TU Clausthal

Clausthal University of Technology

The effect of transport pores on diffusion limitations of Fischer-Tropsch catalyst layers

Doctoral Thesis

(Cumulative Dissertation)

to be awarded the degree

Doctor of Engineering (Dr.-Ing.)

submitted by

Dipl.-Ing. Henning Becker

from Minden

approved by the

Faculty of Mathematics / Computer Science and

Mechanical Engineering,

Clausthal University of Technology,

Date of oral Examination

21.02.2020

D 104

Dean:
Prof. Dr.-Ing. Volker Wesling

Chairperson of the Board of Examiners
Prof. Dr. rer. nat. Alfred Weber

Chief Reviewer:
Prof. Dr.-Ing. Thomas Turek

Reviewer:
Prof. Dr.-Ing. Robert Güttel
Prof. Dr.-Ing. Gunther Brenner

Abstract

One challenge for the utilisation of renewable energy is its highly fluctuating production capacity, as tide, wind and sunlight undergo great daily or even hourly changes. Aside from direct electrical storage conversion of renewable energy into liquid fuels is almost inevitable for long-term storage and for specific mobility applications, e.g. aviation. Hydrogen from water electrolysis can be used in the conversion of carbon-feedstocks into synthetic fuels. In addition to energy storage, this allows an alternative synthetic production of a substitute for crude oil for the chemical industry.

The Fischer-Tropsch synthesis is a process that can produce long-chained hydrocarbons by hydrogenation of carbon monoxide. The reaction occurs on porous catalyst structures that offer a high area of the active metal cobalt. Simultaneously, the catalysts are required to provide a high pore volume to sustain a sufficient diffusive transport of the reactants to the active sites inside the catalyst. The two demands for a high catalytic surface area and an effective diffusive mass transport necessitate a trade-off for the ideal pore size. Small pores typically favour a high activity but hamper diffusive transport and large pores improve mass transport but suffer from lower activity. To reduce the diffusion length, reactors with small catalyst pellets sizes can be used, but then either the pressure drop along the reactor is substantially increased or the catalyst hold-up is very low. Both outcomes may render the entire process ineffective.

By combining larger transport pores, that provide a fast, diffusive access route into the catalyst pellet for the reactants, and small catalyst pores, which maintain a high catalytic activity, it should be possible to improve the total performance of Fischer-Tropsch catalysts. This idea is the central topic of this work and is investigated via simulation and experimental testing. Reactor models for micro-channel reactors with catalytic layers are used for gaining an initial understanding of the relevant phenomena and effects and are further tested against experimental results. For the considered layer geometry, it was shown that only the combined adjustment of layer thickness and transport pore fraction can lead to a significant increase in productivity. Furthermore, the transport pores must be significantly larger than the catalyst pores but at the same time smaller than 30 µm to 50 µm. These requirements were implemented in the experimental investigation using a new, simple manufacturing method. However, little improvement was found, suggesting an insufficient difference in pore geometry that determines effective diffusion. The following simulations also indicated no limitation due to a liquid film forming on the catalyst surface. The complex interplay of diffusive and convective mass transport

on the selectivity and productivity of different layers could also be demonstrated. Especially with high conversions, the potential for improvement is smaller than predicted by a differential model. The comparison of simulation and experiment shows an excellent description of the system by the model. The similar tortuosities for the catalyst and the transport pores obtained from the parameter estimation show that the transport pore geometry requires improvement when a further increase of the catalyst productivity is the objective.

Final evaluation of the model predictions proves the soundness of the modelling assumptions but also raises further questions concerning the actual kinetics, catalyst deactivation and an accurate description of the distribution of the products within the catalyst. These questions may be the subject of further research.

Kurzfassung

Eine Herausforderung bei der Nutzung erneuerbarer Energien ist die stark schwankende Produktionskapazität, da Gezeiten, Wind und Sonnenlicht starken täglichen oder sogar stündlichen Schwankungen unterliegen. Neben dem direkten elektrischen Speichern ist die Umwandlung erneuerbarer Energien in flüssige Kraftstoffe nahezu unausweichlich, insbesondere zur langfristigen Speicherung und für bestimmte Mobilitätsanwendungen wie z. B. für die Luftfahrt. Zur Umwandlung von Kohlenstoffquellen in synthetische Kraftstoffe kann Wasserstoff aus der Wasserelektrolyse verwendet werden. Darüber hinaus wird damit eine alternative Produktion eines Ersatzrohstoffes für die chemische Industrie ermöglicht.

Die Fischer-Tropsch-Synthese ist ein Verfahren mit dem langkettige Kohlenwasserstoffe durch Hydrierung von Kohlenmonoxid hergestellt werden können. Die Reaktion findet an porösen Katalysatoren statt, die eine große Oberfläche des aktiven Metalls, Cobalt, aufweisen. Gleichzeitig müssen die Katalysatoren ein hohes Porenvolumen bereitstellen, um einen ausreichenden Diffusionstransport der Edukte zu den aktiven Stellen innerhalb des Katalysators zu gewährleisten. Diese beiden Forderungen nach einer hohen katalytischen Oberfläche und einem effektiven diffusiven Stofftransport erfordern einen Kompromiss für eine ideale Porengröße. Kleine Poren begünstigen typischerweise eine hohe Aktivität, behindern jedoch den diffusiven Stofftransport, und große Poren verbessern den Massentransport weisen aber oft nur eine geringe Aktivität auf. Um die Diffusionslänge zu verringern, könnten kleinere Katalysatorpellets in den Reaktoren verwendet werden, aber dadurch wird entweder der Druckabfall wesentlich erhöht oder nur sehr wenig Katalysator kann sich im Reaktor befinden. Beides kann die Wirtschaftlichkeit des gesamten Prozesses gefährden.

Durch die Kombination großer Transportporen, die den Edukten einen schnellen diffusiven Zugang zum Katalysatorpellet ermöglichen, und kleinerer Katalysatorporen, die eine hohe katalytische Aktivität aufrechterhalten, ist es möglich die Produktivität von Fischer-Tropsch-Katalysatoren zu verbessern. Diese Idee ist das zentrale Thema dieser Arbeit und wurde anhand von Simulationen und Experimenten untersucht. Reaktormodelle für Mikroreaktoren mit katalytischen Schichten wurden genutzt, um ein Verständnis der relevanten Phänomene und Effekte zu erlangen. Für die betrachte Schichtgeometrie, zeigte sich, dass nur die kombinierte Einstellung von Schichtdicke und Transportporenanteil zu einer deutlichen Steigerung der Produktivität führen kann. Weiterhin müssen die Transportporen deutlich größer als die Katalysatorporen aber

gleichzeitig kleiner als 30 µm bis 50 µm sein. Diese Anforderungen wurden bei der experimentellen Untersuchung durch eine neue einfache Herstellungsmethode umgesetzt. Jedoch wurde nur eine geringe Verbesserung gefunden, was einen unzureichenden Unterschied in der Porengeometrie, die die effektive Diffusion bestimmt, vermuten ließ. Durch nachfolgende Simulationen wurde eine Begrenzung durch einen sich auf der Katalysatoroberfläche bildenden Flüssigkeitsfilm ausgeschlossen. Auch das komplexe Zusammenspiel von diffusivem und konvektivem Stofftransport auf die Selektivität und die Produktivität unterschiedlicher Schichten konnte aufgezeigt werden. Insbesondere bei hohen Umsatzgraden ist das Verbesserungspotential kleiner als von einem differentiellen Modell vorhergesagt. Der Vergleich von Simulation und Experiment zeigt eine hervorragende Beschreibbarkeit des Systems durch das Modell. Die aus der Modell-Anpassung erhaltenen ähnlichen Tortuositäten für den Katalysator und die Transportporen deuten auf eine nötige Verbesserung der Transportporengeometrie hin, wenn deutlichere Steigerungen der Katalysatorproduktivität erreicht werden sollen.
Die abschließende Prüfung der Modellvorhersagen belegt die Belastbarkeit der Modellannahmen, wirft jedoch auch weitere Fragen hinsichtlich der tatsächlichen Kinetik, der Katalysatordeaktivierung und einer genaueren Beschreibung der Verteilung der Produkte innerhalb des Katalysators auf. Diese Fragen könnten als Startpunkt für weitere Forschungsarbeiten dienen.

Acknowledgements

To all that supported me in creating this work, I wish to express my sincere appreciation. First of all, my deepest gratitude goes to my supervisor Prof. Dr.-Ing. Thomas Turek, who provided the opportunity for me to work on this challenging task in the field of reaction engineering and also guided me with seemingly endless patience to the successful conclusion of this work.

I would like to thank Prof. Dr.-Ing. Robert Güttel for being the cause of my involvement in investigating the Fischer-Tropsch synthesis, his efforts to get me to write scientific publications from an early stage on and all the support throughout, many short and long conversations.

Additionally, my special thanks go to Prof. Dr.-Ing. Gunther Brenner for taking over the review of this thesis on a short-notice and his participation in the DFG funded project.

Of course, I also like to thank all my former colleagues at the ICVT for allowing me to work in such a friendly atmosphere, with lots of exciting moments and even a few of them related to work. Specifically, I wish to express my gratitude to

- Carsten Knobloch for handing over and introducing me to such a meticulously build testing rig,
- Nadia Kuwertz, Rafael Kuwertz and Andreas Köppen for sharing their expertise in creating mechanically stable and catalytically active layers,
- Jelka Diedenhoven for being an excellent colleague to share an office with,
- Jens Friedland for being an unequalled well for exciting new ideas,
- Heiner Grimm for providing quick-fixes and simple solutions when time was essential,
- Jens Riede for supporting me with characterisations conducted in Goslar,
- and Vanessa Walter and Sebastian Hofmann for motivating me to also care for my physical health.

I am particularly grateful to Stephan Brandt, without whom no experimental evaluation would have been possible as he manually created all layers investigated.

Furthermore, I would like to thank Heinz Robota, who granted me insights into the research and development of industrial Fischer-Tropsch catalysts. And if nothing else, I owe thanks to my former colleagues at Velocys for helping me enjoy my time in Britain and ever so slightly honing my language-skills, which certainly helped in writing this work.

Finally, I want to thank my parents for their unconditional support allowing me to pursue in life whatever I found interesting and worthy of exploration.
I also want to thank my twin brother for this certainly rare opportunity to talk and exchange ideas about various topics of engineering with an absolute minimum of words, yet complete understanding.
In the end, I want to thank Marina Bockelmann for her perseverance in persuading me to visit Moscow, where I met my fiancée. Without her and the inspiration and motivation she gave me, I probably would still be writing.
My most sincere apologies go to all that I have forgotten to mention here explicitly and conclude with, thank you.

Contents

1 Introduction 1

1.1 The Fischer-Tropsch reaction 1

1.2 Diffusion in the porous catalyst 5

2 Publication overview 9

3 Enhancing internal mass transport in Fischer-Tropsch catalyst layers utilizing transport pores 13

3.1 Abstract 13

3.2 Introduction 13

3.2.1 Model description 16

3.2.2 Transport equations 17

3.2.3 Kinetics and selectivity 19

3.2.4 Objective of the simulation 21

3.2.5 Physical properties 23

3.3 Simulation Results 24

3.3.1 Intrinsic reaction rates 24

3.3.2 Reaction-diffusion effects – limitation of layer thickness 24

3.3.3 Mass transfer improvement by transport porosity optimization 29

3.3.4 Effect of tortuosity 31

3.3.5 Maximum allowable transport pore diameter 34

3.3.6 Temperature gradients 35

3.4 Conclusions 35

3.5 Acknowledgements 37

3.6 Notation 37

3.7 References 39

4 Experimental evaluation of catalyst layers with bimodal pore structure for Fischer–Tropsch synthesis 43

4.1 Abstract 43

4.2 Keywords 43

4.3 Introduction 44

4.4 Experimental 46

4.4.1 Catalyst preparation ... 46
4.4.2 Fischer-Tropsch experiments ... 47
4.4.3 Temperature-programmed reduction ... 48
4.4.4 Nitrogen physisorption ... 48
4.4.5 Mercury intrusion ... 48
4.4.6 Roughness and texture ... 49
4.4.7 Density and porosities ... 49
4.4.8 Chemisorption and oxygen titration ... 49
4.5 Results and discussion ... 50
4.5.1 Preparation results and ex-situ characterization ... 50
4.5.2 Experimental Fischer-Tropsch performance ... 55
4.6 Conclusions ... 59
4.7 Acknowledgements ... 60
4.8 Notation ... 60
4.9 References ... 61
5 Performance of diffusion-optimised Fischer-Tropsch catalyst layers in microchannel reactors at integral operation ... 67
5.1 Abstract ... 67
5.2 Introduction ... 68
5.3 Model description ... 69
5.3.1 Transport in gas phase ... 71
5.3.2 Transport in liquid phase ... 71
5.3.3 Diffusion and reaction in catalyst ... 72
5.3.4 Kinetics ... 73
5.4 Simulation results ... 77
5.4.1 Typical behaviour and expectations ... 77
5.4.2 Effects of integral operation ... 81
5.4.3 Film formation – effects of external mass transfer ... 90
5.5 Conclusions ... 94
5.6 Conflicts of interest ... 97
5.7 Acknowledgements ... 97
5.8 Notation ... 97
5.9 References ... 98

6 Model validation 103

6.1 Parameter estimation 103

6.1.1 Deactivating catalyst 103

6.1.2 Enhanced selectivity model 109

6.1.3 Estimation results 111

6.2 Introducing vapour and liquid phase 120

6.2.1 Model set-up and equations 122

6.2.2 VLE model compared to reactor model 124

6.2.3 Spatial distribution of hydrocarbons 125

6.3 Model sensitivity analysis 132

6.3.1 Transport pore effect 132

6.3.2 Effect of temperature 135

6.4 Notation 138

7 Conclusion & Outlook 143

References 147

Appendix 153

A. Supporting information to chapter 3 153

Catalyst volume 154

Layer volume 154

Channel volume 155

Layer surface area 155

B. Supporting information to chapter 5 156

Film formation 156

Modified ASF selectivity model 157

Reactor performance parameters 159

Convective transport in liquid versus gas phase 161

Effects of conversion on selectivity 163

Additional values for the effect of conversion 164

References 164

C. Supporting information for the model validation 166

1 Introduction

Despite an already decades-old [1] and growing public will to reduce the emissions of greenhouse gases into the atmosphere, the effects of climate change are becoming more and more perceivable [2]. Among the greenhouse gases, CO_2 is the gas that is released into the atmosphere in largest quantities as the main product of burning fossil fuels. Out of the fossil fuels, crude oil, and all fuels derived from it, are used to power combustion engines for electric power generation, domestic heating and transportation. Reducing the emissions from that use would greatly benefit the objective to limit global warming. Besides lowering the fuel consumption and switching over to renewable electric energy and its storage, the fuels can also be generated from carbon feedstocks that are either renewable themselves or comprise of otherwise unused waste materials. One important step in the process of converting these carbon feedstocks into usable liquid fuel is offered by the Fischer-Tropsch synthesis [3,4].
Aside from the conversion of renewable feedstocks, the Fischer-Tropsch process was and is used to generate high-value liquid fuels from coal and natural gas [5]. But, here facilities with huge production capacities next to large reservoirs of natural gas or coal are required to operate economically. The large scale of these sites allows benefiting from relatively reduced cost impact of the reactor and catalyst. But for renewable carbon sources, the production capacity is significantly reduced as only smaller and more distributed sources come into consideration. To make the Fischer-Tropsch process for these constrictions economically possible, a highly productive reactor with a very active and stable catalyst is required [6]. Out of the required high catalyst activity arises a substantial effect of transport limitations within the catalyst. To keep these limiting effects to a minimum transport pores can be advantageously used to avoid the alternative of reducing the catalyst pellet size, as small particles will increase pressure drop or may reduce the total catalyst hold-up. Assessment of transport pores for Fischer-Tropsch catalysts by means of simulation and experimental characterisation is the objective of this work, to find out about the chances and limitations of this approach to improve the catalysts performance.

1.1 The Fischer-Tropsch reaction

The Fischer-Tropsch synthesis, discovered by Hans Fischer and Franz Tropsch in the early 20^{th} century, converts H_2 and CO at elevated pressures into long-chained

hydrocarbons, mainly paraffins and olefins. The reaction is catalysed by different metals, but mostly cobalt, iron and ruthenium are used. Iron has a lower activity and is typically used in the so-called "high-temperature synthesis" at temperatures around 340 °C producing branched and relatively short hydrocarbons. Cobalt and ruthenium are more active than iron, with ruthenium exhibiting highest activity but at a substantially higher price and comparably low availability. Therefore cobalt is typically used at temperatures between 200 and 240 °C in the "low-temperature synthesis" [7,8]. At these temperatures, cobalt produces much longer products than the hydrocarbons that can be produced with the high-temperature synthesis on iron. The heavier weight products from cobalt are more valuable but also cause the products to remain in the liquid phase, at least to some extent. This presence of the liquid phase causes certain limitations for the catalyst's productivity as diffusion in the liquid products is slow. Further understanding of these limitations and the potential for transport pores require to understand the general set-up of the catalyst and the specifics of diffusion inside the catalyst.

In order to obtain a catalyst of high activity, the surface area of the metal, on which the reaction takes place, needs to be as high as possible. Hence, the active metal needs to be dispersed into small particles to yield a high ratio of surface area to metal volume, and catalyst mass. Though, as particles with a diameter of less than about 4 nm tend to form overly more undesired methane, due to a higher hydrogen coverage, for cobalt there exists an ideal particle size of approximately 4 nm to 5 nm [9]. To obtain particles of that small size the metal needs to interact with a support material that stabilises the particles and allows for their formation in the first place. As support material porous alumina, silica and titania can be used. For the preparation, a metal precursor, often cobalt nitrate, is inserted into the pores of the support by impregnation and then decomposed during calcination, thermal treatment, of the catalyst [10,11]. After this calcination, oxidic cobalt is obtained, that require further reduction before the Fischer-Tropsch reaction can begin. But the size of the cobalt oxides is proportional to the size of the cobalt metal particles. Therefore, during calcination, when the cobalt oxides are formed, the eventually obtainable cobalt particle size is already defined. A strong correlation between the support pore diameter and the size of the cobalt particles exists and demands the use of small-diameter pores to obtain highly active catalysts. The correlation is because of the confining effect of the pores that constrict the growth of cobalt particles to a size similar to the diameter of the pores. But, at the same time catalysts with smaller pores perform worse in terms of selectivity, which is assumed to be caused by a constriction of the diffusive flow of reactants when the pores get too small [12,13]. However, on the basis of the same data, there is also a positive correlation between pore volume and C_{5+}

selectivity, indicating that diffusion is governed by pore size as well as the volume fraction of the pores. Nonetheless, a preparation method that allows obtaining a better-dispersed catalyst for a given support material is desirable, and methods have been developed to improve the calcination process. Modification of the calcination atmosphere by addition of NO, that reacts with the cobalt nitrate already at low temperatures, stabilises the cobalt phase and allows for high cobalt dispersions [14,15]. Other methods involve using organic agents to improve the decomposition reaction, effectively increasing the decomposition speed to heat up the catalyst rapidly and thereby reducing the time for the mobile precursor to migrate and agglomerate [16,17].

All these methods lead eventually to a catalyst where cobalt nanoparticles, with ideally the size of about 5 nm, yet regularly larger, are located inside of a porous catalyst pellet with a size of up to several hundred micrometres or even a couple of millimetres [18–21]. Figure 1.1 shows an illustrative drawing of a catalyst pellet with the cobalt particles distributed inside the pores to which the reactants must be transported before the adsorption and subsequent reaction can form the long-chained hydrocarbon products. During the synthesis the formed products fill the pores with liquid and the only relevant transport mechanism for the consumed reactants is diffusion, which is driven by a concentration gradient within the pellet that again results from the consumption reaction of the reactants on the cobalt. Although the actual kinetics for the Fischer-Tropsch reaction on cobalt are not conclusively revealed, there are several suggested pathways and general steps involved in the reaction. First, during adsorption H_2 dissociates to atomically bound hydrogen, whereas CO associatively bonds to the surface. In the following activation step, CO is hydrogenated to some variation of an adsorbed CH_x

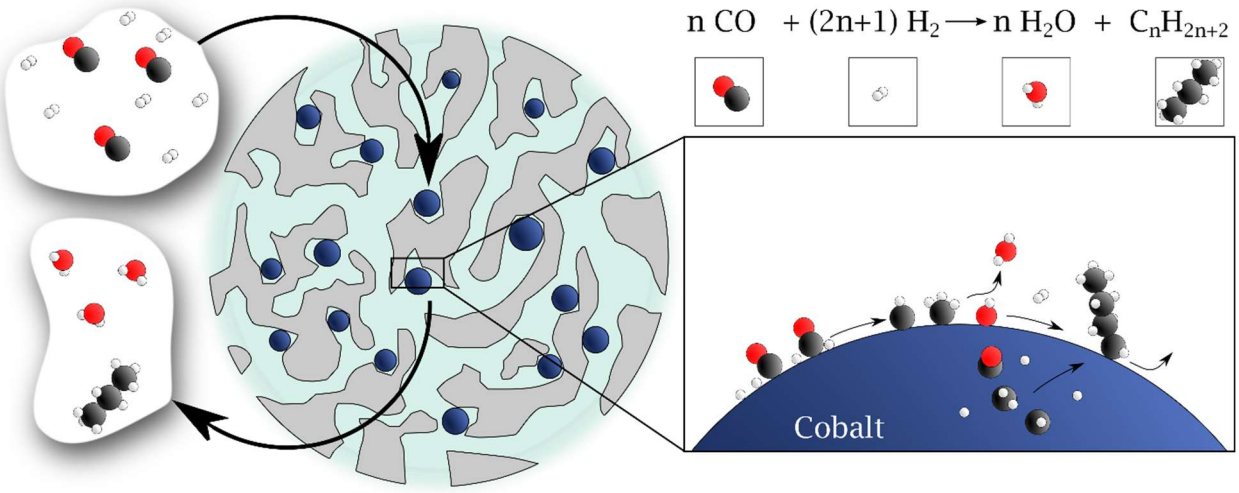

Figure 1.2: Schematic illustration of the porous catalyst pellet with reactants and products diffusing in and out (left) and the reaction on the cobalt surface (right).

species. This reaction forms a carbon pool that is the basis for the polymerisation reaction where long chains are formed. Finally, the formed chains desorb from the surface [8]. The rate-determining step for the entire reaction is assumed to be activation of the CO, and this is likely to be assisted by hydrogen [22,23]. But also hydroxyls can play an important role in splitting the C-O bond – independent of whether CO is molecular adsorbed or already a part of a longer hydrocarbon chain [24]. When CO is directly participating in the chain growth step, the total rate and product selectivity are intricately interrelated. However, there is a debate whether the chain propagation is a result of CO insertion [25–28] into the chain or due to addition of a monomer from the CH_x pool [29,30] or even a result of a simultaneous competitive occurrence of both mechanisms [31,32].

Irrespective, of the actual microkinetic mechanisms for every propagation step the chain can either grow or be terminated by hydrogenation or desorbed. From this, a ratio of propagation rate over the sum of propagation and termination rate for every chain length defines the probability of chain propagation, α. Typical values for cobalt catalysts are between 0.8 and 0.9, but even higher values are desired, as the closer this number gets to unity the higher the fraction of high-value long-chained hydrocarbons in the products. Though the chain growth probability is often assumed to be constant over the entire carbon number range, which allows for a reasonable description of the product distribution [33,34], experimental results and DFT calculations suggest a chain growth probability that is variable for every chain length [30]. More complicated models, therefore, attempt to superpose two distributions [35,36], each with a single α, but also process conditions have an effect on the chain growth probability [37]. A variation of process conditions generally indicates a negative correlation with temperature and also a strong effect of the concentration of the reactants. With high concentrations in H_2, the termination of the chain is favoured leading to low values for α, whereas high concentrations of CO lead to an improved propagation rate, causing high values for α. With the diffusion of the reactants, this causes some challenges when either large pellets or narrow pores are used. Both are beneficial to produce a catalyst that exhibits a low pressure-drop and a high catalyst activity, respectively. But at the same time, diffusion is more and more restricted when small pores and large particles are used. Here, the addition of transport pores can accelerate the flux by which reactants are transported into the catalyst while still a substantial number of narrow pores can be used to stabilise the cobalt to yield a high activity.

1.2 Diffusion in the porous catalyst

Diffusion is the main transport mechanism of the reactants inside the catalyst, where the pores are filled with liquid products. Diffusion in liquids is slow, compared to diffusion in the gas phase, and the diffusion coefficient is affected by the size of the moving solute, as well as the size of the solvent. For the diffusion of H_2 and CO in liquid Fischer-Tropsch products, this means that the diffusion of the smaller H_2 is about three times faster than the diffusion of CO and both are similarly affected by a change of the solvents average chain length [38,39]. In figure 1.2, predicted diffusion coefficients for H_2 and CO in hydrocarbons with varying carbon numbers are shown for three different temperatures. The predictions are based on correlation equations on experimental data and indicate that at low carbon numbers diffusion is much faster than at high carbon numbers [40,41]. The effect of varying solvent composition, as illustrated by the gradient of the plot, is also much greater at low carbon numbers than at high values. In comparison, the temperature has a much more modest yet fairly constant influence over the entire carbon number range. Hence, when diffusion limitations lead to an increase in the concentration ratio of H_2 and CO, as H_2 diffuses faster than CO, this alters the selectivity towards shorter chained hydrocarbons, and the resulting product distribution

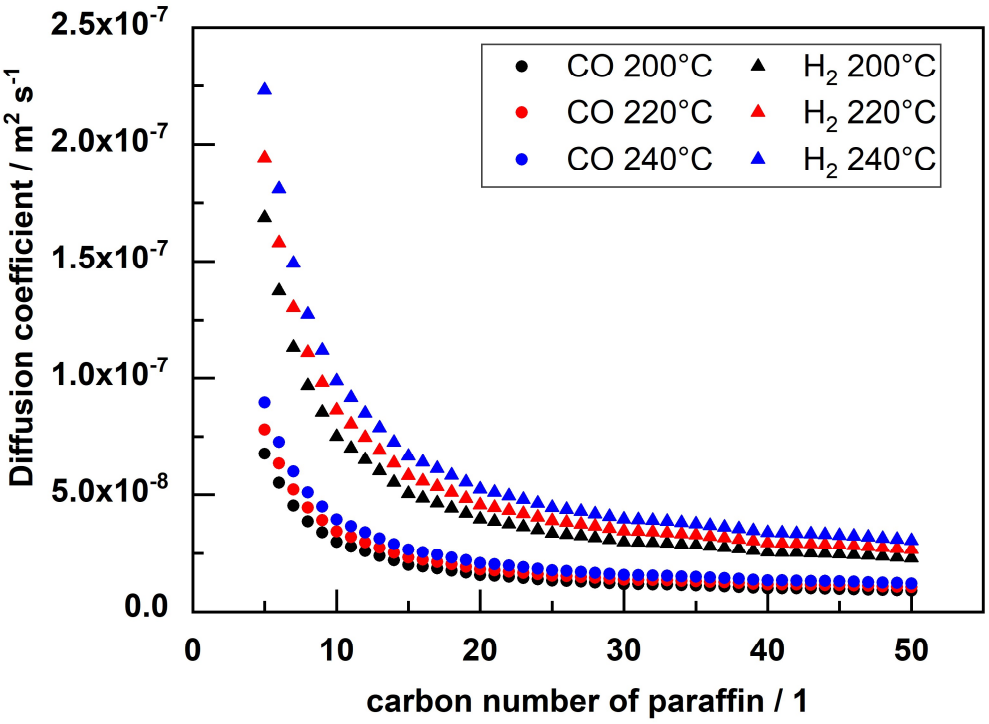

Figure 1.2: Calculated diffusion coefficients for the reactants as function of the carbon number of pure paraffins at different temperatures.

will have a lower average carbon number. In return the lower carbon number improves the diffusion limitations, causing the initial change in the concentration of the reactants to be less severe. This would eventually lead to a certain average carbon number in the liquid products, but simulation would require significant computational efforts. Therefore, a constant average carbon number is assumed in this work. Only in the last chapter, some validation for the chosen carbon number is provided.

Aside from the direct effects on the molecular diffusion, there is also an impact of the pore system on the effective diffusion coefficient, $D_{e,i}$, that is a simplified descriptor of the actual diffusion in a porous system. The upper limit is given by the molecular diffusion coefficient of each species, D_i, and since diffusion can only occur in the void of the pores, the volume fraction of the pores, the porosity ε, also needs to be factored in. Finally, the last part in equation 1.1 for the definition of the effective diffusion coefficient is the tortuosity, τ. It can be defined as an elongation factor of capillaries that would

$$D_{e,i} = \frac{\varepsilon}{\tau} D_i \tag{1.1}$$

yield an effective diffusion coefficient equivalent to an observed one for a real system. Therefore, if a slab-like porous structure consists of straight cylindrical pores, perpendicular to the surface, the resulting tortuosity would equal one. Yet, when the pores are not arranged perpendicular but are slanted at an angle of 60° to the vertical, a tortuosity of two is obtained. This is illustrated schematically in figure 1.3 in the first two cases. A more realistic structure is given by agglomeration of spheres. For monodisperse spheres in a cubic lattice already in the 19th century, Lord Rayleigh [42] described a correlation that later was expanded and found to be independent of the size distribution of the non-overlapping spheres in a homogeneous, isotropic agglomerate [43]. For these cases, the tortuosity remains in boundaries between 1.5 and unity (figure 1.3 c). However, slightly higher values are obtained when the spheres are allowed to overlap randomly [44]. Actual tortuosities for real pore networks can be substantially higher, especially for catalysts where the original pore system of the support may be blocked by the deposition of the active metal within these pores (figure 1.3 d). Additionally to this tortuosity, that was purely based on the geometry, for very narrow pores the effective diffusion of reactants can also be further reduced due to a steric exclusion of the reactants because of their size [45–48]. For pores of 5 nm, which is a useful size to produce catalysts with highest activities, using literature data for solute diameter and effective diffusion model [40,48] and for the larger CO molecule, the maximum tortuosity that can be expected is about 46% higher than just the geometric value. For H_2, the relative increase

is with ca. 34% a little lower, but this additional difference would further increase the gap between the diffusivities for the two reactants.

The idea behind the use of transport pores is that a certain volume fraction of the porous structure ideally comprises of straight pores that are sufficiently large to avoid steric hindrances to diffusion but are small enough not to add additional transport limitations. These transport pores would then exhibit a tortuosity of one, while the remaining pores in the catalyst would create a highly active catalyst with a higher tolerance for high tortuosities. It can be seen as a merging of the straight pores with the realistic catalyst pores of figure 1.3 (a, d). The details of this for the Fischer-Tropsch reaction are investigated in more detail in the following chapters.

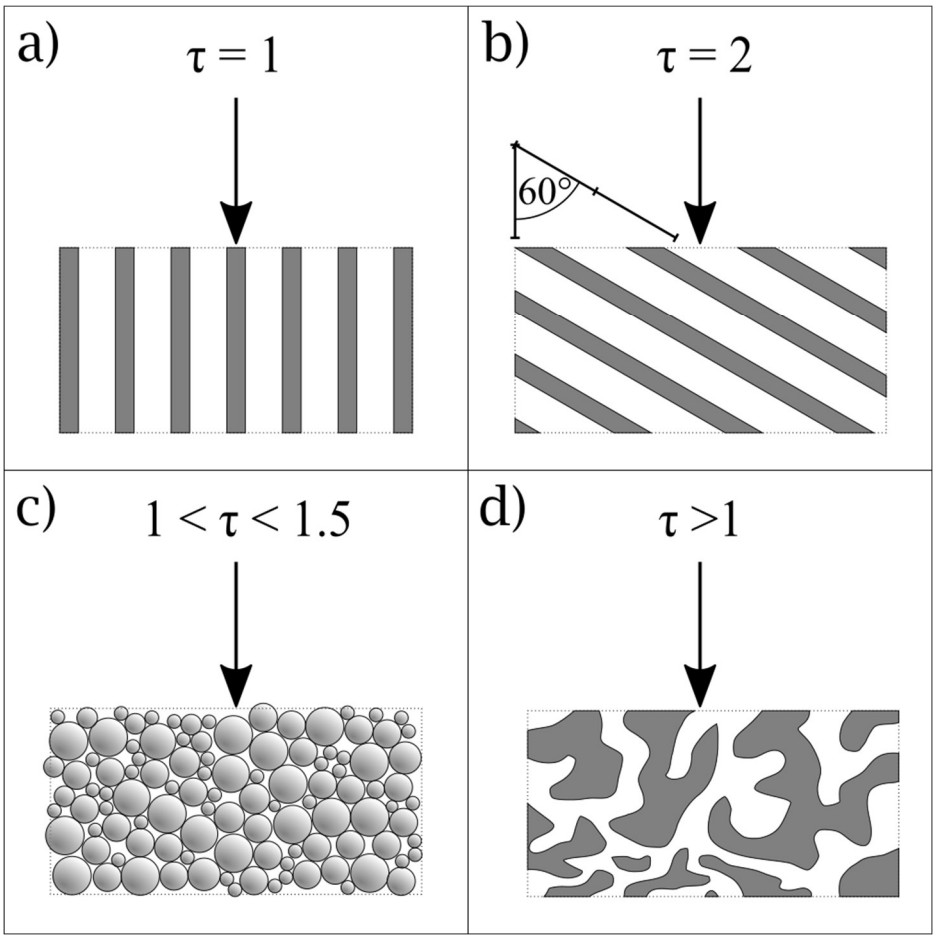

Figure 1.3: Schematic drawing of different pore geometries with according tortuosity values, a) straight, b) slanted, c) agglomeration of spheres and d) irregular.

2 Publication overview

The following publications were submitted and published in "peer-reviewed" scientific journals and are an integral part of this doctoral thesis.

1. H. Becker, R. Güttel, T. Turek, *Enhancing internal mass transport in Fischer–Tropsch catalyst layers utilizing transport pores*, Catal Sci Technol, **2016**, 6(1), 275-287

   The current impact factor of the journal Catalysis Science & Technology is **5.726**. The first author developed a reaction engineering model, carried out the simulation and prepared the manuscript. T. Turek and R. Güttel provided advise for the model development and contributed to the writing of the manuscript. This publication is reprinted in chapter 3 and defines an objective for comparing catalyst layers with and without transport pores and describes the method of finding an ideal transport porosity and layer thickness by use of a differential reactor model. It further details the requirements on transport pores and catalyst pores in terms of tortuosity and pore size to improve mass transport and catalyst performance.

2. H. Becker, R. Güttel, T. Turek, *Experimental evaluation of catalyst layers with bimodal pore structure for Fischer–Tropsch synthesis*, Catal Today, **2016**, 275, 155-163

   The current impact factor of the journal Catalysis Today is **4.888**. It was the contribution of the first author to design and conduct the experiments and to prepare the manuscript. R. Güttel assisted in the evaluation of the experiments and contributed to the writing of the manuscript. T. Turek assisted in the conception of the experiments and contributed to the writing of the manuscript. This publication is reprinted in chapter 4 and describes a method of preparing and characterising catalyst layers with and without transport pores and variable layer thickness. It further evaluates the experimentally feasible benefit of transport pores for Fischer-Tropsch catalysts.

3. H. Becker, R. Güttel, T. Turek, *Performance of diffusion-optimised Fischer–Tropsch catalyst layers in microchannel reactors at integral operation,* Catal Sci Technol, **2019**, 9(9), 2180-2195

   The current impact factor of the journal Catalysis Science & Technology is **5.726**. The first author developed a reaction engineering model, carried out the simulation and run the experiments. T. Turek provided advise for the model

development and contributed to the writing of the manuscript. R. Güttel contributed in writing of the manuscript. This publication is reprinted in chapter 5 and describes an integral reactor model with improved kinetics for the product selectivity as an evolution of the differential reactor model of chapter 3. The intricate interplay between diffusion and convection and its implications on the reactor performance of layers with and without transport pores and various layer thicknesses are evaluated in detail.

3 Enhancing internal mass transport in Fischer-Tropsch catalyst layers utilizing transport pores

With permission from the Royal Society of Chemistry, reproduced from:
H. Becker, R. Güttel, T. Turek
Catal. Sci. Technol, **2016**, 6 (1), 275–287
DOI: 10.1039/C5CY00957J

3.1 Abstract

Internal mass transport limitations inside Fischer-Tropsch catalysts due to the slow diffusion of reactants in the liquid-filled pores may significantly alter selectivity and the achievable productivity. In this work, diffusive restrictions for planar catalyst layers were investigated by mathematical modelling and simulation. A one-dimensional model utilizing empirical kinetics, incorporating transport pores as an additional pathway for the mass transport and taking into account heat production, allows for the calculation of catalyst efficiency and productivity towards C_{5+} products. As diffusional mass transport leads to strong concentration gradients that impair selectivity, an optimum layer thickness with maximum C_{5+} productivity can be found. Additional transport pores enhance the mass transport but reduce the amount of active phase, which requires a trade-off by optimizing the fraction of transport pores and layer thickness. For reference conditions, the catalyst layer with an ideal amount of transport pores and ideal thickness exhibits a productivity that is about 47% higher than for the best layer without transport pores. This improvement requires transport pores with diameters not larger than about 60 µm. While the improvement potential significantly depends on the effective diffusivities, the effect of heat generation was found to be negligible.

3.2 Introduction

Conversion of synthesis gas in low-temperature Fischer-Tropsch (FT) reaction yields a broad spectrum of hydrocarbons that can be used for various further applications such as the production of diesel fuels. An efficient process requires a high selectivity towards long-chained hydrocarbons over the commonly used cobalt-based catalysts [1]. Thus, products with high carbon numbers remain in a liquid phase under reaction conditions.

Consequently, reactors for the low-temperature FT process must be suitable for the resulting three-phase system [2] with fixed-bed reactors and slurry bubble columns being commercially established [3,4]. Considering diffusion limitations, pressure drop and thermal behaviour, the dimensions of catalyst pellets and tubes have to be optimized for conventional fixed-bed reactors [5,6] A further option is the use of micro-packed bed reactors, which are beneficial due to increased heat removal at moderate pressure drop [7]. In reactors of this type highly active catalysts exhibit excellent performance [8], but depending on the catalyst particle size, one can either improve pressure drop [9,10] or mass transport. Micro-structured reactors with a wall coating of catalyst offer an extraordinarily low pressure-drop and high catalyst efficiency but suffer from low catalyst inventory and therefore low reactor productivity [11]. The low catalyst inventory results from diffusion limitations that restrict the thickness of the catalyst coating [12, 13]. Diffusivity inside the FT catalyst is slow due to the liquid products that remain inside the pores of the catalyst during reaction [14]. Moreover, these severe internal mass transport effects do not only retard the reaction but also hamper selectivity [15–19].

Different approaches have been made to deal with the restrictions in catalyst size caused by limited diffusion length. To achieve a low diffusion length, the use of eggshell catalysts or structured packings and open foams as catalyst support was proposed [20–23]. This reduces the negative impact of internal diffusion limitations, results in a low pressure drop and, especially for foams and packings, also a good heat removal. Nonetheless, these approaches suffer from low catalyst inventory and do not directly enhance internal mass transport. For improvement of the diffusive transport inside the catalyst, a bimodal pore structure can be used. Xu et al. [24] compared experimental results from FT synthesis with a mathematical model indicating that a bimodal catalyst gives rise to high activity at low diffusion resistance [24].

Since diffusion occurs in a porous system, shape and size of the pores are crucial for a productive catalyst. On the one hand, small pores of the catalyst support are necessary in order to obtain catalysts with high activity [25–28], since small pores confine the cobalt species to nanometer-sized particles with high specific surface areas. On the other hand, diffusion becomes very slow in liquid-filled catalyst support pores of small size, as shown by Preising and Enke [29] for porous glasses. This can be attributed to restricted diffusion as a result of a solute with a critical molecular diameter in the range of the pore diameter [30–34]. This pore size effect is similar to the well-known Knudsen diffusion regime during gas-phase mass transport. Although a comprehensive, exact matching correlation for the description of these effects could not yet be developed, the work of the above-mentioned authors emphasizes that nanometer-sized pores

additionally hinder diffusion in the liquid phase. Therefore, optimized catalyst designs require larger pores to improve the accessibility of the catalyst for the reactants in addition to smaller pores providing high surface area and activity.

Literature reports different approaches to describe the effect of pore structures on effective diffusion. From general analytical solutions of simplified models for bidisperse systems [35,36] or fractal pore models [37,38] to numerical approaches regarding three-dimensional pore networks [39, 40] catalyst efficiency depends on effective diffusivity and thus on structural parameters like tortuosity or pore connectivity [41]. Although these parameters can be measured [42, 43] the validity, especially for tortuosity under reaction conditions, is not necessarily given. A three-dimensional multiscale simulation approach tries to avoid these uncertainties by starting with a nanometer-scale model to evaluate effective diffusivities for a mesoporous structure, which can then be used for further simulation of effective diffusivities and reaction rates on the micrometer scale. In the last step, these results are then applied to evaluate a reactor model. For CO oxidation, this approach by Pereira et al. [44] leads to good agreement between experimental results and simulation. But even here, the validity of effective diffusivities depends on the reliability of the nanoscopic structure. An optimization by Gheorghiu and Coppens [45] of two-dimensional bimodal pore networks for a simple gas-phase reaction of first order illustrates the trade-off between ease of access and productivity which depends on of pore fraction and pore size. It is shown that transport pores are especially interesting if diffusion in micro- and mesopores is slow due to Knudsen diffusion. Further systematic evaluation from Wang et al. [46] and Johannessen et al. [47] has revealed, that a uniform transport pore size and fraction can yield almost the same improvement as an optimized distribution of transport pores. These results obtained for simple first-order kinetics were applied to calculate the optimal porous structure of a catalyst layer for methane reforming [48], indicating a considerable increase in activity for a commercial catalyst.

In the present work, a simplified mathematical model is used to describe the effects of reactant diffusion in catalyst layers with small and large pores on activity and selectivity of the FT reaction. Using the approach of Vervloet et al. [18] for description of the chain growth probability as a function of reactant concentration and temperature, we have already shown that it is possible to find an ideal layer thickness, where the yield with respect to the desired products reaches a maximum [49]. In the present paper, the optimization potential by adjusting the transport pore fraction is analyzed in detail with respect to the effective diffusivities in the catalyst and the transport pore phase. Furthermore, the relevance of temperature gradients and the maximum allowable transport pore diameter are evaluated. In other words, by applying realistic,

experimentally based kinetics and transport parameters to optimization of pore structure, we demonstrate how and up to which extent transport pores can enhance the productivity in Fischer-Tropsch synthesis.

3.2.1 Model description

The general idea is that transport pores inside a catalyst provide a bypass for diffusive transport of reactants inside the catalyst and thus improve the effective mass transport. However, since the volume fraction of transport pores does not contribute to the reaction, an increased transport pore fraction improves mass transport at the expense of a reduced amount of catalytically active phase. This emphasizes the necessity of a compromise that has to take into account the reduced volume fraction of the active phase and the benefit of an improved mass transport.

The developed model is based on a planar geometry of a catalyst coated on the wall of a microchannel reactor but can also be applied to washcoated monoliths and egg-shell catalysts, as long as the active catalyst layer remains thin. The catalyst layer is assumed to consist of a mesoporous active catalyst and cylindrical macropores denoted as transport pores.

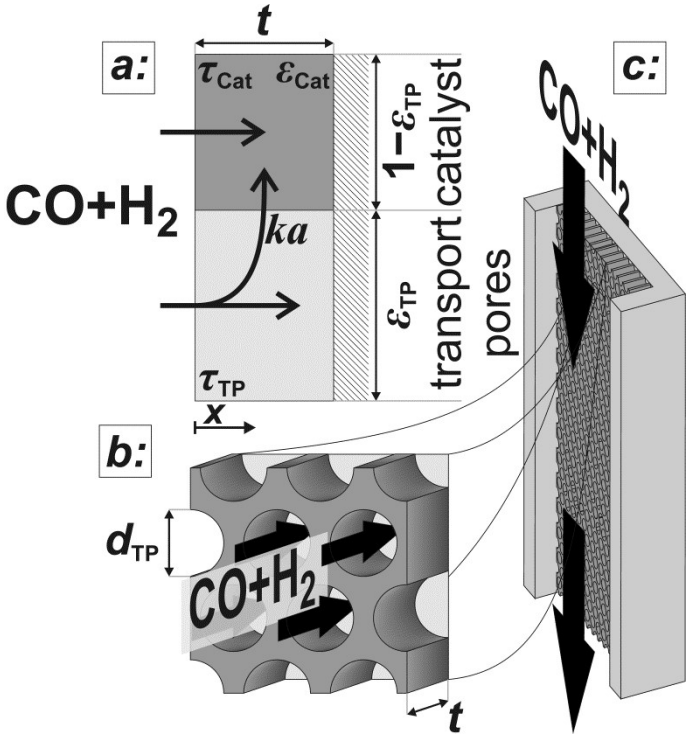

Figure 3.1: Schematic of the catalyst layer with porous catalyst and transport pores as two separate phases: transport pathways inside the reference volume of the model (a), geometry of the cylindrical transport pores (b) and microchannel reactor with catalyst layer (c).

Above the catalyst layer remains the free cross-section area of the channel. In order to investigate the effects of the diffusion in the catalyst and the transport pores only, axial convection and external mass transport are neglected. This leads to the assumption of constant reactant concentrations at the gas-solid boundary and simplifies the model to only one dimension (figure 3.1). Although this reduction to a differential reactor does not lead to results which could directly be compared to experimental data, it allows results with general significance to be derived, which are also applicable to different reactor concepts. For the solution of the model equations, gPROMS® ModelBuilder 4.0.0 of Process Systems Enterprise Ltd. was used. The transport equations were distributed over 50 elements using a second-order "orthogonal collocation on finite elements method" (OCFEM) for discretisation.

3.2.2 Transport equations

The reaction takes place on the active surface inside the catalyst. Therefore, the reactants carbon monoxide and hydrogen have to be transported into the catalyst layer. This diffusive transport occurs as a result of a concentration gradient between the gas-solid boundary and the depth of the catalyst. Since two types of pores concurrently contribute to diffusive mass transport, but reaction occurs on the active surface only, catalyst phase and transport pore phase must be distinguished within the catalyst layer. The volume fraction of the transport pores is defined by $\varepsilon_{\mathrm{TP}}$. This virtual separation of transport phase and active phase is a main idea of the simulation approach (figure 3.1 (a)).

The representative volume element for the mass balance is the whole catalyst layer (figure 3.1 (a)) comprising the active and transport phases. Mass transport is described according to equation (3.1) with a term considering effective diffusion inside the catalyst and the transport pore phase, and a reaction term. As the transport pores are inert, the active catalyst fraction $(1-\varepsilon_{\mathrm{TP}})$ has to be considered for the reaction term. The diffusion term simplifies the original two-dimensional problem to a one-dimensional equation, accounting for the different effective diffusivities inside catalyst and transport pores. This effective one-dimensional model is valid as long as transport pores are sufficiently small, thereby leading to the same concentration profiles in catalyst and transport pores [47].

$$\left((1-\varepsilon_{\mathrm{TP}})\frac{\varepsilon_{\mathrm{cat}}}{\tau_{\mathrm{cat}}}+\frac{\varepsilon_{\mathrm{TP}}}{\tau_{\mathrm{TP}}}\right)D_{\mathrm{i}}\frac{d^2}{dx^2}(c_{\mathrm{i}}(x))+(1-\varepsilon_{\mathrm{TP}})\nu_i\,(x)r_{\mathrm{CO}}(x)=0 \qquad (3.1)$$

The effective diffusion is assumed to obey Fick's law which is modified with porosity and tortuosity. It has to be mentioned that the reference volume for the catalyst porosity is the catalyst phase, while it is the whole catalyst layer for the transport pore fraction. Thus, the sum of transport pore fraction and catalyst porosity is not unity. The assumed reference values for porosity and the tortuosities are listed in table 3.1. As the transport pores are cylindrical and parallel to the direction of the diffusion, the tortuosity of the transport pores equals one. This is an ideal assumption, since transport pores of real catalyst layers will not easily exhibit such a simplified best-case geometry. Reference tortuosity of the catalyst is assigned a value of 3, which is in the typical range [29,50]. The supposed reaction kinetics in equation (3.1) are dependent on the concentration of carbon monoxide and hydrogen; consequently only these species are relevant for mass transport and need to be considered for the boundary conditions (equation (3.2) and (3.3)).

$$c_i|_{x=0} = \frac{p_i}{H_i v_L} \tag{3.2}$$

$$\left.\frac{\partial c_i}{\partial x}\right|_{x=t} = 0 \tag{3.3}$$

Since the FT reaction is quite exothermic, the removal of heat may have a significant impact. Therefore, the heat balance was taken into account. The corresponding differential equation (3.4) neglects the influence of a varying transport pore fraction on the effective thermal conductivity and incorporates the transport pore fraction only via the residual amount of catalyst, $(1-\varepsilon_{TP})$, which scales the heat source term.

$$\lambda_{\text{eff}} \frac{d^2}{dx^2}\big(T(x)\big) + (1-\varepsilon_{TP}) r_{CO}(x)\, \Delta_R H = 0 \tag{3.4}$$

Similar to the mass transport, the boundary conditions assume that all heat is removed through an isothermal wall and the heat flux to the gas boundary is zero (equation (3.5) and (3.6)).

$$T|_{x=t} = T_0 \tag{3.5}$$

$$\left.\frac{\partial T}{\partial x}\right|_{x=0} = 0 \tag{3.6}$$

For the reaction enthalpy, a value of 170 kJ mol_{CO}^{-1} was chosen, which is a quite high estimate compared to literature [5,6,11,51]. For the effective thermal conductivity a

value was chosen, that is significantly lower than conductivities of the solid catalyst phase [48,52], the liquid phase [53], the gas phase in Fischer Tropsch reaction [54] or the estimated effective bed conductivity [55]. Hence, the chosen approach should give rise to a worst-case assessment of possible heat transport effects.

Table 3.1: Structural transport parameters of the active catalyst and transport pore phase.

Parameter	Value	Unit
ε_{cat}	0.4	m^3_{pore}/m^3_{cat}
τ_{cat}	3	-
τ_{TP}	1	-
λ_{eff}	0.1	W/(m K)

3.2.3 Kinetics and selectivity

For the description of the CO consumption rate, an approach from Yates and Satterfield [56] is used (equation (3.7)), where a temperature dependency analogous to the Arrhenius equation as proposed by Maretto and Krishna [57] is utilized (equation (3.8) and (3.9)).

$$r_{CO} = \rho_{cat} \frac{a\, p_{H_2} p_{CO}}{(1 + b\, p_{CO})^2} \tag{3.7}$$

$$a = a_0 \exp\left(\frac{E_{Aa}}{R}\left(\frac{1}{493.15\ K} - \frac{1}{T}\right)\right) \tag{3.8}$$

$$b = b_0 \exp\left(\frac{E_{Ab}}{R}\left(\frac{1}{493.15\ K} - \frac{1}{T}\right)\right) \tag{3.9}$$

Assuming paraffins to be the only hydrocarbon products (equation (3.10)), the chain growth probability allows calculating the stoichiometric coefficients for all species participating in the reaction.

$$\nu_{CO}\ CO + \nu_{H_2} H_2 \rightarrow \nu_{H_2O}\ H_2O + \nu_{Cn}\ C_nH_{2n+2} \tag{3.10}$$

The relationship developed by Vervloet et al. [18] describes the chain growth probability as a function of reactant concentration and temperature (equation (3.11)). Constants for reaction rate and chain growth probability are specified in table 3.2. The stoichiometric

Table 3.2: Constants for equations describing reaction rate and chain growth probability [18, 56, 57].

Parameter	Value	Unit
ρ_{cat}	1000	kg/m³
a_0	8.853×10^{-3}	mol/s bar²
b_0	2.226	1/bar
E_{Aa}	37.37	kJ/mol
E_{Ab}	-68.48	kJ/mol
β	1.76	-
k_α	0.0567	-
ΔE_α	120.4	kJ/mol

coefficients of carbon monoxide and water are independent of the hydrocarbon chain length (equation (3.12) and (3.13)). However, this is not the case for the consumption of hydrogen, for which the stoichiometric coefficient is accessible via equation (3.14) [18]. For a chain growth probability of zero, all carbon monoxide is converted to methane, thus leading to a stoichiometric coefficient for hydrogen of three. Whereas for a chain growth probability close to unity almost exclusively long-chained hydrocarbons are formed, hence resulting in a hydrogen coefficient of virtually two. The stoichiometric coefficients of the hydrocarbons follow the ASF distribution according to equation (3.15).

$$\alpha = \frac{1}{1 + k_\alpha \left(\frac{c_{H_2}}{c_{CO}}\right)^{\beta} \exp\left(\frac{\Delta E_\alpha}{R}\left(\frac{1}{T_{ref}} - \frac{1}{T}\right)\right)} \tag{3.11}$$

$$\nu_{CO} = -1 \tag{3.12}$$

$$\nu_{H_2O} = 1 \tag{3.13}$$

$$\nu_{H_2} = -(3 - \alpha) \tag{3.14}$$

$$\nu_{Cn} = \alpha^{n-1}(1 - \alpha)^2 \tag{3.15}$$

The expressions for chain growth probability and overall reaction rate are functions of temperature and the concentrations of hydrogen and carbon monoxide only. As the

stoichiometric coefficients solely depend on the chain growth probability, it is sufficient to solve the mass transport equations (3.1) and (3.2) exclusively for hydrogen and carbon monoxide.

3.2.4 Objective of the simulation

Simulation of reaction-diffusion equations computes coupled variables as spatial distribution over the catalyst layer thickness. These variables are hydrogen and carbon monoxide concentrations, reaction rate, temperature, chain growth probability and the resulting stoichiometry. Computation utilizes transport equations, kinetic equations, material properties and parameters to estimate the values for all distributed variables. For evaluation and comparison of the overall reactivity of different catalyst layers, the catalyst efficiency is a measure, which compares the apparent reaction rate with the surface reaction rate (equation (3.16)). Since catalyst layers with a certain amount of transport pores exhibit a lowered amount of the catalytically active phase the efficiency has to be corrected by the residual fraction of catalytically active phase (equation (3.17)) leading to the layer efficiency. For this new quantity, the volume of the catalyst layer serves as reference volume, which facilitates a reliable comparison of different layer productivities.

$$\eta_{\mathrm{Cat}} = \frac{1}{t}\int_0^t \frac{r_{CO}(x)}{r_{CO}(x=0)}\,dx \tag{3.16}$$

$$\eta_{\mathrm{Lay}} = (1-\varepsilon_{TP})\frac{1}{t}\int_0^t \frac{r_{CO}(x)}{r_{CO}(x=0)}\,dx \tag{3.17}$$

To evaluate the fraction of desired products, which are assumed to consist of hydrocarbons with carbon numbers of 5 or higher, the C_{5+} selectivity on a carbon mass basis is calculated as a function of spatial stoichiometric coefficients, which directly depend on the chain growth probability (equation (3.18) and (3.19)). For further classification of the values obtained with this equation, the methane selectivity is calculated according to equation (3.20). From these equations, the effective selectivities are accessible via integration over the whole layer thickness and averaging with the reaction rates (equation (3.21) and (3.22)).

$$S_{\mathrm{Cn}}(x) = n\alpha(x)^{n-1}\big(1-\alpha(x)\big)^2 \tag{3.18}$$

$$S_{C5+}(x) = 1 - \sum_{n=1}^{4} S_{Cn}(x) = \big(5 - 4\alpha(x)\big)\alpha(x)^4 \tag{3.19}$$

$$S_{C1}(x) = \big(1 - \alpha(x)\big)^2 \tag{3.20}$$

$$S_{C5+,\mathrm{eff}} = \frac{\int_0^t r_{CO}(x) \cdot S_{C5+}(x)dx}{\int_0^t r_{CO}(x)dx} \tag{3.21}$$

$$S_{C1,\mathrm{eff}} = \frac{\int_0^t r_{CO}(x) \cdot S_{C1}(x)dx}{\int_0^t r_{CO}(x)dx} \tag{3.22}$$

Typically, space time yield, STY, is used to compare the productivity of different reaction systems. In this particular case--due to the flat geometry of the catalyst layers and fixed gas composition--gradients in concentration will only appear in the direction of the layer thickness. This means that the absolute overall productivity scales nonlinearly with the thickness but is proportional to the geometric surface area of the catalyst layer. Thus, an area-specific quantity denoted by areal time yield, ATY, is a better reference and therefore used as an objective function for evaluation of transport pore effects on mass transport. ATY can be calculated from the distributed variables of reaction rate and C_{5+} selectivity (equation (3.23)) and is also equal to the molar flux of C_{5+} carbon species leaving the layer.

$$ATY = (1 - \varepsilon_{TP}) \int_0^t r_{CO}(x) \cdot S_{C5+}(x)dx \tag{3.23}$$

The focus of this investigation is to find the maximum productivity of an optimally designed catalyst layer. For wall coated micro-reactors, but also egg-shell catalysts and washcoated monoliths, catalyst inventory rises with increasing layer thickness. This implies the demand to fill as much catalyst as possible into the reactor by increasing layer thickness but simultaneously avoiding diffusion limitations. Hence, one objective is to find the layer thickness that yields the highest productivity. The other objective is to evaluate the influence of transport pore fraction on the achievable productivity. Therefore, two degrees of freedom are available namely the catalyst layer thickness and the transport pore fraction. The ATY is advantageous for the desired evaluation, since it allows performing the optimization towards both parameters, while evaluating catalyst efficiency or STY is only insufficient for this task (see detailed discussion in the

appendix). However, for comparison of layers with the same thickness, only efficiency and selectivity have to be considered as thickness and surface reaction rate remain constant.

3.2.5 Physical properties

Computation of the mass transport equation requires certain properties of hydrogen and carbon monoxide. The gas phase is supposed to be ideal and to contain only hydrogen and carbon monoxide at a fixed H_2/CO ratio of 2 at a temperature of 493.15 K and a pressure of 21 bar. Thus, concentration and diffusivity of the reactants in the liquid phase only depend on the liquid solvent. Although the reaction produces a broad distribution of hydrocarbons, the liquid phase is assumed to consist of only one species for estimation of liquid solubility and diffusivity. For a paraffin with a carbon number of 28, the liquid molar volume and the Henry constants for hydrogen and carbon monoxide are calculated as reported by Marano and Holder [58]. Diffusivities of hydrogen and carbon monoxide are calculated in accordance with an approach from Erkey et al. [59] The resulting properties for the reaction conditions are listed in table 3.3.

Table 3.3: Reaction conditions and properties of the solutes hydrogen and carbon monoxide for n-octacosane as solvent.

Parameter	Value	Unit
T_0	493.15	K
p	21	bar
H_2/CO	2.0	mol/mol
c_{H_2}	52.46	mol/m^3
c_{CO}	33.07	mol/m^3
H_{H_2}	458.6	bar
H_{CO}	363.8	bar
v_L	0.5818×10^{-3}	m^3/mol
D_{CO}	14.30×10^{-9}	m^2/s
D_{H_2}	36.05×10^{-9}	m^2/s

3.3 Simulation Results

3.3.1 Intrinsic reaction rates

Figure 3.2 displays the consumption rate of CO, the C_{5+} selectivity and the resulting formation rate of C_{5+} hydrocarbons as a function of reactant gas composition.
Since no mass transport effects are considered and only the kinetic expressions are relevant, the rates are denoted as intrinsic. At small H_2/CO ratios, where the concentration of carbon monoxide is high, the C_{5+} selectivity reaches maximum values. However, the inhibiting effect of carbon monoxide in the kinetic expression (Equation (3.7)) limits the achievable reaction rate. On the contrary, a low carbon monoxide concentration promotes the overall reaction rate but confines the C_{5+} selectivity due to the high H_2/CO ratio. These opposite trends lead to a maximum of the formation rate of desired products at a distinct value for the H_2/CO ratio of slightly above 3. Although diffusional effects will lower the concentration of both reactants in the catalyst layer, a shift in the reactant ratio will also appear, especially as CO and H_2 exhibit different diffusivities.

3.3.2 Reaction-diffusion effects – limitation of layer thickness

Figure 3.3 illustrates the effect of coupled reaction and diffusion on the spatial concentration profiles inside catalyst layers of different thickness without any transport pores. The concentration is normalized to the concentration of hydrogen at the gas-solid boundary, which is given in table 3.3. As this is the highest observed concentration, the normalized concentration profiles of figure 3.3 range between values of zero and unity. Additionally, the resulting chain growth probability is plotted in the same figure. For the smallest thickness of 10 µm, gradients in concentration are almost absent and the normalized concentrations remain constant at a value of unity for hydrogen and about 0.63 for carbon monoxide (figure 3.3, top left). This increased carbon monoxide concentration results from the lower Henry coefficient of CO compared to H_2 (table 3.3), which leads to a better solubility of CO (equation (3.2)). Thus, the H_2/CO ratio inside the liquid is 1.59 for a value of 2 in the gas phase. The chain growth probability also stays at a level of about 0.89, due to the absence of gradients.

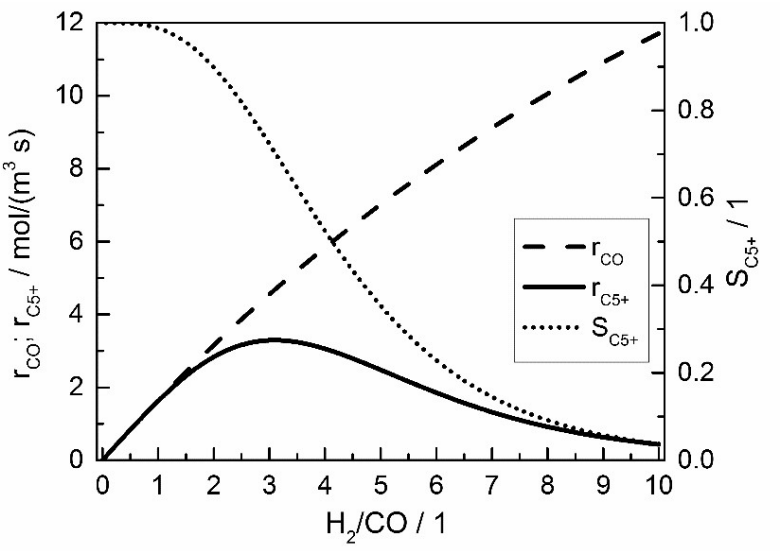

Figure 3.2: Calculated CO consumption rate, C_{5+} selectivity and formation rate of C_{5+} hydrocarbons for different H_2/CO ratios in the gas phase without diffusion effects and based on literature kinetics [18,56,57], conditions as in Table 3.

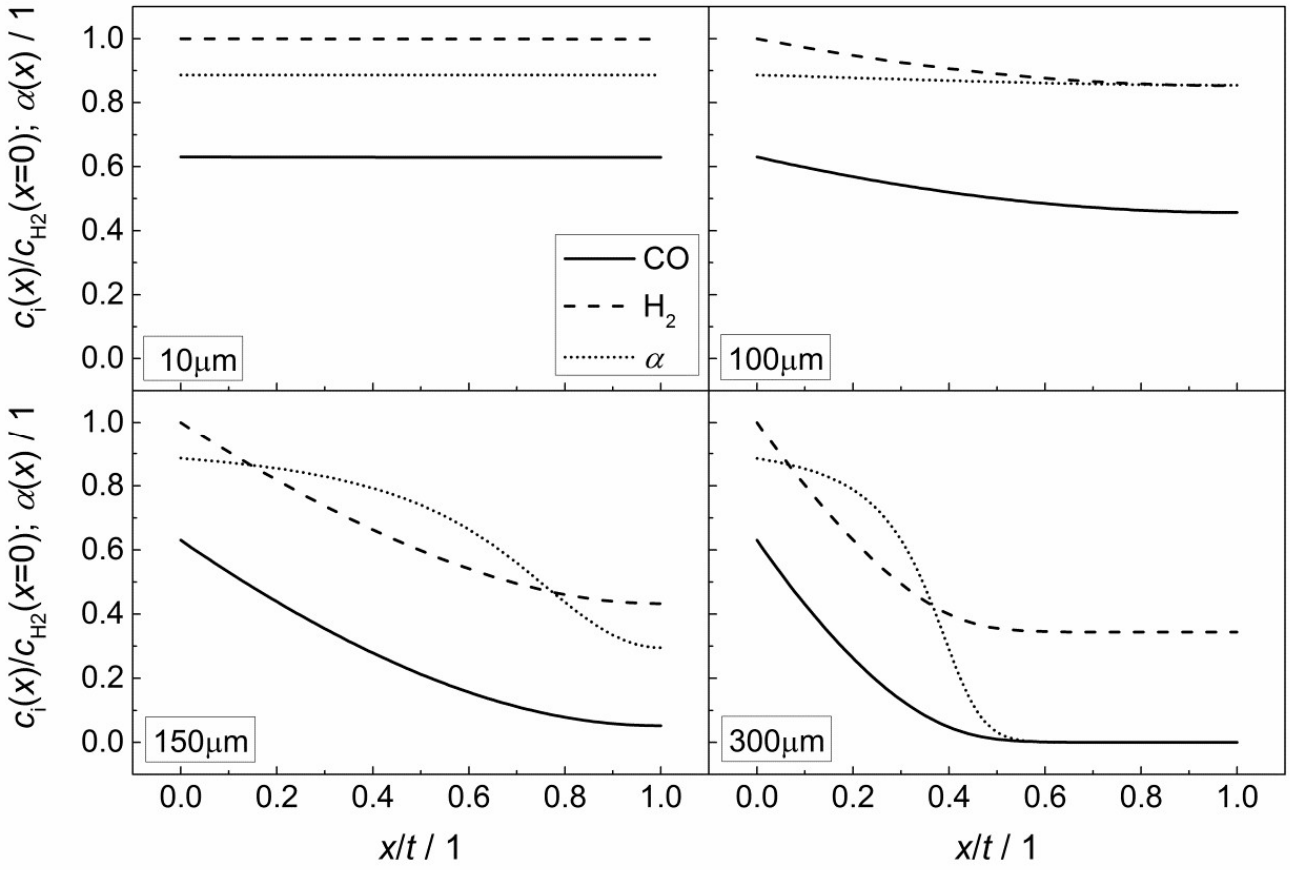

Figure 3.3: Concentration profiles of hydrogen and carbon monoxide as well as corresponding chain growth probability for catalyst layers of different thickness without transport pores; concentration normalized to the surface concentration of hydrogen.

With increasing diffusion length, concentration gradients start to form as can be seen for a layer thickness of 100 µm (figure 3.3, top right). Although the relative concentrations of hydrogen and carbon monoxide drop to 0.85 and 0.45, respectively, the influence on the chain growth probability is almost negligible. However, after a further increase of the layer thickness to 150 µm (figure 3.3, bottom left), a severe drop of reactant concentrations appears. At the wall boundary, the normalized concentration of carbon monoxide is decreased to 0.05 whereas the concentration of hydrogen still remains above 40% of the original value. As a result, the H2/CO ratio reaches a value of about 8 at this position, thereby diminishing the chain growth probability to 0.30. For an even larger layer thickness of 300 µm (figure 3.3, bottom right), the concentration of carbon monoxide reaches a value of virtually zero directly behind the middle of the layer thickness and from this point on, the concentration of hydrogen persists at about one-third of its initial value. This almost total absence of CO causes a drastic increase of the H_2/CO ratio which leads to a chain growth probability of effectively zero. In particular, the last two cases illustrate that the better diffusivity of hydrogen compared to carbon monoxide leads to an increased H_2/CO ratio, which negatively affects the chain growth probability. Neither the better solubility of carbon monoxide nor the more than twice as high consumption rate of hydrogen compensate this effect.

In accordance with figure 3.3, the CO consumption rate as well as methane and C_{5+} selectivity profiles are depicted in figure 3.4 for four catalyst layers of different thickness. The reaction rate is normalized to the intrinsic value at the surface boundary. Since no substantial concentration gradients occur at a layer thickness of 10 µm, the reaction rates and selectivities exhibit a constant value (figure 3.4, top left). For the 100 µm layer, the minor concentration gradients with a slight increase in local H_2/CO ratio result in an only minor change of methane selectivity from 0.01 at the surface to a value of 0.02 at the wall boundary. Nonetheless, the C_{5+} selectivity is already quite clearly influenced and decreases from 0.90 to 0.84. However, due to the increased H_2/CO ratio, the inhibiting effect of CO on the reaction rate is reduced and the rate rises to 12% above the intrinsic value (figure 3.4, top right). These contrary trends for C_{5+} selectivity and reaction rate become more relevant at a layer thickness of 150 µm. Although the concentration of carbon monoxide is only marginally above zero in proximity to the wall, a normalized rate of 1.87 is calculated at this position (figure 3.4, bottom left). Because of the increased local H_2/CO ratio the C_{5+} selectivity is now severely diminished and at the wall only 3% of the converted carbon monoxide participates in the production of desired C_{5+} products, whereas almost 50% is converted to methane. At a layer thickness of 300 µm, the concentration profile of carbon monoxide reaches zero at approximately

half of the thickness and consequently, the reaction is stopped. However, the profile of reaction rate exhibits a strong increase up to this point and drastically drops when almost all carbon monoxide is consumed. This leads to a distinctive maximum in the reaction rate profile for catalyst layers with strong mass transfer limitations. At the point of maximum reaction rate, the C_{5+} selectivity reaches zero and methane selectivity considerably increases towards unity. This means that an effective contribution to the production of C_{5+} hydrocarbons is limited to the first third of the catalyst layer. Any additional catalyst thickness can be denoted as dead volume since the formation rate of C_{5+} is practically zero. The profiles of selectivity and reaction rate reveal that increasing the layer thickness has a negative effect on the selectivity for desired products and a more complex effect on the efficiency as reaction rate displays a maximum. Especially the last case with 300 µm thickness is in good agreement with previously reported results from Vervloet et al. [18]. The concentration profiles are quite similar, but since reaction conditions differ slightly and a spherical model instead of a planar geometry was used, the dimensionless rate profile exhibits a higher maximum with a normalized rate above 2.5 in the work of Vervloet et al.

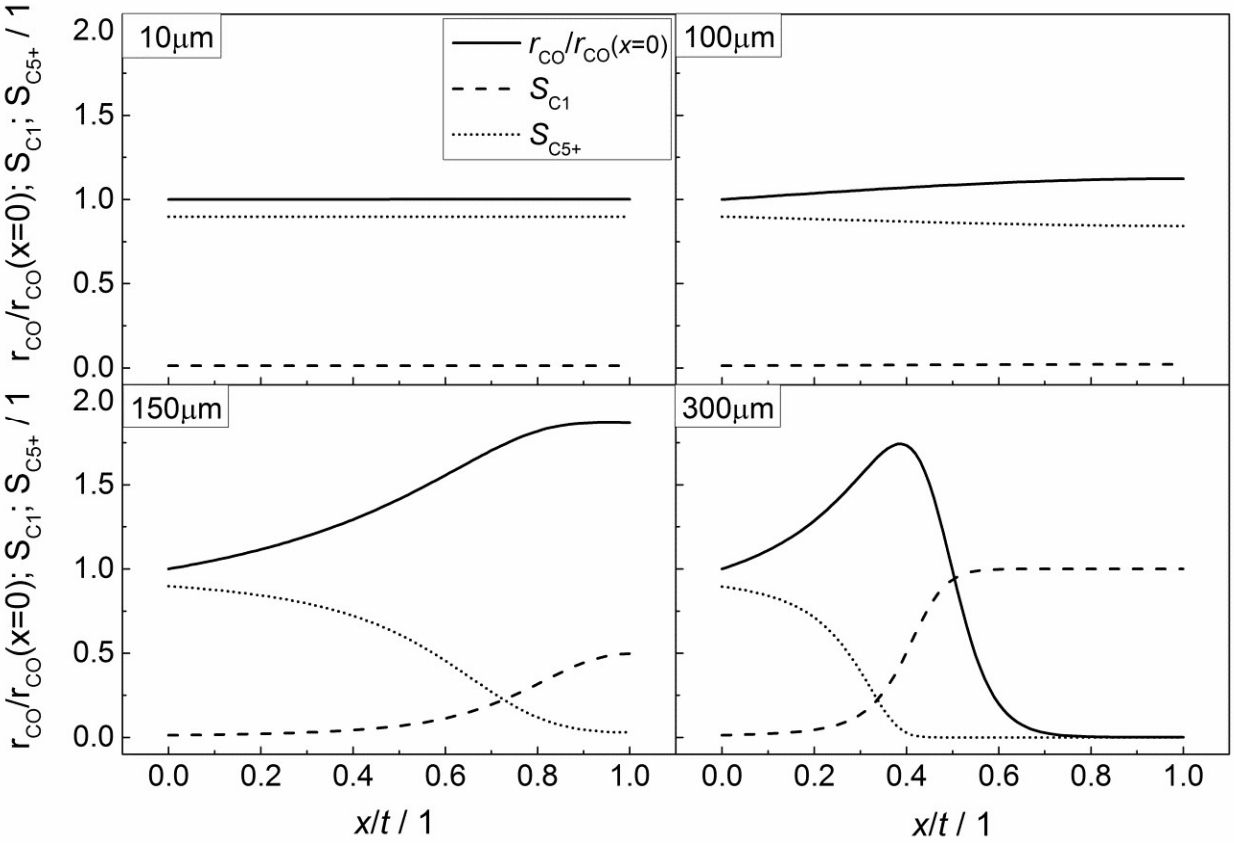

Figure 3.4: Spatial distribution of normalized CO consumption rate, methane selectivity and selectivity to C_{5+} hydrocarbons for catalyst layers of different thickness without transport pores.

For comparison of the productivity of catalyst layers with different thickness, effective selectivities, efficiencies and ATY are shown in Figure 5. On the basis of the ATY, the productivity can be divided into three different regions. In the first one, ranging up to a layer thickness of approximately 100 µm, concentration gradients are not relevant. This means that ATY is directly proportional to the layer thickness as C_{5+} selectivity and reaction rate remain close to the intrinsic values, which transforms the integral in equation (23) into the product $ATY = (1-\varepsilon_{TP})\, r_{CO} \cdot S_{C5} \cdot t$. In the next region for thicknesses ranging from ca. 100 µm to 160 µm, concentration gradients develop, leading to partially opposing tendencies for efficiency and selectivity. As the increase in layer efficiency compensates the decreased selectivity only to some extent, a maximum for the ATY at a layer thickness of 139 µm occurs. Though from this point on the layer efficiency still increases to its maximum of 1.45 at 151 µm, a higher efficiency does not lead to a higher ATY as the drop in C_{5+} selectivity is too severe. Above a layer thickness of about 160 µm C_{5+} selectivity and ATY remain constant. This marks the third and last region from which on any further increase in layer thickness would only result in an additional amount of active phase that does not contribute to the formation of desired products. Figure 3.5 displays a characteristic profile of the ATY that allows finding a certain layer thickness which produces the highest achievable amount of desired products for catalyst layers without transport pores. Hence, it provides a reference for evaluating the effect of transport pores on mass transport enhancement and improving catalyst layer productivity. This reference is denoted as optimum for "dense" layers.

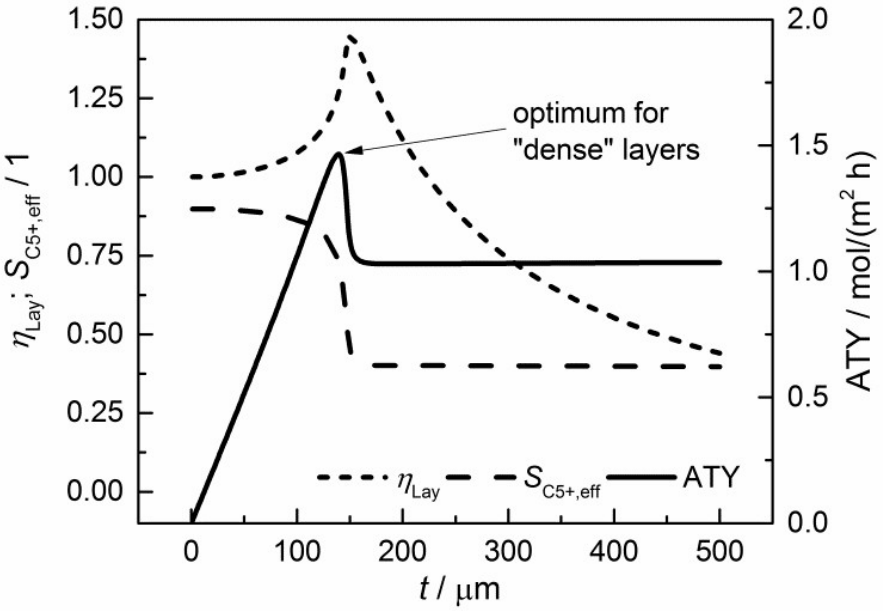

Figure 3.5: Integral values for catalyst efficiency, C_{5+} selectivity and areal time yield of catalyst layers without transport pores as a function of thickness.

3.3.3 Mass transfer improvement by transport porosity optimization

Results of a systematic variation of transport porosity for a case with a layer thickness of 300 µm and a transport pore tortuosity of one are shown in Figure 3.6. Transport porosity is varied from the lower theoretical boundary of zero to a maximum value of 0.99. The effective values for layer efficiency, selectivities and ATY are plotted as a function of the transport porosity. A catalyst layer of 300 µm exhibits a strong influence of concentration gradients if no transport pores are present. As a result, the efficiency is limited to about 0.74, the C_{5+} selectivity is fairly low, with about 0.40 and the methane selectivity of 0.32 is quite high. With increasing transport porosity the selectivity to C_{5+} hydrocarbons and methane remain unaffected up to a porosity of 25%. Only the layer efficiency rises, which can be attributed to an improved accessibility of deeper catalyst layer fractions.

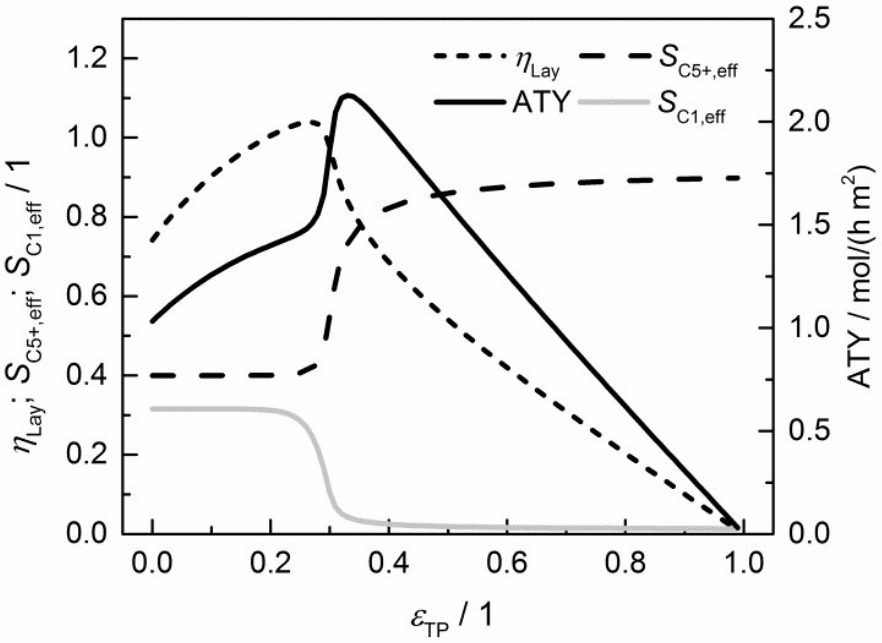

Figure 3.6: Layer efficiency, areal time yield, C_{5+} and methane selectivity of a 300 µm thick layer as a function of transport pore fraction.

As long as an enhanced access of reactants, especially carbon monoxide, does not prevent a concentration drop towards zero, a high local H_2/CO ratio still prevails and results in constant selectivities. With further increasing porosity, the negative effect of high local H_2/CO ratios disappears and selectivities rapidly approach their intrinsic values. On the other hand, the positive effect of high H_2/CO ratios on reaction rate vanishes as the diffusive transport is enhanced. Together with a reduced amount of active phase, this leads to decreasing layer efficiency. At high fractions of transport pores, diffusive

transport is fast enough for almost intrinsic behaviour throughout the catalyst layer. Thus, efficiency drops proportionally to the residual amount of the catalyst phase. As a consequence, the ATY is only slightly enhanced by increased efficiency up to a porosity of 25% but fairly benefits from an improved selectivity passing a maximum at a porosity of 33% before it declines in accordance with the layer efficiency at higher porosities. At maximum, the achievable productivity is more than twice as high as for the case without transport pores. Figure 3.6 nicely demonstrates the positive effect of the optimal fraction of transport pores. However, one should keep in mind that not only transport pore fraction but also layer thickness is required to be optimized in order to compare only the best points to determine a reliable improvement. For this purpose, the results of a single layer optimization of transport porosity, as previously discussed, are condensed in Figure 3.7 for catalyst layers ranging from 0 to 500 µm.

For each layer thickness, the maximum productivity, represented by ATY, the corresponding layer efficiency, C_{5+} selectivity and the required transport porosity are collected. Thus, figure 3.7 represents the optimization results for each single layer thickness. For thin layers, diffusion limitations are absent and additional transport pores only have a negative effect, as they reduce the fraction of active phase. Hence, up to a layer thickness of 135 µm, catalytic layers without transport pores yield the highest ATY and the plots are equivalent to figure 3.5. But from this thickness on the introduction of transport pores enhances the achievable productivity. The C_{5+} selectivity remains almost

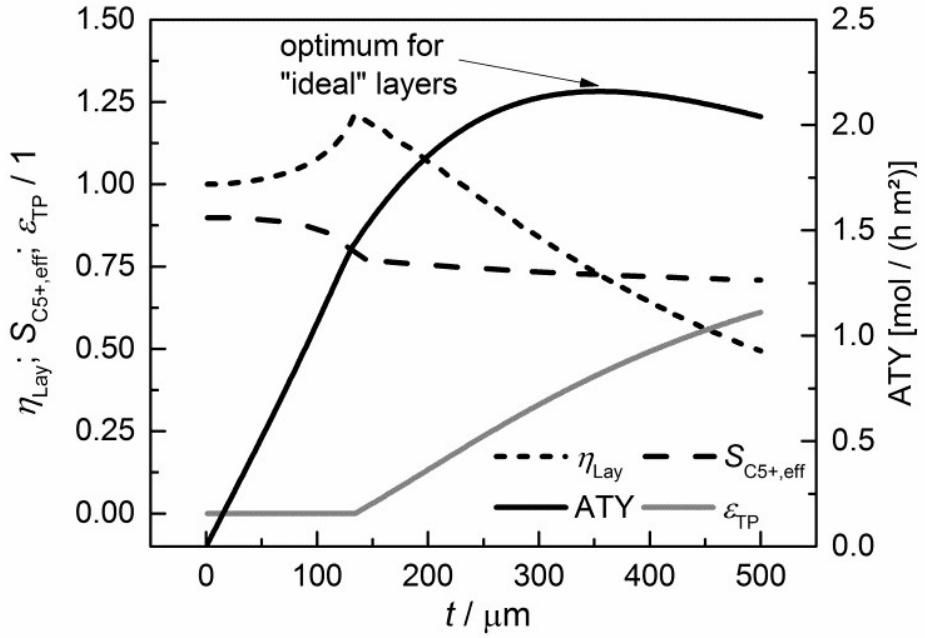

Figure 3.7: Layer efficiency, C_{5+} selectivity, transport pore fraction and ATY of optimized catalyst layers as a function of thickness.

constant at values between 0.9 and 0.7 and a distinct maximum of layer efficiency is extenuated leading to a typical, hyperbolic decrease with increasing layer thickness. The necessary fraction of transport pores rises non-linearly from zero to above 60% at a layer thickness of 500 µm. The increasing transport porosity enables to increase the values of ATY for high thicknesses significantly above the level of non-optimized layers. Nonetheless, it is not possible to continue the linear increase of ATY by optimization of transport porosity and even for this ideal case, a maximum of ATY over the layer thickness appears. The maximum achievable ATY at the ideal transport pore fraction of 0.43 and at an ideal thickness of 356 µm is about 47% higher than the maximum for "dense" layers without transport pores. The thickness where the maximum occurs is significantly shifted to higher values, but since transport pores are required to obtain these higher thicknesses the amount of catalyst is not increased proportionally. For the optimum case, the layer thickness at maximum ATY corrected with the residual fraction of the catalyst phase of 0.57 exhibits a value of 204 µm. This is 47% higher than for the dense case and underlines that the enhanced ATY is directly related to an increased amount of catalyst. Moreover, transport pores are necessary at this elevated diffusion length to preserve a concentration profile with minor gradients. These minor gradients allow maintaining a relatively high C_{5+} selectivity of 0.73, which is almost identical to the C_{5+} selectivity for the optimum of the dense case (figure 3.5).
At first sight, an enhancement of only 47% appears to be relatively low compared to improvements through addition of transport pores reported in the literature [48]. However, it has to be taken into account that only the maxima of ATY for the dense and the ideal case are compared. This comes along with different values for transport porosity and layer thickness. If one would compare the productivity at a certain layer thickness only, significantly higher values are obtainable, e.g. for a layer thickness of 500 µm increases up to 97% are possible. This emphasizes the necessity to compare only the maxima for different cases and to include not only the transport pore fraction but also the catalyst layer thickness during optimization.

3.3.4 Effect of tortuosity

Since the model assumes straight, cylindrical pores perpendicular to the layer surface, the tortuosity of transport pores equals unity. For real catalyst structures, this ideal value is not necessarily reached and diffusivity inside transport pores might be slower due to higher values of transport pore tortuosity. Furthermore, tortuosity of the mesoporous catalyst can be lower or higher than the assumed value for the reference

case ($\tau_{cat} = 3$). For dense and optimized, ideal layers the achievable maxima of ATY as a function of catalyst and transport pore tortuosity are shown in figure 3.8. Without transport pores, the ATY considerably decreases with rising catalyst tortuosity. For the best points with ideal transport pores, $\tau_{TP} = 1$, the overall highest productivity can be obtained at a catalyst tortuosity of one. The decline with increasing catalyst tortuosity is considerably attenuated almost leading to a constant productivity at high values of τ_{Cat}. With increasing transport pore tortuosity, the diffusivity in the additional pores slows down and thus the achievable ATY drops. For the points where the catalyst tortuosity is equal to or even lower than the transport pore tortuosity, no or only a negligible improvement can be observed. This clearly emphasizes the necessity of transport pores with high effective diffusivities in order to facilitate mass transport and to obtain a benefit. In figure 3.9, the required transport pore fraction as function of catalyst and transport pore tortuosity are plotted. With increasing catalyst tortuosity the required porosity rises indicating that especially at slow diffusion inside the catalyst an introduction of inert transport pore volume gives rise to an improvement. The similar shape of the profiles in figure 3.8 and figure 3.9 indicates that only the difference of the diffusivity inside the catalyst and the transport pores is relevant for the improvement and the required transport pore fraction.

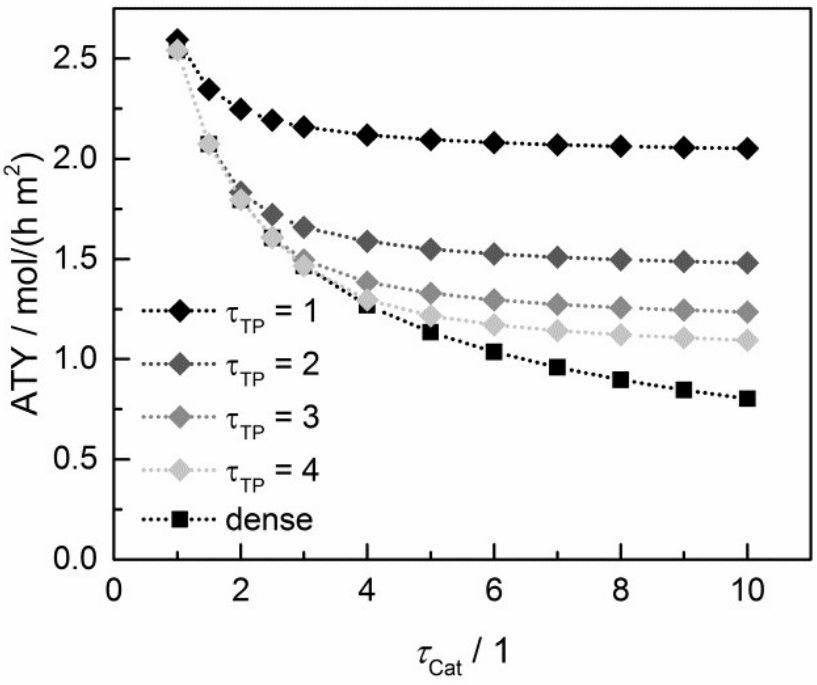

Figure 3.8: Obtainable ATY of optimized cases with ideal transport pore fraction compared to optimized cases without transport pores (dense) as a function of catalyst tortuosity and transport pore tortuosity.

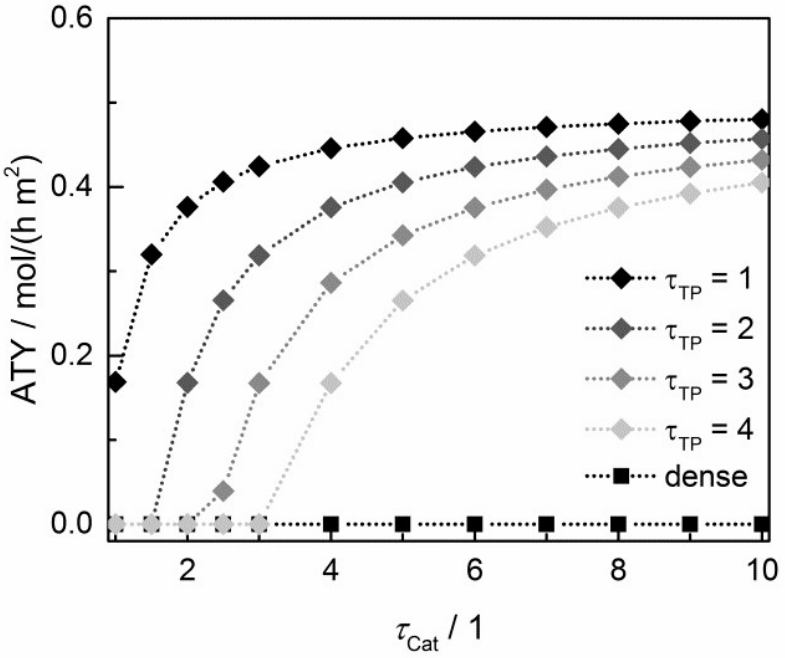

Figure 3.9: Transport pore fractions for optimized cases compared to the non-optimized, dense case as a function of catalyst tortuosity and transport pore tortuosity.

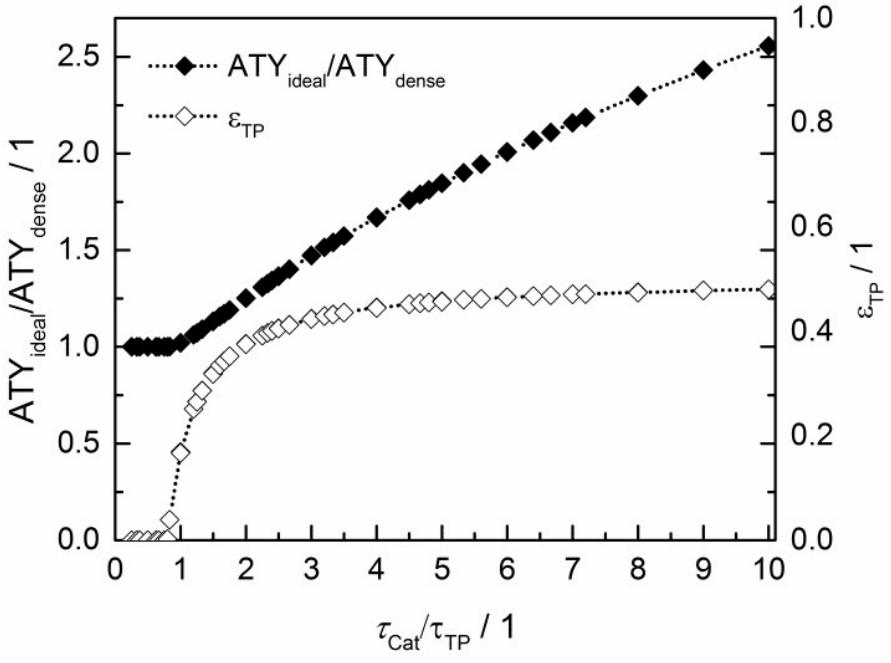

Figure 3.10: Transport pore fractions and improvement of ATY as a function of the tortuosity ratio $\tau_{\mathrm{Cat}}/\tau_{\mathrm{TP}}$.

Thus, the achievable enhancement by insertion of transport pores is directly visible as a function of the ratio of catalyst to transport pore tortuosity (Figure 3.10, calculated with the data of Figure 3.8 and Figure 3.9). It is evident that the diffusivity in the transport pores has to be faster than the diffusivity inside the catalyst to yield an effect for ATY.

Furthermore, the improvement potential increases with rising tortuosity ratio. Interestingly, the required transport porosity rapidly approaches a value close to 0.5 with an increasing tortuosity ratio. This is a very similar result as reported by Coppens and coworkers [47], who found a maximum ideal porosity of macropores of 0.5 for layers with the highest investigated Thiele moduli.

3.3.5 Maximum allowable transport pore diameter

To justify the reliability of an effective 1D model, transport pores have to be sufficiently small in order to avoid any additional transport limitations orthogonal to the main diffusion direction. Johannessen et al. [47] have derived a criterion for the necessary size of transport channels from 2D simulations for first-order kinetics and applied this to cylindrical transport pores in a hexagonal packing. For the present work, the criterion can be written as Equation (3.24), assuming CO as the limiting species, due to its lower diffusivity, and approximation of the first-order kinetics by the reaction rate and concentration at the gas-solid boundary.

$$d_{\mathrm{TP}} \leq 0.2 \sqrt{\frac{D \cdot \frac{\varepsilon_{\mathrm{Cat}}}{\tau_{\mathrm{Cat}}} \cdot c_{CO}(x=0)}{r(x=0)}} \frac{\sqrt{\frac{2\sqrt{3}}{\pi}\varepsilon_{\mathrm{TP}}}}{1-\sqrt{\frac{2\sqrt{3}}{\pi}\varepsilon_{\mathrm{TP}}}} \tag{3.24}$$

This criterion basically determines the maximal remaining wall thickness between the transport pores, in order to avoid concentration gradients inside the walls. Therefore the pore size is independent of the layer thickness and only depends on the effective diffusion and reaction inside the catalyst phase as well as the fraction of transport pores.
For catalyst tortuosities of 1, 3 and 10 the resulting wall thickness is about 49 µm, 28 µm and 15 µm, which is considerably smaller than the layer thickness at which concentration gradients appear (Figure 3.5). The transport pore diameters calculated by this criterion for three different catalyst tortuosities are shown in Figure 3.11. Even for a very low transport pore fraction of 0.01 and the highest considered catalyst tortuosity of $\tau_{\mathrm{Cat}} = 10$, the maximum allowable transport pore diameter is still about 1.8 µm. Thus, transport pores with diameters of 1-2 µm can be used over the entire range of layer thicknesses and transport pore fractions without causing additional mass transfer resistances. However, the required transport pore fraction for the optimal point is in most cases in the range of 0.4 to 0.5 (Figure 3.10). Here, the necessary transport pore diameter can be between 30 and 140 µm. This shows that remarkably large pores can be utilized to achieve an overall improvement of FTS.

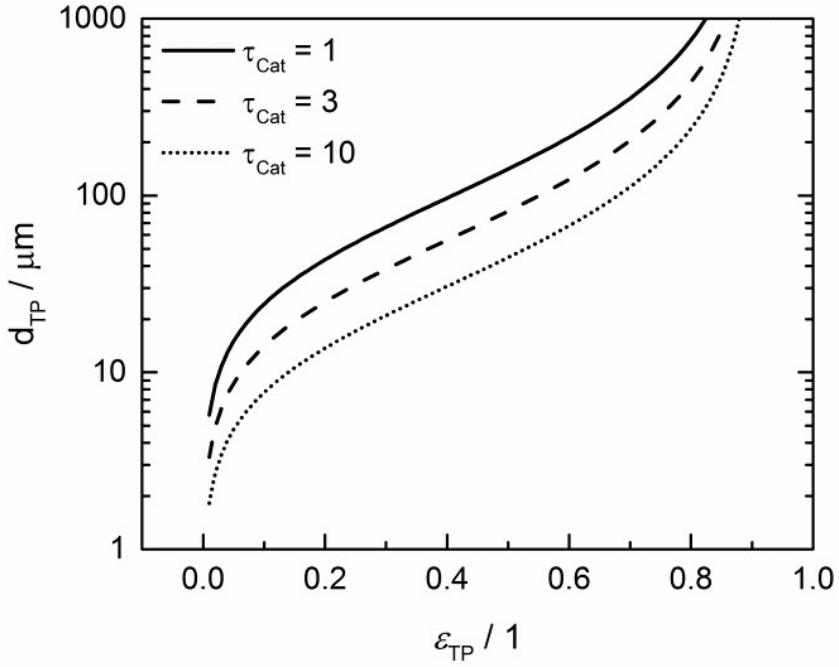

Figure 3.11: Upper limit for transport pore diameters as a function of transport pore fraction for different catalyst tortuosities; criterion derived from Johannessen et al. [47].

3.3.6 Temperature gradients

Although the main focus of this work is the enhancement of mass transport effects, we also investigated the possible appearance of temperature gradients in the catalyst layers. The maximum temperature deviations from the wall temperature occur at the gas-solid boundary as no heat flux to the gas phase was assumed. Figure 3.12 displays the temperature differences at this point as a function of layer thickness. Obviously, the temperature difference rises with increasing layer thickness. However, even for a layer of 500 µm, the calculated temperature rise is less than about 0.5 K. Consequently, any influence of the temperature distribution in the catalyst layer can be neglected.

3.4 Conclusions

Diffusion phenomena inside Fischer-Tropsch catalysts are likely to play a vital role for apparent reaction rate and selectivity towards long-chained hydrocarbons and may limit the achievable productivity. The insertion of transport pores is an interesting option to enhance catalyst productivity. For the investigation of this concept, an effective one-dimensional reaction-diffusion model using empirical kinetic equations was adapted to include transport pores as the inert phase. For a planar geometry of the catalyst, the

quantity ATY was defined and used as the objective function for productivity optimization. During optimization, it became evident that catalyst thickness and transport pore fraction have to be adjusted simultaneously in order to obtain the maximum benefit in productivity. For the investigated parameter range, an improvement of up to 150% was found, strongly depending on the effective diffusivities inside transport pores and catalyst phase. The best results are achieved if the diffusivity in the transport pores is significantly faster than inside the catalyst. In this range, a relatively constant transport pore fraction of 0.4 to 0.5 was found to be ideal. For the reference case, the productivity could be improved by about 47% with a transport pore fraction of 43%. To achieve this enhancement, the layer thickness has to be increased from 134 µm to 346 µm. The maximum allowable transport pore diameter at this point is 62 µm. As for varying tortuosities, different transport pore fractions were found to be ideal, the limit for the transport pore diameter also changed. In most cases, transport pores diameters between 30 and 140 µm can be employed without any additional mass transfer resistance between transport pore and catalyst. The calculated temperature gradients in the catalyst layer are fairly low. Thus, mass transport is the dominant phenomenon determining rate and selectivity of FTS catalysts.

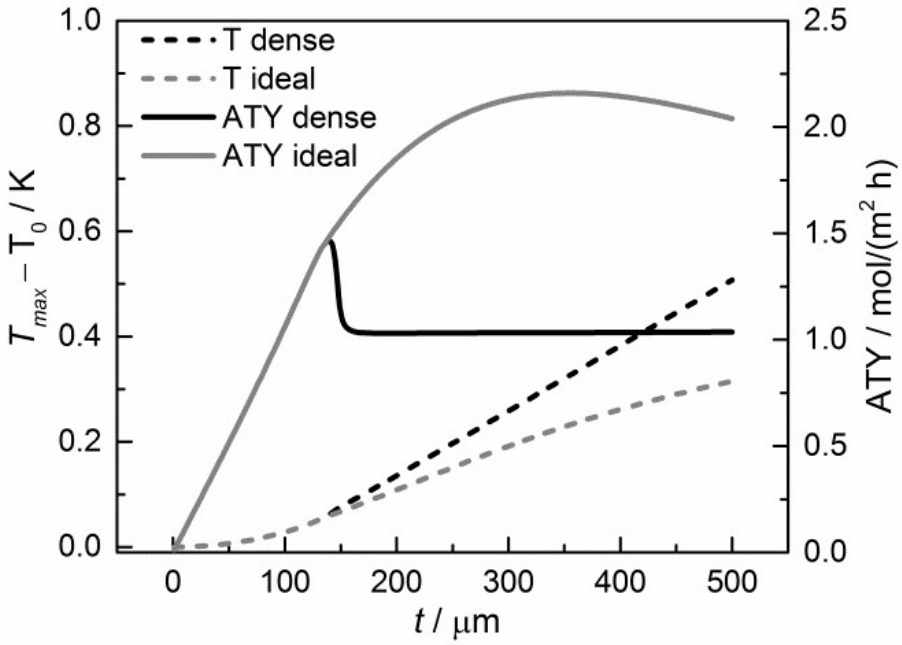

Figure 3.12: Temperature difference of maximum temperature to wall temperature and ATY of optimized, ideal, and not-optimized, dense, catalyst layers as a function of thickness; $\tau_{\mathrm{TP}} = 1$, $\tau_{\mathrm{Cat}} = 3$.

The simple model described in the present contribution illustrates that the variation of structural parameters offers considerable optimization potential for FTS catalysts. These parameters can be easily altered with common techniques of catalyst preparation such as addition of pore-forming agents or templates. These investigations are currently carried out in our group and will be presented in a forthcoming publication.

3.5 Acknowledgements

The authors gratefully thank Deutsche Forschungsgemeinschaft (DFG) for financial support through SPP 1570 (grant number TU89/9).

3.6 Notation

Latin

a	reaction rate constant, mol s^{-1} bar^{-2}
a_0	frequency factor for reaction rate constant, mol s^{-1} bar^{-2}
ATY	areal time yield of desired products, mol s^{-1} m^{-2}
b	absorption constant, bar^{-1}
b_0	frequency factor for absorption constant, bar^{-1}
$c_{i,cat}$	concentration in liquid-filled pores of catalyst phase of species i (CO or H_2), mol m^{-3}
$c_{i,TP}$	concentration in liquid-filled transport pores of species i (CO or H_2), mol m^{-3}
D_i	diffusion coefficient of species i (CO or H_2), m^2 s^{-1}
d_{TP}	diameter of transport pores, m
E_{Aa}	activation energy for reaction rate constant, J mol^{-1}
E_{Ab}	activation energy for absorption constant, J mol^{-1}
H_i	Henry coefficient of species i (CO or H_2), bar
ka_i	combined mass transfer coefficient of species i (CO or H_2), s^{-1}
k_α	selectivity coefficient, dimensionless
n	carbon number, dimensionless
p	gas phase pressure, bar
p_i	partial pressure of species i (CO or H_2), bar
R	universal gas constant, J mol^{-1} K^{-1}
r_{C5+}	formation rate of desired products, mol s^{-1} m^{-3}
r_{CO}	consumption rate of CO, mol m^{-1} s^{-1}

S_{C1} spatially distributed molar selectivity for methane, dimensionless

$S_{C1,eff}$ effective molar selectivity for methane, dimensionless

S_{C5+} spatially distributed molar selectivity for alkanes with n greater than 4, dimensionless

$S_{C5+,eff}$ effective molar selectivity for alkanes with n greater than 4, dimensionless

S_{Cn} spatially distributed molar selectivity for alkane of carbon number n, dimensionless

STY space time yield of desired products, mol $s^{-1}\,m^{-3}$

t thickness of catalyst layers, m

T temperature, K

T_0 temperature at wall boundary, K

T_{max} maximum temperature in the layer, K

T_{ref} reference temperature for selectivity expression, 493.15 K

v_L molar volume of the products liquid phase, $m^3\,mol^{-1}$

x dimension coordinate, m

H_2/CO ratio of gas-phase partial pressures of H_2 to CO, dimensionless

Greek

a chain growth probability, dimensionless

β selectivity order, dimensionless

ΔE_α selectivity expression activation energy, $J\,mol^{-1}$

ε_{cat} fraction of pores in the catalyst phase, dimensionless

ε_{TP} fraction of transport pores in the catalyst layer, dimensionless

η_{Cat} efficiency of the catalyst phase, dimensionless

η_{Lay} efficiency of the catalyst layer including transport pores, dimensionless

ν_{C30+} stoichiometric coefficient of alkanes with n greater than 29, dimensionless

ν_{Cn} stoichiometric coefficient of alkane with carbon number n, dimensionless

ν_i stoichiometric coefficient of species i (CO, H_2 or H_2O), dimensionless

ϱ_{cat} apparent density of the catalyst phase, $kg\,m^{-3}$

τ_{cat} tortuosity inside the catalyst phase, dimensionless

τ_{TP} tortuosity inside the transport pores, dimensionless

3.7 References

[1] Q. Zhang, J. Kang and Y. Wang, *ChemCatChem*, 2010, 2, 1030-1058.

[2] B. H. Davis, *Catal. Today*, 2002, 71, 249-300.

[3] M. E. Dry, *Catal. Tod*ay, 2002, 71, 227-241.

[4] R. Guettel, U. Kunz and T. Turek, *Chem. Eng. Tec*hnol., 2008, 31, 746-754.

[5] A. Jess and C. Kern, *Chem. Eng. Tec*hnol., 2012, 35, 369-378.

[6] A. Jess and C. Kern, *Chem. Eng. Techn*ol., 2012, 35, 379-386.

[7] R. Myrstad, S. Eri, P. Pfeifer, E. Rytter and A. Holmen, *Catal. T*oday, 2009, 147S, S301-S304.

[8] H. Robota, L. Richard, S. Deshmukh, S. LeViness, D. Leonarduzzi and D. Roberts, *Catal. Surv. Asia*, 2014, DOI: 10.1007/s10563-014-9175-x, 1-6.

[9] C. Knobloch, R. Güttel and T. Turek, *Chem. Ing. Tech.*, 2013, 85, 455-460.

[10] J. Knochen, R. Güttel, C. Knobloch and T. Turek, *Chem. Eng. Process.*, 2010, 49, 958-964.

[11] R. Guettel and T. Turek, *Chem. Eng. Sci.*, 2009, 64, 955-964.

[12] A. M. Hilmen, E. Bergene, O. A. Lindvåg, D. Schanke, S. Eri and A. Holmen, *Catal. T*oday, 2001, 69, 227-232.

[13] F. Kapteijn, R. M. de Deugd and J. A. Moulijn, *Catal. Today*, 2005, 105, 350-356.

[14] M. F. M. Post, A. C. Vanthoog, J. K. Minderhoud and S. T. Sie, *AIChE J.*, 1989, 35, 1107-1114.

[15] E. Iglesia, S. C. Reyes, R. J. Madon and S. L. Soled, *Adv. Catal.*, 1993, 39, 221-302.

[16] K. D. Kruit, D. Vervloet, F. Kapteijn and J. R. van Ommen, C*atal. Sci. Techn*ol., 2013, 3, 2210-2213.

[17] M. Lualdi, S. Lögdberg, G. Carlo, S. Järås, M. Boutonnet, A. Venezia, E. Blekkan and A. Holmen, *Top. Catal.*, 2011, 54, 1175-1184.

[18] D. Vervloet, F. Kapteijn, J. Nijenhuis and J. R. van Ommen, *Catal. Sci. Technol.*, 2012, 2, 1221-1233.

[19] Y.-N. Wang, Y.-Y. Xu, H.-W. Xiang, Y.-W. Li and B.-J. Zhang, Ind. Eng. Chem. Res., 2001, 40, 4324-4335.

[20] E. Iglesia, S. L. Soled, J. E. Baumgartner and S. C. Reyes, J. Catal., 1995, 153, 108-122.

[21] L. Fratalocchi, C. G. Visconti, L. Lietti, E. Tronconi, U. Cornaro and S. Rossini, Catal. Today, 2015, 246, 125-132.

[22] Y. Liu, D. Edouard, L. D. Nguyen, D. Begin, P. Nguyen, C. Pham and C. Pham-Huu, Chem. Eng. J., 2013, 222, 265-273.

[23] K. Pangarkar, T. J. Schildhauer, J. R. van Ommen, J. Nijenhuis, J. A. Moulijn and F. Kapteijn, Catal. Today, 2009, 147, Supplement, S2-S9.

[24] B. Xu, Y. Fan, Y. Zhang and N. Tsubaki, AIChE J., 2005, 51, 2068-2076.

[25] Ø. Borg, S. Eri, E. A. Blekkan, S. Storsæter, H. Wigum, E. Rytter and A. Holmen, J. Catal., 2007, 248, 89-100.

[26] A. Y. Khodakov, A. Griboval-Constant, R. Bechara and V. L. Zholobenko, J. Catal., 2002, 206, 230-241.

[27] A. M. Saib, M. Claeys and E. van Steen, Catal. Today, 2002, 71, 395-402.

[28] M. Wolters, L. J. W. van Grotel, T. M. Eggenhuisen, J. R. A. Sietsma, K. P. de Jong and P. E. de Jongh, Catal. Today, 2010, 163, 27-32.

[29] H. Preising and D. Enke, Colloids Surf. A, 2007, 300, 21-29.

[30] C. K. Colton, C. N. Satterfield and C.-J. Lai, AIChE J., 1975, 21, 289-298.

[31] C. N. Satterfield, C. K. Colton and W. H. Pitcher, AIChE J., 1973, 19, 628-635.

[32] S. Y. Lee, J. D. Seader, C. H. Tsai and F. E. Massoth, Ind. Eng. Chem. Res., 1991, 30, 29-38.

[33] E. M. Renkin, J. Gen. Physiol., 1954, 38, 225-243.

[34] M. C. Tsai, Y. W. Chen and C. Li, Ind. Eng. Chem. Res., 1993, 32, 1603-1609.

[35] T. Doğu, Ind. Eng. Chem. Res., 1998, 37, 2158-2171.

[36] N. Wakao and J. M. Smith, Chem. Eng. Sci., 1962, 17, 825-834.

[37] M.-O. Coppens and G. F. Froment, Chem. Eng. Sci., 1995, 50, 1013-1026.

[38] M.-O. Coppens and G. F. Froment, Chem. Eng. Sci., 1995, 50, 1027-1039.

[39] F. J. Keil and C. Rieckmann, Chem. Eng. Sci., 1994, 49, 4811-4822.

[40] C. Rieckmann and F. J. Keil, Chem. Eng. Sci., 1999, 54, 3485-3493.

[41] R. Güttel, Chem. Ing. Tech., 2015, 87, 694-701.

[42] G. Dogu and J. M. Smith, AIChE J., 1975, 21, 58-61.

[43] N. A. Seaton, Chem. Eng. Sci., 1991, 46, 1895-1909.

[44] J. M. C. Pereira, J. E. P. Navalho, A. C. G. Amador and J. C. F. Pereira, Chem. Eng. Sci., 2014, 117, 364-375.

[45] S. Gheorghiu and M.-O. Coppens, AIChE J., 2004, 50, 812-820.

[46] G. Wang, E. Johannessen, C. R. Kleijn, S. W. de Leeuwa and M.-O. Coppens, Chem. Eng. Sci., 2007, 62, 5110-5116.

[47] E. Johannessen, G. Wang and M.-O. Coppens, Ind. Eng. Chem. Res., 2007, 46, 4245-4256.

[48] G. Wang and M.-O. Coppens, Chem. Eng. Sci., 2010, 65, 2344-2351.

[49] H. Becker, R. Güttel and T. Turek, Chem. Ing. Tech., 2014, 86, 544-549.

[50] G. S. Armatas, Chem. Eng. Sci., 2006, 61, 4662-4675.

[51] D. Vervloet, F. Kapteijn, J. Nijenhuis and J. R. van Ommen, Catal. Today, 2013, 216, 111-116.

[52] D. S. Smith, A. Alzina, J. Bourret, B. Nait-Ali, F. Pennec, N. Tessier-Doyen, K. Otsu, H. Matsubara, P. Elser and U. T. Gonzenbach, J. Mater. Res., 2013, 28, 2260-2272.

[53] J. J. Marano and G. D. Holder, Ind. Eng. Chem. Res., 1997, 36, 2409-2420.

[54] G. Chabot, R. Guilet, P. Cognet and C. Gourdon, Chem. Eng. Sci., 2015, 127, 72-83.

[55] X. Zhu, X. Lu, X. Liu, D. Hildebrandt and D. Glasser, Chem. Eng. J., 2014, 247, 75-84.

[56] I. C. Yates and C. N. Satterfield, Energy Fuels, 1991, 5, 168-173.

[57] C. Maretto and R. Krishna, Catal. Today, 1999, 52, 279-289.

[58] J. J. Marano and G. D. Holder, Fluid Phase Equilib., 1997, 138, 1-21.

[59] C. Erkey, J. B. Rodden and A. Akgerman, Can. J. Chem. Eng., 1990, 68, 661-665.

6 Model validation

This far only separate results of computations or experiments were shown. In this chapter, the essential combination of simulation with experimental data is presented and the parameter estimation results are examined and model predictions thereupon evaluated.

6.1 Parameter estimation

6.1.1 Deactivating catalyst

Any data, obtained from experimental testing of catalysts, is a result of a catalyst being exposed to the reaction conditions for a certain period of time. For typical Fischer-Tropsch experiments, this time is in the magnitude of several hundred hours. This can lead to the catalyst becoming more active or, what is more common to see, to a degradation of the catalytic activity over time, known as deactivation. Deactivation is a continuous process, which would prevent the catalytic reactor from reaching steady-state operation when interpreted strictly. However, the rate of change for the catalytic activity is a quite slow process, with changes being visible only over hours. This leaves ample time for the syngas conversion reaction to reach a stable profile within the catalyst, because diffusion and convection, the two main transport mechanisms in the reactor, are much faster and adapt to changes in seconds and minutes. Therefore, the reactor is always assumed to be in a quasi-steady state, allowing the reactor models, as described in the previous sections to be used for evaluation of experimental data.
Nonetheless, deactivation is a process that can be caused by several different effects and taking place at different sites of the catalyst. For cobalt-based catalysts for Fischer-Tropsch synthesis, different mechanisms can affect the observed reaction rate. These mechanisms are sintering, agglomeration or migration of cobalt particles, cobalt oxidation to pure oxide or mixed oxides, carbon formation either on the cobalt or within the catalyst pores, poisoning and attrition of the catalyst [1,2]. For a fixed bed reactor attrition is unlikely, and due to the use of pure gases poisoning is also not expected to have occurred. This leaves modification to the cobalt active phase and carbon depositions as the most likely causes for deactivation. Unfortunately, even with deactivation mechanisms narrowed down it is still complicated. Several attempts to build a model that takes the catalyst deactivation into account have been suggested and could show a reasonably similar evolution of the CO conversion as the experiments [3,4]. Though this

can describe deactivation, it is not verified against the characterisation of a spent catalyst. So aside from merely fitting the time-dependent trajectories also an autopsy of used catalysts after some reaction time is required to validate the deactivation mechanisms. This has also been attempted several times [5–7], but here the difficulty is to assign a numerical quantity to the largely qualitative or only semi-quantitative results and also catalysts normally have to be transported out of the reactor into the characterisation device, introducing a possibility for error. Using in-operando methods, this can be avoided, but often the operating conditions are too demanding and the pressure has to be adjusted, often to very low levels [8]. Promising studies with a reactor inside a magnetometer circumvent these limitations and can allow for detailed insights into the evolution of the catalyst activity, but this technique is limited to the cobalt phase [9]. Despite all these achievements, the investigation of catalyst deactivation for the Fischer-Tropsch process is still a highly time-intensive task, which probably contributes to the lack of available universally applicable kinetic description of the catalyst deactivation.

Hence, the experimental results obtained in this work require a more pragmatic approach to correct for the well observable change in conversion over time to improve the modelling descriptive validity. For doing this, generally two methods can be imagined. The first requires the use of reference points, where the same operating conditions are used several times throughout a long experiment and the conversion for each point is divided by the initial conversion to yield a number, the activity factor (equation 6.1), that typically declines over the reaction time as the catalyst deactivates.

$$F(t) = \frac{X\left(t_{\mathrm{ref,n}}\right)}{X\left(t_{\mathrm{ref,0}}\right)} \tag{6.1}$$

This method can provide reliable values for the activity factor, but it would double the experimental time as ideally an activity factor for each operating condition is measured requiring an additional operating point. The prolonged experiment itself worsens the catalyst activity due to more time for deactivation. Thus, this method was not deemed ideal, because it increases the loss of activity, which it ought to compensate.

The second method can be used without this detriment and solely utilises already available data. It is based on the assumption that the activity of the catalyst is a continuous function over time with a linear decline at each operating point. For a hypothetical, ideally heated, differential reactor, with an ideal plug flow all the way to the perfect analyser, any change of the conversion would be directly caused by either a change in the operating conditions or the catalyst activity. Therefore, a relation between

the extensive reaction rate for CO, R_{CO}, the feed flow of CO, $\dot{n}_{CO,in}$, the activity factor, F, and the CO conversion, X, can be written as equation 6.2.

$$X(t) = F(t) \cdot \frac{R_{CO}(T, c_{gas})}{\dot{n}_{CO,in}} \tag{6.2}$$

Here it is already implied to have constant operating conditions as temperature, gas composition and feed flow are assumed to be constant. This enables rewriting to

$$\frac{X(t)}{X_0} = \frac{F(t)}{F_0} = \frac{r_{CO}(T, c_{gas})}{\dot{n}_{CO,in}} = const \tag{6.3}$$

equation (6.3) and further means that any time-dependent evolution of the activity factor can be derived from the conversion when the initial values are known. Now, assuming a linear gradient for the conversion, and the activity (equation 6.4),

$$\frac{d}{dt}\left(\frac{F(t)}{F_0}\right) = \frac{d}{dt}\left(\frac{X(t)}{X_0}\right) \tag{6.4}$$

this equation directly leads to a form providing the activity factor as a function of time (equation 6.5):

$$F(t) = F_0\left(1 + \frac{d}{dt}\left(\frac{X(t)}{X_0}\right)\Delta t\right) \tag{6.5}$$

This means the activity can be extrapolated on the basis of the time derivative within an operating time period, where the initial activity is known and the operating conditions are the same. When operating conditions vary, the reaction rate and hence the conversion will follow accordingly to the kinetics. However, when the step in the operating conditions is sufficiently fast, the change in activity during the step time is negligible and one can formulate for a change from a general operating point n to the subsequent operating point n+1 (equation 6.6 and 6.7):

$$F_{n+1,0} = F_n(t_{n,end}) \tag{6.6}$$

$$F_{n+1} = F_n(t_{n,end})\left(1 + \frac{d}{dt}\left(\frac{X(t)}{X_0}\right)_{n+1}\Delta t\right) \tag{6.7}$$

So, as long as a starting activity factor is assigned, which naturally would be one, the entire trajectory for the activity factor can be calculated. However, this statement is valid only for reactors where the deactivation is linear and one activity factor for the

entire reactor suffices. For real experimental data, these assumptions are idealisations, which may only be true for specific cases. For an integral reactor, the various deactivation mechanisms would occur in different places as the spatial concentration and temperature profiles would affect the reaction rates for deactivation as well as the rate for the main reaction. In combination, this makes the rate of change of the CO conversion only a measure for an estimated loss of activity. But this is still considerably better than no factor at all and therefore was applied to the experimental data of this work.

Exemplary experimental data to illustrate a typical profile is shown in figure 6.1 for a catalyst with transport pores and a thickness of 183 µm. During the initial activation phase after reduction, the temperature is stepped up by 10 K every 12 h starting from 150 °C until a temperature of 190 °C. From that point on a quantifiable conversion is measured and each point is held at least 24 h to obtain data that is only affected by deactivation. At least the last ten points at each temperature level are used to estimate the rate of change for the conversion. From that, the activity profile is estimated, assuming that at the first temperature of 190 °C an activity factor of one holds. Any data from before that is associated with an assigned activity factor of one but also excluded from parameter estimation. The activity profile exhibits a rather severe deactivation at the beginning, but the deactivation rate slowly fades until, at the final temperature, there is even a slight increase in activity. In total, over a period of nearly 300 h, the activity decays to a value of just below 60%. This illustrates the necessity for a correction as otherwise, any parameter estimation would suffer from severe inaccuracies, preventing a decent fit of the model to the experimental data.

Because of the number of experiments conducted, illustrating all in terms of deactivation would be futile. Only a condensed overview for the two types of catalyst layers is therefore shown. All experiments were undergoing the same principle analysis programme, with a stepwise increase in temperature that was hold for a sufficient time period at each temperature from 190 °C onwards up to the maximum temperature of 240 °C with an increment of 10 K. So, in figure 6.2 the deactivation rate is plotted as function of the operating temperatures for the not compacted layers, with transport pores, and for the compacted ones, without transport pores. Because of the scattering of the available data, confidence intervals for each level are also shown. At the starting temperature of 190 °C, the uncompacted layers are on average almost not deactivating, whereas the compacted layers deactivate a fair bit. But as soon as the temperature rises to 200 °C, deactivation for the layers with transport pores jumps to its lowest level, exceeding the deactivation rate for the compacted layers, which only modestly worsens. From this point onwards the deactivation rate for both types slowly approaches zero.

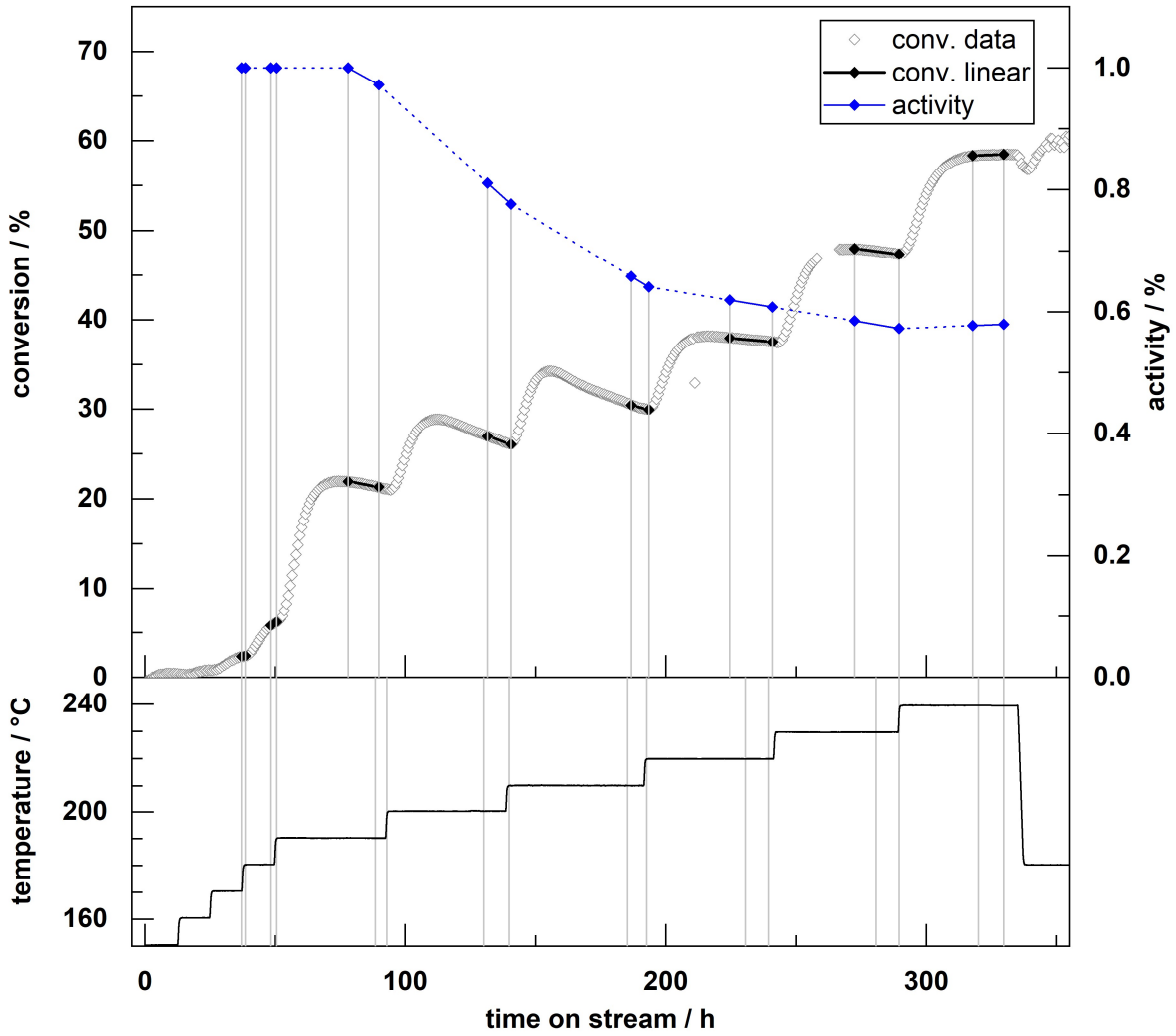

Figure 6.1: Conversion and derived activity as a function of time. Ranges for estimation of deactivation rate and linearised reactor conversion are additionally indicated; temperature profile is added to the bottom. The thickness of the catalyst layer with transport pores is 183 µm; GHSV = 5000 h^{-1}, p =21 bar, $H_2/CO = 2$, $CO/Ar = 9$.

This leads to the deactivation rate for the uncompacted layers being always a bit lower and therefore leading to a greater extent of activity loss for this type. Only at the two highest temperatures, the uncompacted layers are slightly better off in terms of deactivation rate than the compacted ones, but the difference is fairly minute. This more severe behaviour for the layers with transport pores is also mirrored by the development of the activity factors (figure 6.3). Both types start off with 100% of activity, but right from the beginning, there is a substantial drop after the first temperature increment. For the uncompacted layer, this is the highest drop of all temperature levels, whereas the compacted layers exhibit a relatively constant drop. Hence for the next temperature levels, the compacted layers continue to decline by about 7% of the initial activity per

temperature step, but the layers with transport pores have already lost about 20% activity after the first step and appear to stabilise with only a lower change of about 5% per step. At 220 °C, the uncompacted layers exhibit their minimum in activity at a value of about 70% from which point on the activity starts to increase slightly, closing the gap to the activity of the compacted layers. The compacted layers, on the other hand, drop with an almost constant gradient to the minimum at 230 °C of about 75% of the initial activity. Thus, the activity at 240 °C is again modestly higher and almost identical to the not compacted layers. The on average lower value for layers with transport pores make the attempt to show a benefit from utilising transport pores more challenging and contributes to the lack of clear evidence for this expected improvement in the experimental data, as shown in section 4. The entire approach to correct the activity to improve the quality and clearness of the obtained experimental data is based on the expectation that dynamic changes to the catalyst only affect the main reaction of CO consumption. But in reality, deactivation is highly likely to also have an impact on the selectivity as the catalyst degrades over time. Correcting for this is, however, much more complicated, and was not attempted, as it would have required additional data concerning the distribution of the activity after deactivation.

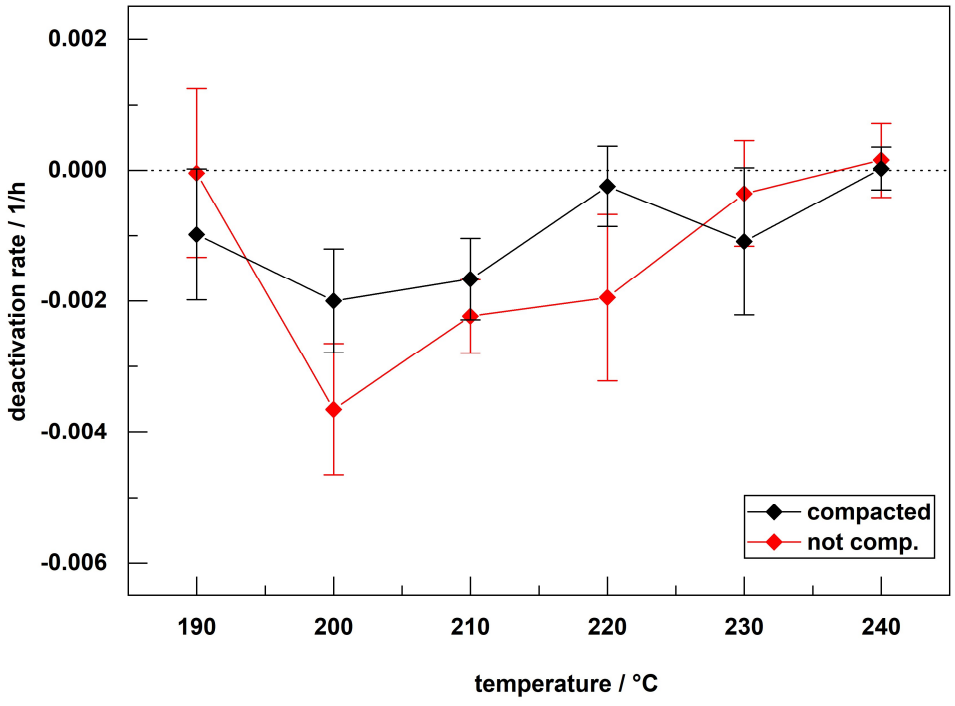

Figure 6.2: deactivation rates of catalysts as function of operating temperature for compacted and not compacted layers, error bars indicate confidence interval for 90% probability.

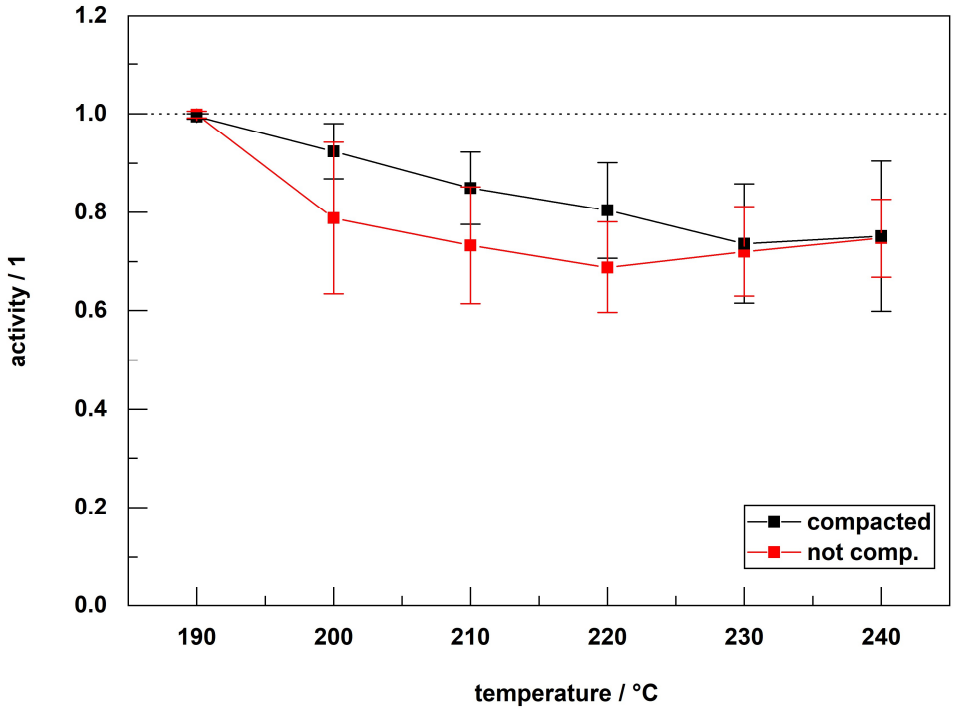

Figure 6.3: Activity of catalysts as function of operating temperature for compacted and not compacted layers, error bars indicate confidence interval for 90% probability.

6.1.2 Enhanced selectivity model

For the description of the selectivity, the model uses an explicit function to estimate the local chain growth probability, which is used as a single parameter to describe the entire product spectrum. That function depends on the temperature and the concentration ratio between the two reactant species, which is affected by the H_2 concentration and the concentration of CO, respectively. This function developed by Vervloet et al. [10] is not rigorously based on a microkinetic analysis, but was derived on the assumption that the chain growth probability results from chain termination and chain propagation rates. Additionally, both rates are of course also affected by temperature, included via an Arrhenius term, resulting in a function that approaches one, for low temperatures and low H_2 to CO ratios, and zero for high temperatures and high ratios (equation 6.8).
To further accommodate the deviation of the methane selectivity, which is often substantially higher than expected from a strict ASF-distribution, Förtsch et al. [11] introduced a new parameter, the termination probability for methane. It accounts for an additional pathway for the formation of methane apart from the conventional termination rate proposed by a simple ASF-model (equation 6.9). This parameter is already used in the integral model of the previous paragraph, but only a constant value

of 0.5 was applied. When looking at the definition of these two parameters, it becomes obvious, that when applying similar assumptions as for the chain growth probability, the termination probability for methane is also influenced by temperature and the reactant concentrations.

$$\alpha = \frac{rate_{\text{propag.}}}{rate_{\text{propag.}} + rate_{\text{termin.}}} = \frac{k_p(T) \cdot c_{\text{CO}}}{k_p(T) \cdot c_{\text{CO}} + k_t(T) \cdot c_{\text{H}_2}} = \frac{1}{1 + k_\alpha(T) \cdot \frac{c_{\text{H}_2}}{c_{\text{CO}}}} \tag{6.8}$$

$$\begin{aligned} \gamma &= \frac{rate_{methane}}{rate_{propagate} + rate_{terminate} + rate_{methane}} \\ &= \frac{k_m(T) \cdot c_{H_2}}{k_p(T) \cdot c_{CO} + k_t(T) \cdot c_{H_2} + k_m(T) \cdot c_{H_2}} \end{aligned} \tag{6.9}$$

However, further simplification is possible considering the low value for the conventional termination rate. For chain growth possibilities of about 0.9 and an additional termination probability for methane of 0.5, which lead to a still moderate methane selectivity of 10%, the additional termination rate for methane is ten-fold larger than the conventional termination rate. Therefore, the function for the additional methane termination probability transforms to almost resemble the function for the chain growth, only with an inverted concentration ratio (equation 6.10).

$$\begin{aligned} \gamma &= \frac{k_m(T) \cdot c_{H_2}}{k_p(T) \cdot c_{CO} + k_t(T) \cdot c_{H_2} + k_m(T) \cdot c_{H_2}}, \qquad k_t \ll k_{\text{m}} \\ &\approx \frac{k_m(T) \cdot c_{H_2}}{k_p(T) \cdot c_{CO} + k_m(T) \cdot c_{H_2}} = \frac{1}{1 + k_\gamma(T) \cdot \frac{c_{CO}}{c_{H_2}}} \end{aligned} \tag{6.10}$$

Not shown in the previous equation is the exponent in the concentration to allow for a certain reaction order to be applied. This exponent, δ, is in the end just an additional parameter to improve the accuracy of the selectivity estimation analogue to the exponent for the chain growth probability, so that the final equation 6.11 yields to:

$$\gamma = \frac{1}{1 + \left(\frac{c_{\text{CO}}}{c_{\text{H}_2}}\right)^{\delta} \cdot k_\gamma \cdot \left(\frac{\Delta E_{\text{A},\gamma}}{R}\left(\frac{1}{T_{\text{ref}}} - \frac{1}{T}\right)\right)} \tag{6.11}$$

In total, three new parameters are introduced, the exponent, δ, the activation energy, $\Delta E_{\text{A},\gamma}$ and the selectivity coefficient, k_γ. Yet, the enhanced termination probability for methane, γ, is not a parameter anymore. Hence, only two additional parameters are added to the model, which also need to be estimated. But as they are based on a rational derivation rather than just empirical testing, it is assumed to be an improvement to the model. Eventually, only the results of the parameter estimation will allow for an evaluation of their validity.

6.1.3 Estimation results

Both previous paragraphs altered either the model or the experimental data and introduce new assumptions that need to be checked against the quality of the fitting to justify their use and benefit to the model accuracy and predictability. In order to test the benefit that taking deactivation into account and introducing a modified selectivity model provide, the parameter estimation was conducted for different scenarios. In these scenarios the correction for deactivation was either included or not and the selectivity model was either kept without any modification for the methane selectivity, assigning a value of zero to the new parameter, γ, or it was kept at a constant value or, as the last case, γ was assigned to a function of temperature and reactant concentration. This leads to a total of six combinations for which the estimation results are shown in the form of parity plots in figure 6.4. In the top left corner, the base case without any modification to the activity or the selectivity model is shown. It reveals a substantial scattering of the conversion, the C_{5+} selectivity does scatter a bit less, but is clearly offset to the experimental values. Only the methane selectivity is relatively well matched by the simulation. When adjustment of the activity is applied the scattering of the conversion becomes much lower, but the selectivities behave almost identical to the base case, with still a clear deviation for the C_{5+} selectivity. This improves already when the modification to the selectivity model allows for an increased methane selectivity, even when no deactivation correction is applied. But when activity factors are additionally taken into account, the scattering of CO conversion improves again clearly. With the most sophisticated selectivity model, the tendency is very similar, just for the C_{5+} selectivity, a small but significant improvement can be observed. With an estimated simple constant value for γ, the C_{5+} selectivity exhibits a certain bias, where high experimental values tend to be over-predicted by the model and low experimental values are underestimated. This holds with or without accounting for deactivation. With the improved selectivity model, this bias can be avoided and the best prediction for the selectivity is obtained when deactivation is not accounted for. When deactivation is included the scattering for the C_{5+} selectivity gets slightly worse.

Because these plots only allow for a qualitative comparison of fitting results a more quantitative measure, the cumulated absolute relative residual, for all cases and conversion as well as methane and C_{5+} selectivity is plotted in figure 6.5.

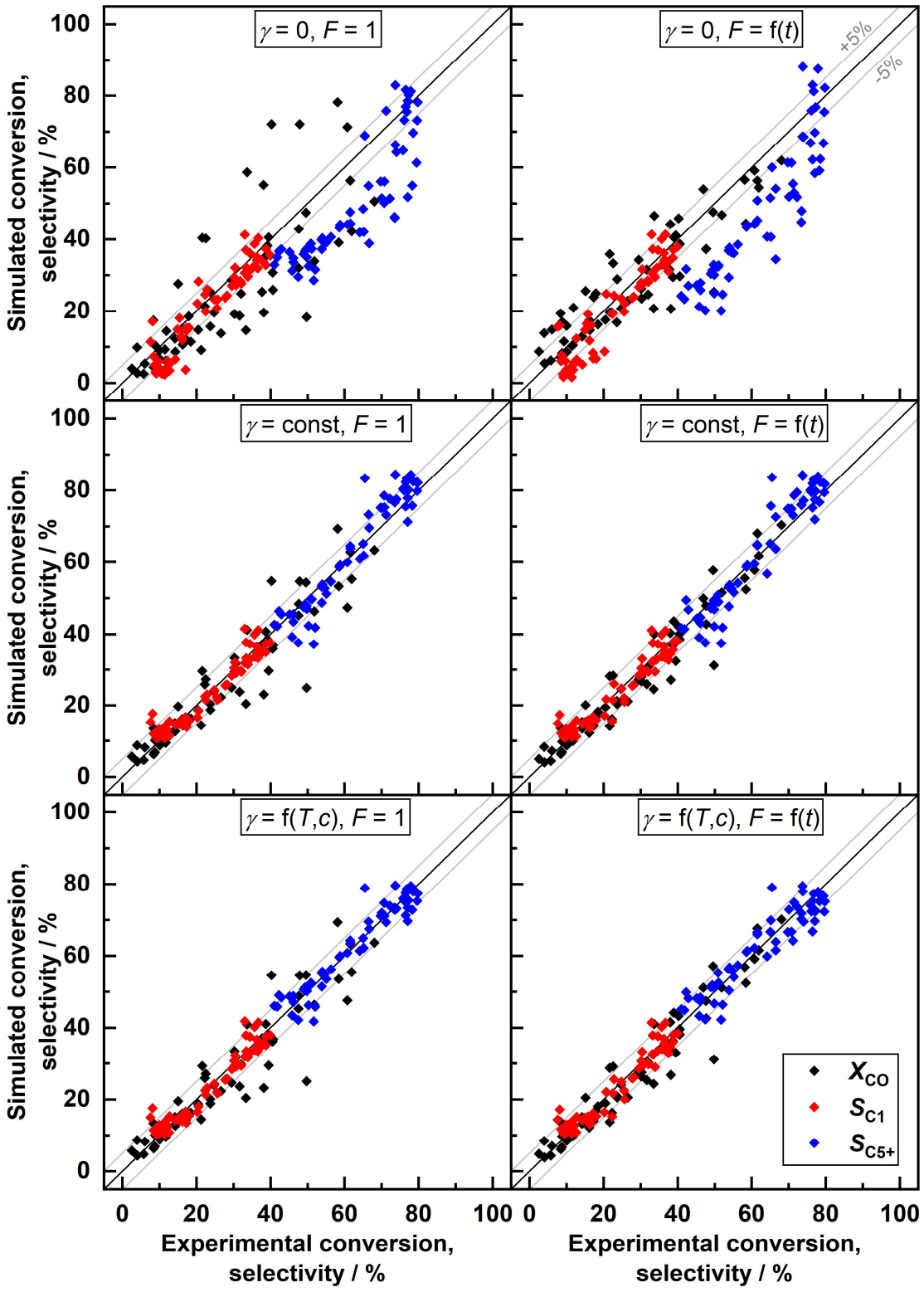

Figure 6.4: Parity plots of parameter estimation results for different model assumptions, including the selectivity model and catalyst deactivation. Absolute 5% error lines are added as an additional reference for the eye.

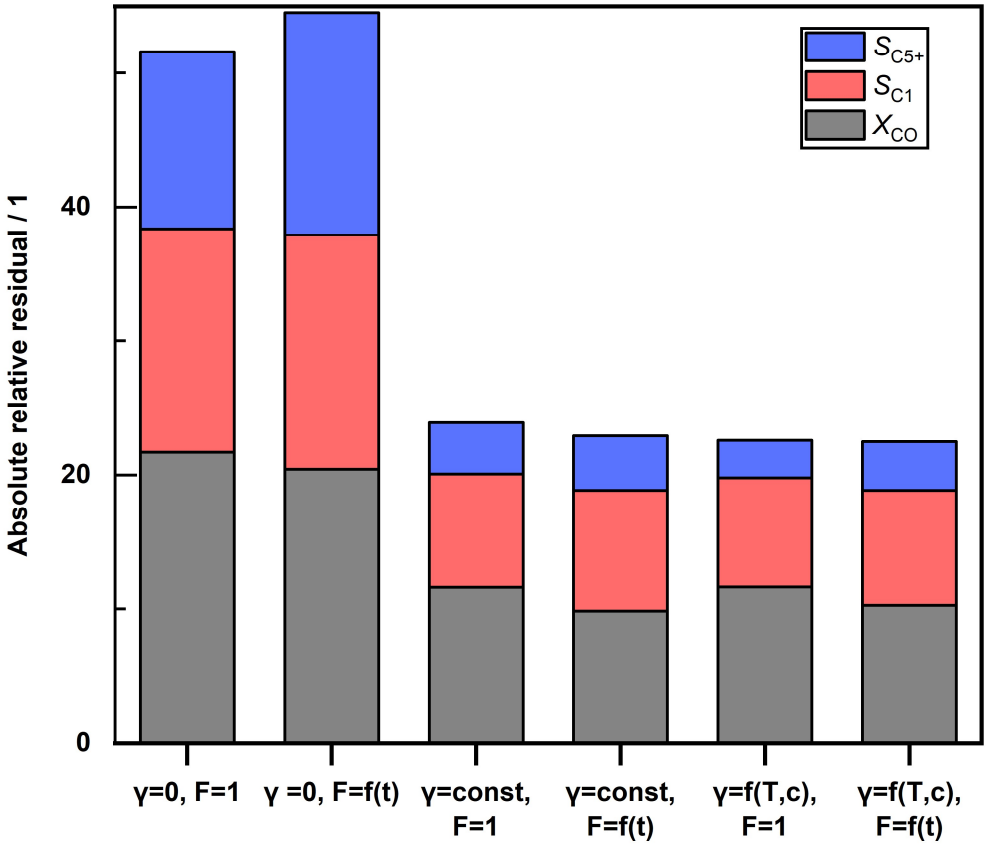

Figure 6.5: Errors of the parameter estimations calculated as absolute relative residual for different model assumptions.

It becomes obvious that the selectivity model needs to include an additional parameter for methane selectivity, as all cases, where γ is none zero, result in less than half the cumulated residual than when γ is zero. The inclusion of the deactivation is, however, less obvious in this illustration. Though conversion clearly benefits from taking deactivation into account, it is generally not beneficial for the accuracy of the selectivities. Without an additional parameter for the methane selectivity, this worsened selectivity even outweighs the benefit in conversion leading to the total residual being higher than without any correction.

For both improved selectivity models the total gain from the improved accuracy for the conversion, when activity factors are considered, is also reduced by the poorer description of the selectivities, but the overall error is still lower than without activity correction. This behaviour where the selectivity description gets worse when deactivation is taken into account might be explained by the fact that not only the reactivity gets hampered when the catalyst degrades but also the intrinsic selectivity of the catalyst can be affected. Additionally, the deactivation is also a spatially distributed reaction with different parts

of the catalyst losing activity more or less rapidly. Also, each part of the catalyst in the reactor does not contribute equally to the conversion measured at the end. Hence, a single factor is only a simplified surrogate in lack of more precise information. Nonetheless, the overall best result is obtained with the full selectivity model and a time-dependent activity factored in.

Further validation of the estimation results is based on the plausibility of the estimated parameters. Figure 6.6 compares the estimated kinetic parameters of the six cases, as just discussed, against the values based on the original work of Yates & Satterfield [12]. The activation energy of the main kinetic coefficient is several times higher than the literature value and is with values from about 150 to 250 kJ/mol within a range that is at the very top of what is normally expected. The value for the activation energy is also much higher than expected from the literature, but with an opposite sign. This inverses the effect that temperature has on the reaction, with high temperatures leading to higher sorption factors and thus generally increasing the inhibiting influence of CO on the reaction. This also allows for fairly high activation energies for the kinetic coefficient, without obtaining too high values for the reaction rate as the temperature rises. The spread of the estimation results for all cases is fairly limited, apart from for the second one, where considerably lower values for both activation energies were estimated. This could be related to the experimental test program. The testing with an ever-increasing temperature over the course of the experiment may lead to a bias in the data because the most deactivated catalysts will always appear together with the highest temperatures. This was thought to be compensated for by the adoption of activity factors, and it does. But apparently, only for the simple selectivity model, where the overall fit is relatively poor, activation energies that are low enough to be considered typical are obtainable. The estimated kinetic coefficient is in the same order of magnitude as the reference value from literature. For the different cases, one can see that by including activity factors, higher kinetic coefficients are achieved. Also, for the most precise selectivity models, higher values for the kinetic coefficients are found suggesting that the catalysts investigated here are several times more active than the one from literature. The sorption coefficients show a similar trend as the kinetic coefficients, but are overall quite similar to the reference value, leaving little room for doubt.

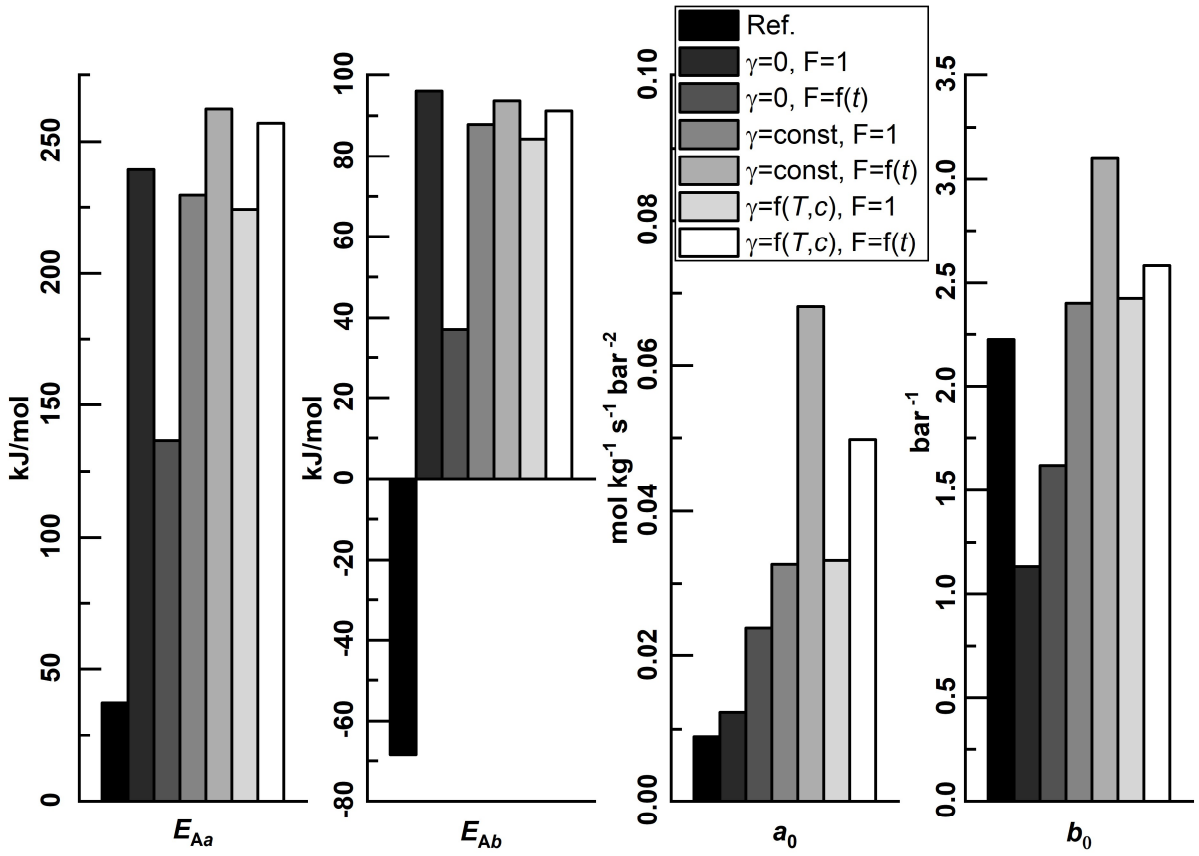

Figure 6.6: Results of the estimation of kinetic parameters for the CO consumption reaction.

Overall the predicted kinetic parameters can be considered reasonable, though somewhat different to the literature values. This is acceptable as this estimation of kinetic parameters can only provide an effective kinetic expression but does not convincingly hint at the intrinsic kinetics. Anyhow, intrinsic kinetic expressions never were the intended aim of this research, since the focus is on the transport effects, which is reflected by the design of the experiments and therefore limits the possible insights into the actual kinetic relations. Nevertheless, the model does work well as a rigorously derived representation of the catalyst behaviour.

In figure 6.7, the results of the parameters for the chain-growth-model are depicted. The obtained values for the activation energy of the expression is found to be several times lower than presented in the literature, indicating a much lower impact of temperature changes on the α-value. A clear trend or pattern for the different cases is however not visible, only for the base case an activation energy of almost zero was found, that would rule out any effects of temperature. It is interesting to see that the alternative value

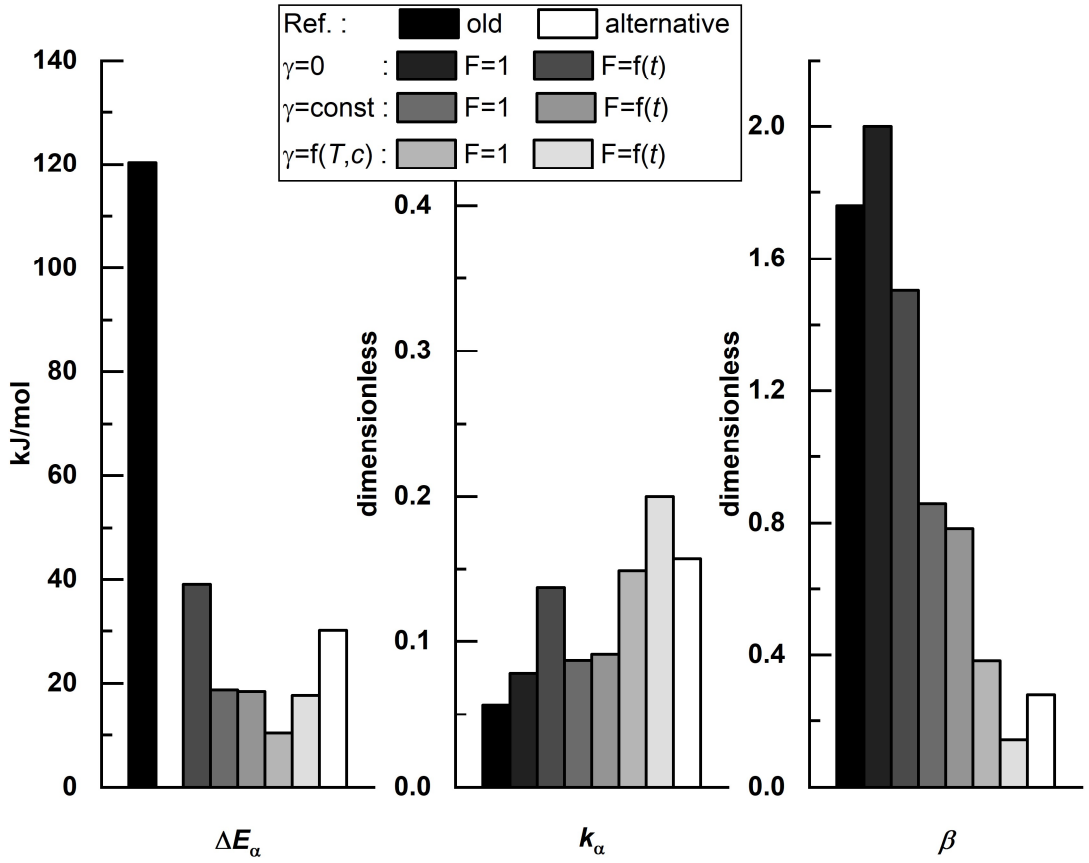

Figure 6.7: Results of the estimation of selectivity parameters for the variable chain-growth probability model.

from the literature, which was published in the same article as an additional set of parameters that was based on secondary data [10], is relatively close to the predictions of this work. This holds even more so for the two other parameters, the selectivity coefficient and the exponent. The coefficient for the selectivity model is for the base case quite close to the primary parameter from literature only slightly higher. With more corrections for the selectivity or activity, this parameter tends to increase and is eventually, for the best scenario, again only slightly higher than the secondary parameter from literature. An opposite trend can be seen for the exponent of the concentration ratio of H_2/CO. Here the primary exponent is fairly high, as is the parameter for the base case, but with more corrections, this parameter drops and is finally very close to the secondary parameter in literature. Hence all estimations for these selectivity parameters appear to be valid and choosing the ones from the last case, which achieved the best description of the experimental values is most reasonable. The fact that the parameters for the exponent and the activation energy are fairly low allows concluding that the model and thereby the catalyst is less sensitive to changes in the concentration

ratio and also less susceptible to be influenced by changes in temperature than initially expected from the literature.

Finally, the tortuosity of the pores inside the catalyst and the tortuosity of the transport pores are checked for being within a physically sensible range. These tortuosities are used to account for effects of the real structures on the effective diffusivity of the reactants inside the pores of the catalyst layer. These effects can either be caused by the geometric hindrance, which is just a descriptor for the prolonged diffusion path inside the pores or due to steric hindrances of the solute molecule, which might be so large to being slowed down by interaction with the pore wall. Most of the results for the catalyst tortuosity (figure 6.8) indicate a value of just below three, which is the reference value that was assumed as a typical value for the calculations discussed in previous chapters. Only the first and the second estimation cases deviate from this with the first one exhibiting a surprisingly high value of 7.5 and the second one exceeding three, but only by a small margin. This substantial difference is clearly caused by deactivation being incorporated in the model or not. When, as for the first case, deactivation is not accounted for, all measurement points at higher temperatures, which occurred at later times and therefore are more affected by deactivation, are also deviating more from the expected conversion of the model. Hence the tortuosity is drastically increased to overly emphasize mass transport limitations that can reduce this flaw in the model interpretation of the data to some extent. With deactivation taken into account, this error is reduced and much more realistic values for the tortuosity are obtained. However, the same can be said about the cases where only the selectivity model is improved but activity factors are assumed to be constant at unity. So just looking at these values does not allow further differentiation between the estimation cases.

The results for the transport pore tortuosity are relatively similar to the tortuosities obtained for the catalyst, but they differ in some important points. The first thing is the overall fairly high value for the transport pores, which is exceeding three for the first two cases and exhibits numbers below three for the last for cases. Therefore the intended benefit of transport pores is considerably reduced - reference calculations were based around a value of one. Another notable finding is that the tortuosity for the second case, where deactivation is incorporated with no advanced selectivity model, is with a value of 4.7 substantially higher than the tortuosity of the catalyst. This is highly unlikely as the transport pores with their larger pore width do not constrict the diffusive flux of the reactants as much as the pores within the catalyst. Thus, this is yet another reason for the inclusion of an advanced selectivity model. For these cases, where additional methane formation is assumed, the transport pores and the catalyst exhibit very comparable

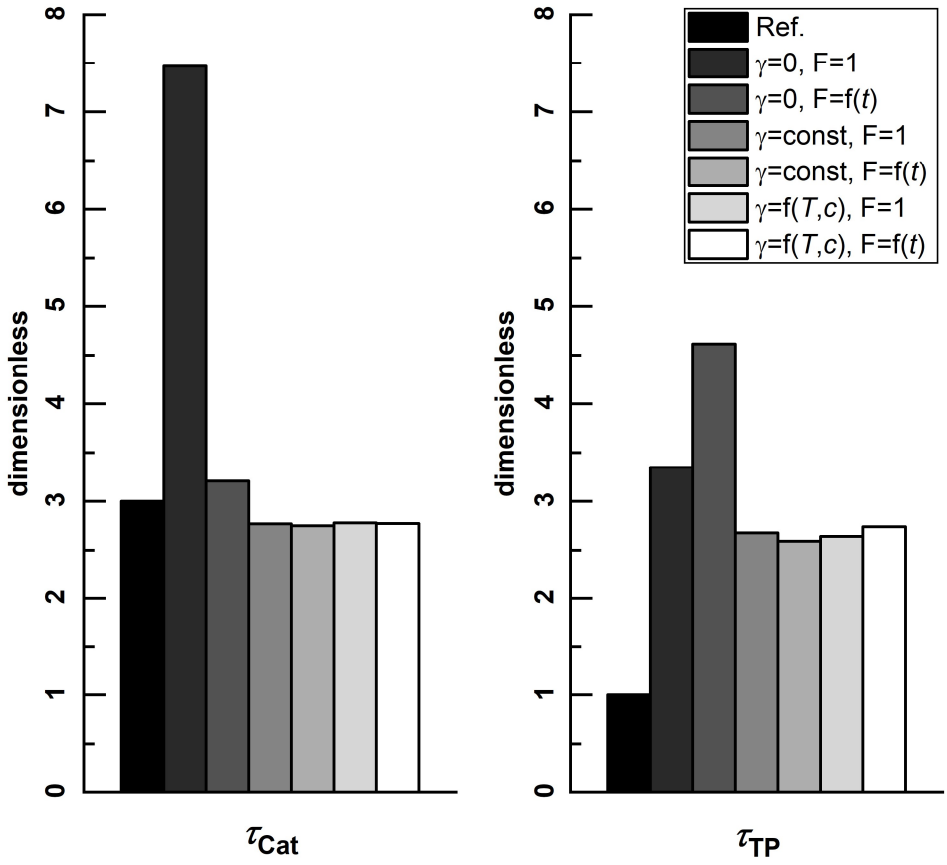

Figure 6.8: Results of the estimation the tortuosities as the main factors for the description of effective mass transport within the catalyst.

tortuosities, with the former averaging around 2.7 and the latter being at a value of about 2.6. These values are a bit high given the void fractions of about 50% within the catalyst and around 30% for the transport pores. Analytical and Numerical simulations for theoretically derived pore geometries often find only fairly low values, between 1.3 and 1.6, when agglomerates of spherical particles are considered [13–19]. Due to the method of generating the porous structure, the resulting pores often have very rounded curves leading to smooth transitions in the direction of the pores. Only when a geometry with orthogonal pore arrangements is investigated the analytically predicted values for the tortuosity increased noticeably. Beeckman found for a network of such orthogonally connected pores an analytical solution that predicts a tortuosity in the range of 2.4 to 2.7 for given porosities from 0.3 to 0.5 [20]. However, despite an apparently good agreement to the values estimated in this work, pores of this type are not as easily proven to exist than agglomerates of spheres, which are easier established as a relatively likely system to be found in nature or to be synthesized. This is also the case for the catalyst layers investigated in this work. Especially the transport pores are very likely

to have been formed as the result of the agglomeration of spheres. The catalyst particles are almost spherical and bound together during the fabrication of the catalyst layer. Hence the high value for the tortuosity needs further verification. This also holds for the mesopores within the catalyst, though for these the geometry is not known at all.

There are several possible causes for the high values, except for the pore geometry. For the transport pores, the high tortuosities could be explained by additional transport resistances. But this can be ruled out, because the transport pores are with about 10 µm in width sufficiently small, as was shown in chapter 3, based on literature approximations, and also confirmed by simulations on 3D geometries [21]. Another reason could be the restriction of diffusive flow when the pore size is small enough to interact with the solute. But for this to be of influence, the transport pores are magnitudes too large and only the catalyst pores could be affected. For the estimation of the bulk diffusion coefficient of CO its molecular diameter was assigned a value of 0.372 nm [22] while the pore width has its maximum at 6 nm. With this data and by using various empirical or analytically derived equations [23–26] the effective diffusion should be reduced by only 10 to 15%. For the other reactant, hydrogen, with its smaller diameter, the impact should be even less. Thus, restricted diffusion cannot be identified as the main cause leading to the high numbers for the tortuosities, albeit undoubtedly contributing to a higher tortuosity. This only leaves an erroneous molecular diffusion coefficient as one last possible explanation. This could be the case when the composition of hydrocarbons that are present in the pores leads to an average carbon number that deviates significantly from the assumed average carbon number of 28. Because octacosane is used as a model component for the prediction of the physical properties of the liquid product – including the diffusion coefficient, the actual molecular diffusion coefficient will be higher if the average carbon number is lower than 28 and lower when the average carbon number is higher. Consequently, the composition of the liquid products in the catalyst pores is important for obtaining the right tortuosities and is discussed in more detail in the last section of this chapter. Here it suffices to say that when the carbon number decreases to 16 the diffusivity increases by less than 35% and for an increase of the carbon number to 48 the drop is even less than 15% [27].

As no singular cause can be attributed to the somewhat high tortuosities, it is likely caused by a combined effect of pore geometry, restricted diffusion and change in product composition and well within a valid range. Only the surprisingly slight difference between transport pores and catalyst pores remains unresolved.

Aside from the already discussed resulting parameters only the ones for the methane selectivity model equation are left, but since they are exclusive to this work and lack

referenceable literature values they are only listed in the appendix (table C1). In conclusion, the parameter estimation resulted in a model with a reasonable set of parameters that yields the best accuracy when deactivation is accounted for by activity factors and the enhanced methane selectivity is modelled analogously to the chain growth probability. For this best-case model, a comparison of experimental and simulated values for conversion as well as methane and C_{5+} selectivity are depicted in figure 6.9. The effect of increasing temperature or layer thickness driving the formation of products from longer to shorter hydrocarbons is well described for all layers and the tendencies are very similar. Also, the actual behaviour of the conversion is very well matched by the simulation results for both types of catalysts and all layer thicknesses. Merely for the highest temperature and layer thicknesses of about 450 µm, a certain discrepancy is visible. Here the simulated reactor performance is poorer, in terms of conversion and selectivity to long-chained products, than in reality. Aside from this minor inaccuracy, the model is generally well suited for describing the behaviour of catalytic layers with and without transport pores.

6.2 Introducing vapour and liquid phase

As mentioned previously, the composition of the liquid hydrocarbons that are formed inside the catalyst during the reaction can have a contributing effect on the precision of the estimation of the transport parameters, as the composition affects the physical properties of the reactants, especially the molecular diffusion. That is why the estimation of the real product composition is shown in this section and compared to the assumptions of the model.

In order to do that, the transport of the products within the pores of the catalyst layer and the axial transport through the reactor channel need to be incorporated in the model. For an appropriate representation of the composition, a high number of hydrocarbons needs to be included. For this estimation, a maximum carbon number of 40 was chosen. This vastly increases the number of equations needing to be solved, making this approach fairly time-consuming. Hence, a simplification for the calculation was required and introduced. The already working reactor model was just used as a basis to provide the local reaction rates for all considered components. In the following step, the product composition is calculated on that basis but without a feedback to the reactor model. This does not reduce the number of equations involved, but the system of equations is separated into two parts that behave much more docile during the calculation of a numerical solution.

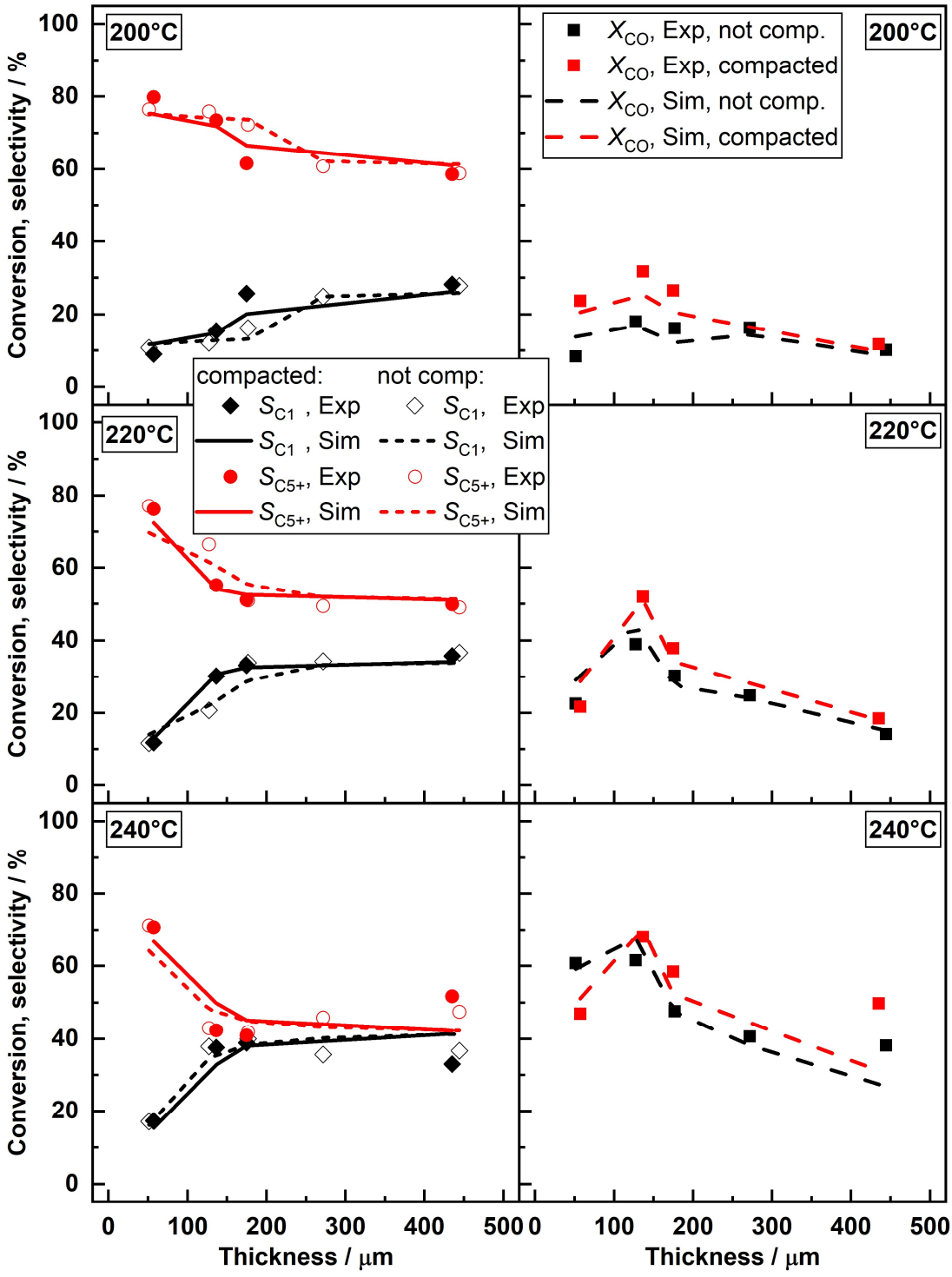

Figure 6.9: Comparison of methane and C_{5+} selectivity based and conversion on experimental results and predictions from parameter estimation for layers of different thickness and different temperatures; GHSV = 5000 h^{-1}, p =21 bar, $H_2/CO = 2$, $CO/Ar = 9$.

6.2.1 Model set-up and equations

In this product composition model, the fluid phase is assumed to be isothermal, isobar and in vapour-liquid equilibrium at each point along the axial direction. There is also no slip between the gas and the liquid flow. Thus, a simple balance (equation 6.12) for each species in the fluid phase can be calculated when boundary conditions (equation 6.13) for the feed are provided.

$$\frac{d\dot{n}_i}{dz} = J_{\mathrm{cl},i} \cdot t_{\mathrm{gas}} \tag{6.12}$$

$$\dot{n}_i(z=0) = \dot{n}_{i,0} \tag{6.13}$$

Only the molar flux from the catalyst to the fluid phase needs further specification as it depends on the effective production rate of every species within the catalyst. Here that is included via the diffusive and convective flux out of the catalyst layer surface (equation 6.14). However, for that matter, the profiles of liquid concentration and velocity within the catalyst pores are required and are accessible when the classic reaction-diffusion equation is extended with a term for convective transport (equation 6.15). This includes the velocity that is simply derived from a non-divergence-free continuity equation, with the reaction as a source term (equation 6.16).

$$J_{\mathrm{cl},i} = \left((1-\varepsilon_{\mathrm{TP}}) \frac{\varepsilon_{\mathrm{cat}}}{\tau_{\mathrm{cat}}} + \frac{\varepsilon_{\mathrm{TP}}}{\tau_{\mathrm{TP}}} \right) \left(D_i \frac{dc_i}{dy} - u_{\mathrm{l}} \cdot c_i \right) \tag{6.14}$$

$$0 = \left((1-\varepsilon_{\mathrm{TP}}) \frac{\varepsilon_{\mathrm{cat}}}{\tau_{\mathrm{cat}}} + \frac{\varepsilon_{\mathrm{TP}}}{\tau_{\mathrm{TP}}} \right) D_{\mathrm{i}} \left(D_i \frac{d^2 c_i}{dy^2} - \frac{d(u_l \cdot c_i)}{dy} \right) + r \cdot \nu_i \tag{6.15}$$

$$0 = \left((1-\varepsilon_{\mathrm{TP}}) \frac{\varepsilon_{\mathrm{cat}}}{\tau_{\mathrm{cat}}} + \frac{\varepsilon_{\mathrm{TP}}}{\tau_{\mathrm{TP}}} \right) \left(\frac{d(u_{\mathrm{l}} - u_{\mathrm{dif}})}{dy} \right) - r \cdot \frac{v_{\mathrm{C_{28}H_{58}}}}{28} \tag{6.16}$$

A simplifying assumption is that only hydrocarbons generate a volume proportional to their carbon number, which is approximated by the molar volume relative to octacosane. On the other hand, a complication occurs, due to the simultaneous convection and diffusion which demands a correction for the liquid velocity. Without this correction the combined transport effects would over-estimate the flux, leading to inconsistencies with the actual production rate of each species. For this correction, the diffusive contribution to transport for each species, weighted by a carbon number based molar volume, is accumulated over all hydrocarbons to yield a "liquid velocity due to diffusion", u_{dif} (equation 6.17).

$$u_{\mathrm{dif}} = \sum_{i=1}^{40} \left(-D_i \frac{dc_i}{dy} \right) \cdot n_{\mathrm{c},i} \frac{v_{\mathrm{C_{28}H_{58}}}}{28} \tag{6.17}$$

With this, only two boundary conditions for diffusion and one for convection within the catalyst need further specification. At the wall boundary, there are no flow conditions keeping the gradient of concentration and the liquid velocity at zero (equation 6.18 and 6.19). The liquid composition of the vapour-liquid equilibrium applies the concentration that defines the other boundary condition at the interface to the fluid phases (equation 6.20).

$$0 = u_{\mathrm{l}} \tag{6.18}$$

$$0 = \frac{dc_i}{dy} \tag{6.19}$$

$$c_i(y = 0) = \frac{x_{\mathrm{l},i} \cdot p}{H_i \cdot v_{\mathrm{C_{28}H_{58}}}} \tag{6.20}$$

The vapour-liquid equilibrium is calculated by solving the Rachford-Rice equation [28] for a given composition, defined by the molar flows, and results in the molar fraction of the feed that is vaporised, Z:

$$0 = \sum_i \frac{\frac{\dot{n}_i}{\sum \dot{n}_i} \cdot (K_i - 1)}{1 + Z(K_i - 1)} \tag{6.21}$$

With that, the molar fractions for each species in the liquid and gas phase, $x_{\mathrm{l},i}$ and $x_{\mathrm{g},i}$, are easily obtained using already available variables (equation 6.22 and 6.23).

$$x_{\mathrm{l},i} = \frac{\frac{\dot{n}_i}{\sum \dot{n}_i}}{1 + Z(K_i - 1)} \tag{6.22}$$

$$x_{\mathrm{g},i} = x_{\mathrm{l},i} \cdot K_i \tag{6.23}$$

Physical properties for this method are all based on the same data source as for chapters 3 and 5. This also means that octacosane is still used as the reference component upon which the estimation of the physical properties is based. For the equilibrium calculation Henry coefficients for "permanent" gases as CO, H_2, H_2O, CH_4, C_2H_6 were used (equation 6.24), whereas for all longer hydrocarbons their vaporisation pressures were used to calculate the equilibrium constants (equation 6.25) [29]. Only for Argon, an arbitrarily

high value for the equilibrium constant, K_{Ar}, of 1000 was assigned to keep it nearly exclusively in the gas phase.

$$K_i = \frac{H_i}{p} \tag{6.24}$$

$$K_i = \frac{p_{vap,i}}{p} \tag{6.25}$$

Diffusion coefficients for the hydrocarbons and water were analogously estimated to the ones for CO and H_2 [22]. Water was not supposed to form a second liquid phase as it dissolves relatively well in hydrocarbons when the temperature is elevated and the hydrocarbon chain length increases [30] and recent data suggests solubilities of up to 40% for octacosane under conditions relevant for FTS [31].

6.2.2 VLE model compared to reactor model

Before conclusions from the new model, regarding the composition of the hydrocarbons inside the catalyst pores, can be validly drawn the comparability to the reactor model is evaluated by comparing the predicted gas-phase composition of both models. For typical conditions, in figure 6.10, the predicted gas-phase concentrations along the axial direction for the two reactants, water, argon and the first four hydrocarbons are shown. These are all the components that are assumed to be in the gas phase for the reactor model and all other hydrocarbons are therefore expected in the liquid phase. To also account for differences in the selectivity a very thin layer with no diffusion limitations is compared against a thick layer, where diffusion limitations are prevalent. Although one can see for all curves that the new model consistently produces lower concentrations, the difference is only minor. Even at the end of the reactor channel, the relative difference for water or methane is less than 4% and 3%, respectively. For the other components, the difference is even lower. The reason for the VLE model consistently producing lower values can be attributed to the presence of a liquid phase that dissolves part of the gas phase species but also can be a result of additional products being present in the gas phase that the reactor model does not account for.

There is also not much difference between the two types of layers visible, indicating a constant, small error regardless of layer type. Therefore, the assumptions for the reactor model apparently have been sufficient for an accurate description of the system. But the good agreement also means that the VLE model, with the additional diffusion and

convection terms, which rely on data from the reactor model, can be used in a post-processing step without suffering tremendous inaccuracies.

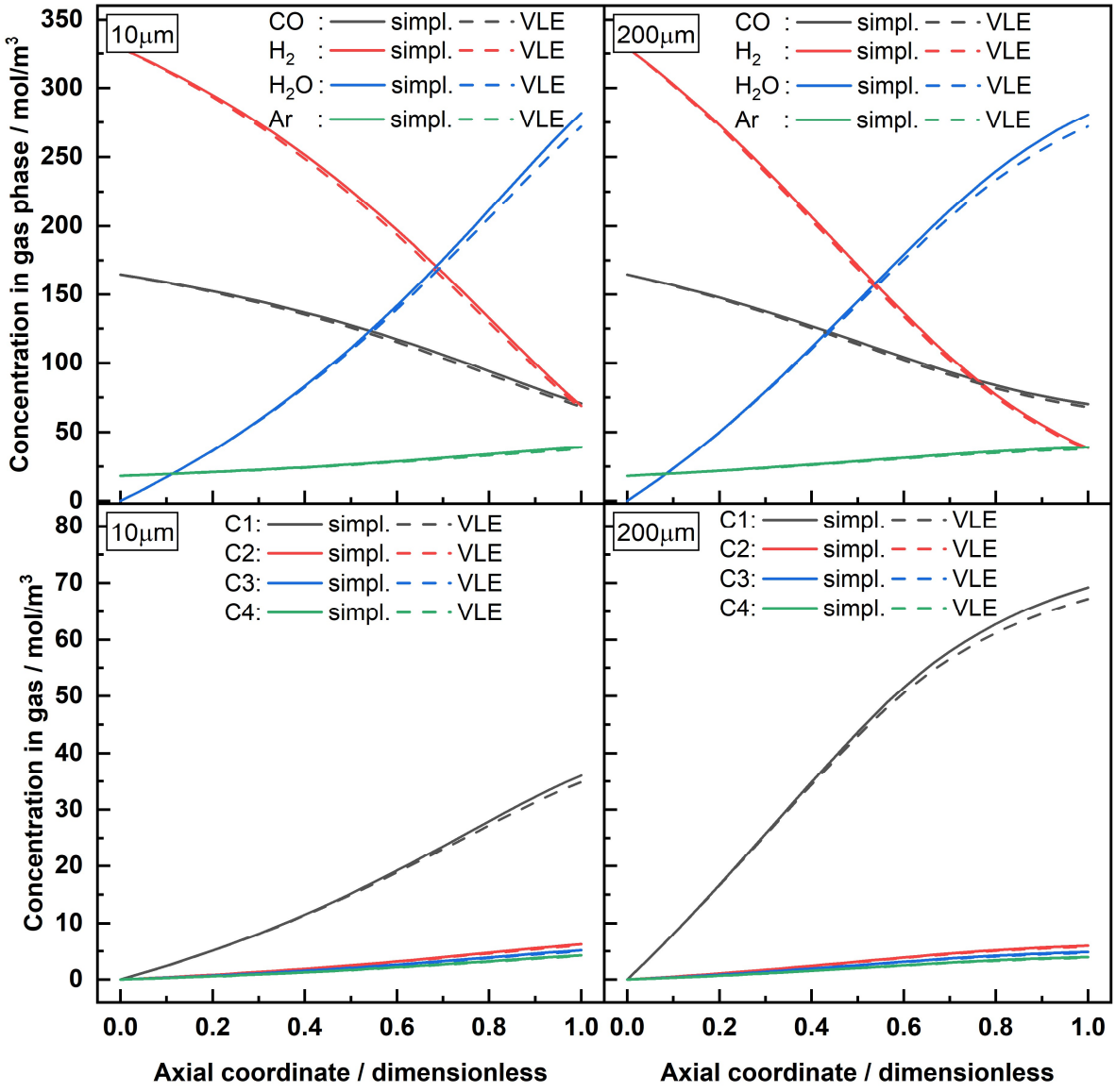

Figure 6.10: Comparison of the predicted gas-phase composition of the VLE and the reactor model for a 10 µm thick catalyst layer (left column) and a thick layer with 200 µm in thickness (right column); in the top row results for both reactants together with water and argon are shown, in the bottom row results for hydrocarbons from methane to butane. $T = 220\,°C$, $p = 21$ bar, $H_2/CO = 2$, $CO/Ar = 9$, $X_{CO} = 80\%$.

6.2.3 Spatial distribution of hydrocarbons

With the good comparability between both models, the extended VLE model can be used to illustrate how the hydrocarbon products are distributed within the reactor and

the catalyst. Starting with the gas phase composition for a layer with negligible diffusion limitations, figure 6.11 depicts the gas and the liquid phase molar fractions for the reactants, argon and the products lumped together in groups of light, medium and high carbon numbers. The gas-phase looks familiar, with respect to figure 6.10, and only a small additional fraction of paraffins from pentane to tetradecane takes up less than 4%. The higher hydrocarbons are not even visible, as only a tiny fraction of them is vaporises into the gas phase. Hence, for the gas phase, this group forms the majority in the liquid phase with only the medium carbon number group and water also contributing to meaningful extents. The reactants, argon and the light hydrocarbons exhibit only a total molar fraction of less than 5%. However, this does not hold for the very inlet of the reactor because here the boundary conditions define the composition. This means that exclusively H_2, CO and Ar are present at this point. This is a simplification of the idealized reactor model. In reality, axial dispersion in the fluid channel, axial diffusion in the catalyst and spreading of the liquid phase would increase the concentration of products at this point flattening the profile. Nonetheless, the catalyst at the inlet is still completely filled with liquid.

The same plots for a layer of 200 µm in thickness are depicted in figure 6.12. Due to the severe diffusion limitations, the selectivity is shifted towards the short-chained hydrocarbons and especially methane. The shift in the selectivity also increases the hydrogen consumption. These effects can be clearly seen in figure 6.12 for the gas phase, but for the liquid-phase, the changes in the absolute values are minute and only changes in the shape of the profile are obvious. Additionally, it is noteworthy to see the water fraction in the liquid phase for both cases with a maximum of just about 20%. This suggests that water is indeed dissolved and does not form a second phase as this would require higher molar fractions.

The previously mentioned figures made clear that the liquid phase is mainly composed of long-chained hydrocarbons, but the illustration of the exact composition requires detailed plots. Thus, figure 6.13 exhibits the molar fraction in the gas and the liquid phase for all hydrocarbons included in the model. The concentration for inlet, middle and outlet are shown to depict the evolution along the axial direction. In order to get a meaningful composition for the inlet position, other than the feed composition, the first mesh point after the inlet is used. The gas phase behaves as expected with molar fractions that increase from the inlet over the middle to the outlet and only differ from zero up to a carbon number of 15. Comparison of the thick to the thin layer also shows the presence of diffusion limitations for the thick layer, as the methane levels in the gas phase are much higher than for the thin one.

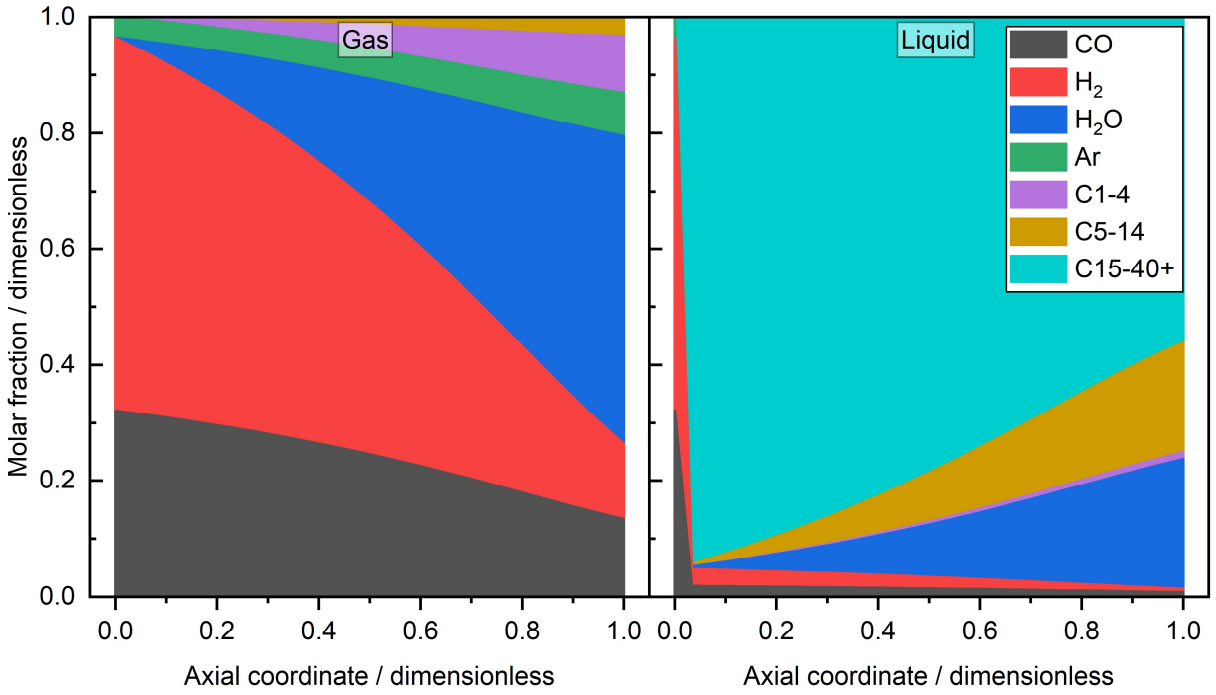

Figure 6.11: Gas and liquid phase composition as a function of the axial position for a 10 µm thick catalyst layer; hydrocarbon products are accumulated in three fractions. $T = 220\,°C$, $p = 21$ bar, $H_2/CO = 2$, $CO/Ar = 9$, $X_{CO} = 80\%$.

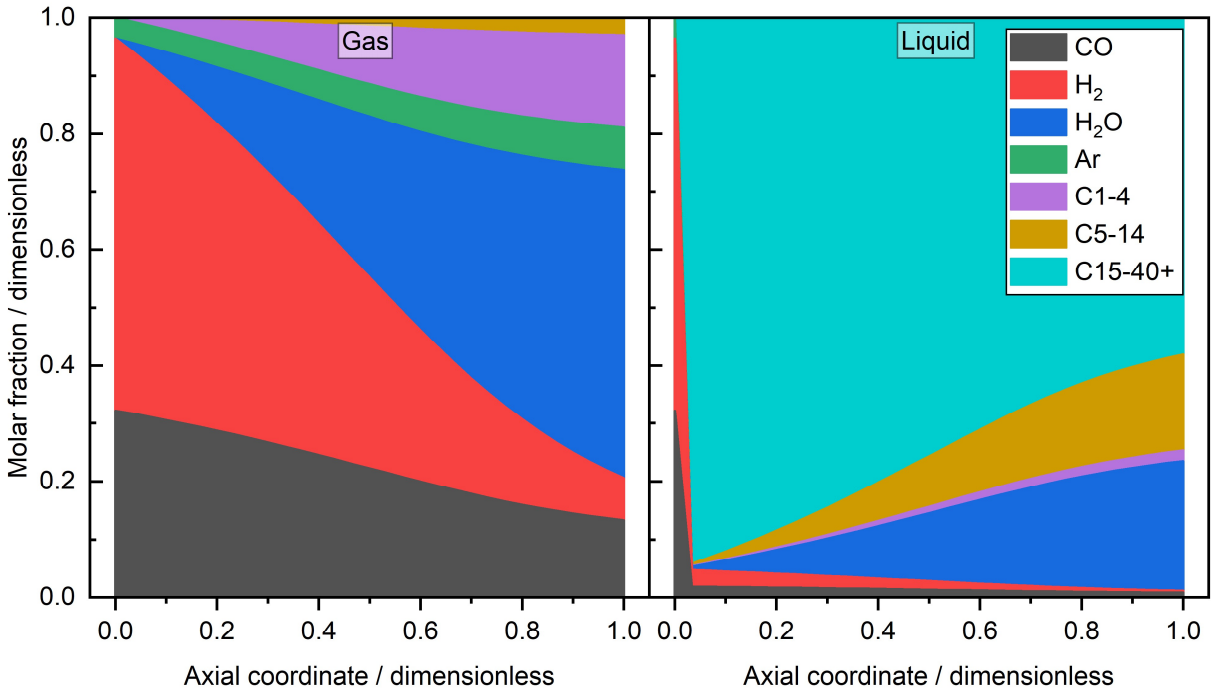

Figure 6.12: Gas and liquid phase composition as a function of the axial position for a catalyst layer with a thickness of 200 µm; hydrocarbon products are accumulated in three fractions. $T = 220\,°C$, $p = 21$ bar, $H_2/CO = 2$, $CO/Ar = 9$, $X_{CO} = 80\%$.

Interestingly this does not exactly project to the liquid phase composition. Despite suffering from diffusion limitations that generally reduce the average α value and thus the catalysts ability to produce long hydrocarbons, at the inlet the maximum of the distribution is at 38 and therefore higher than for the thin layer with a maximum at 36. This surprising difference is also mirrored by the values for tetracontane, which are even higher than the "maximum" as this component represents all higher hydrocarbons to close the carbon balance.

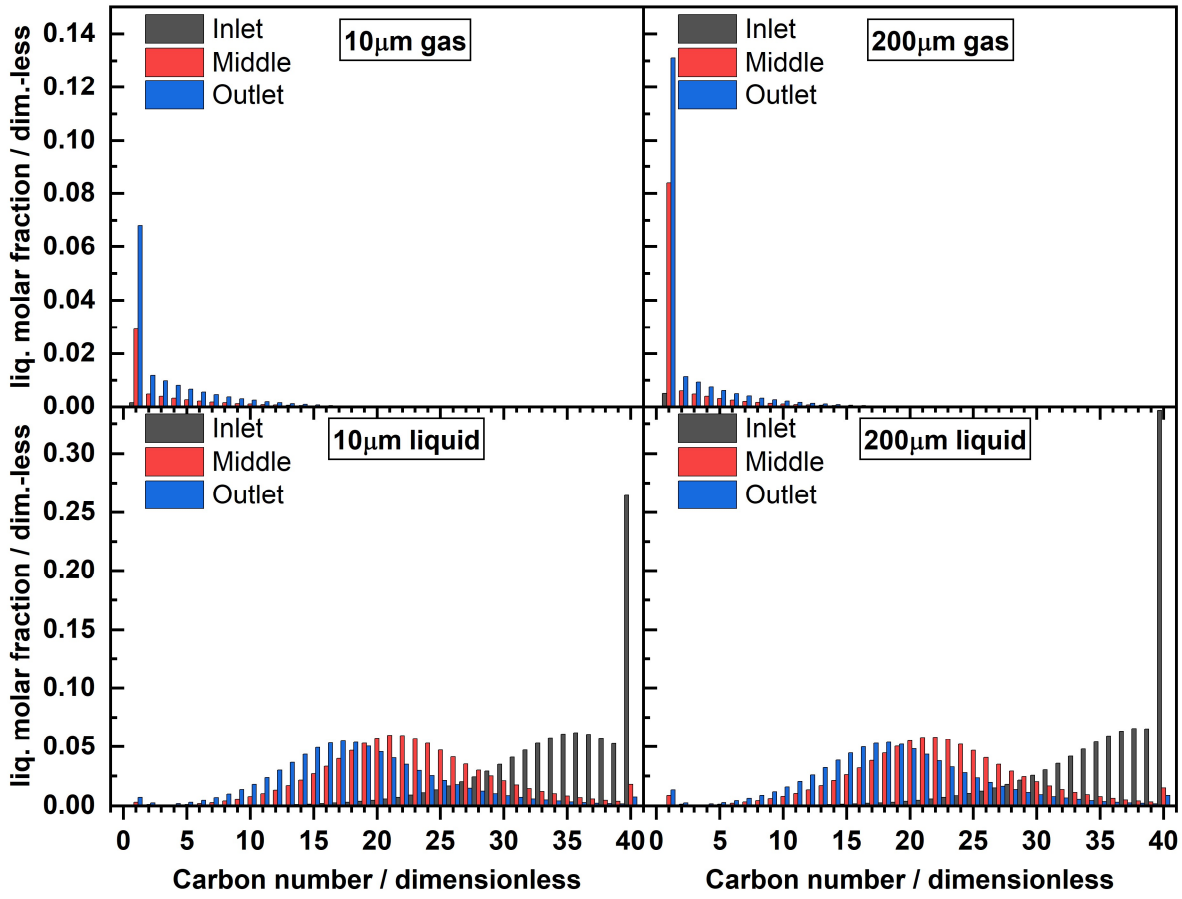

Figure 6.13: Molar fractions of the hydrocarbons in gas (top row) and liquid (bottom row) phase for catalyst layers with a thickness of 10 µm (left column) and 200 µm (right column). $T = 220\,°C$, $p = 21$ bar, $H_2/CO = 2$, $CO/Ar = 9$, $X_{CO} = 80\%$.

Downstream at the middle and outlet, the composition becomes almost identical for both layers with a clear shift towards shorter hydrocarbons. The carbon number with the highest fraction is 22 for the middle and just 17 for the outlet.

This is remarkable as for the given reaction conditions the local H_2/CO ratio shifts to lower numbers with progressing conversion along the fluid stream. The reduced H_2/CO ratio slows down the reaction but also causes a shift of the selectivity towards more products with higher carbon numbers. Despite a relative shift towards more, longer-

chained products, the liquid composition exhibits an opposite trend. An explanation for this apparent paradox can be given when looking at the distribution of products between the gas and the liquid phase. For solving the VLE, the fraction of vaporisation, Z, was introduced, that describes the combined molar fraction all species that are in the gas phase compared to the liquid phase. On the left side of figure 6.14, this fraction of vaporisation is shown, again for a thick and a thin layer. Additionally, a fraction of vaporisation just for the hydrocarbons is depicted as well. Overall, almost the entire molar amount of species is in the gas phase and only from approximately the middle of the reactor a value for the fraction of vaporisation mildly deviating from unity is visible. This is the case for both types of layers, though the 200 µm layer exhibits a slightly higher value than the 10 µm layer, which is in line with its higher methane selectivity. However, when looking at the fraction of vaporisation that only includes hydrocarbons, the deviation gets a bit bigger, but the difference between the two layers also increases. The 10 µm layer with its lower selectivity towards methane produces more long-chained hydrocarbons that have a greater tendency to form a liquid phase. Hence at the outlet, almost 4% of all hydrocarbons are in the liquid phase, whereas this number is less than 2% for the 200 µm catalyst layer. This means that the more products are being produced that tend to form a liquid the lower is the fraction of vaporisation or the higher is the fraction of the liquid. But when more liquid is formed, more, shorter-chained products can also dissolve in this liquid phase and thereby reduce the average carbon number. This can clearly be seen on the right-hand side of figure 6.14, where the average carbon number for the gas and the liquid phase is shown. For the 200 µm layer in the liquid, the initial number is slightly above 35 but for the thin layer, it starts just below 35. Despite this initial difference and the fact that the gas phase for the thick layer exhibits a lower average carbon number, the further evolution is almost identical with a continuous drop to the end at a value of about 19. So, the lower fraction of vaporisation for the thick layer prevents a too extensive dissolution of short-chained hydrocarbons, albeit a larger quantity of shorter-chained products is present in the gas phase.

In other words, the thick layer produces such small amounts of long-chained hydrocarbons, that only the longest can form a liquid phase, which then consists of more, longer-chained hydrocarbons and consequently has a slightly higher average carbon number than the 10 µm layer. And because fewer products remain in the liquid phase, the fraction of vaporisation is higher; hence a lesser amount of short-chained products can be dissolved. In total, this leads to fairly similar profiles for the average carbon number in the liquid phase, regardless of the layer thickness and resulting selectivity.

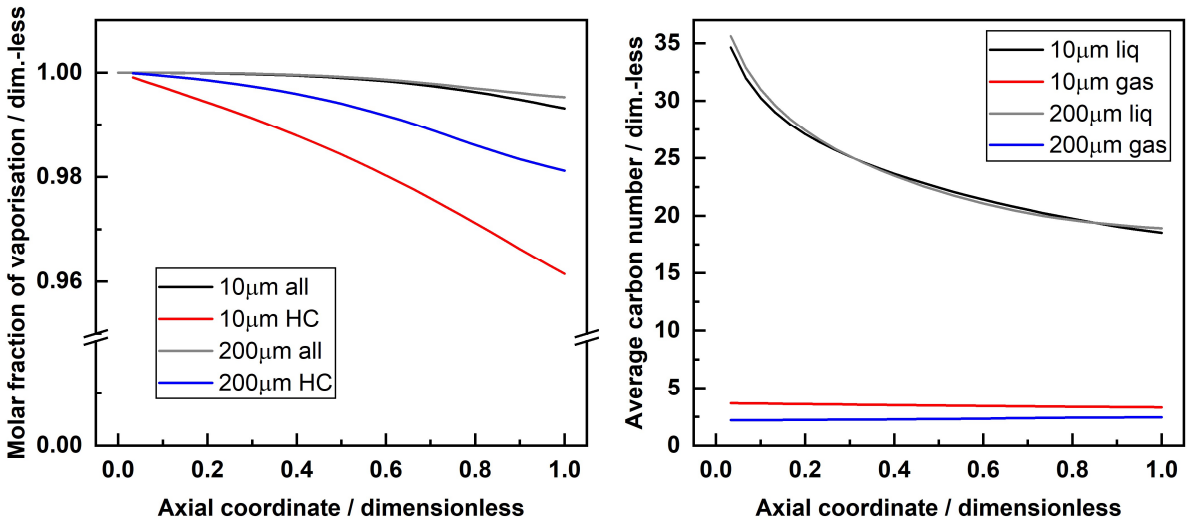

Figure 6.14: Molar fractions of vaporisation on the basis of all species or only including hydrocarbons, HC, (left) and average carbon numbers for the gas and the liquid phase (right) along the axial direction for catalyst layers with a thickness of 10 µm and 200 µm; $T = 220$ °C, $p = 21$ bar, $H_2/CO = 2$, $CO/Ar = 9$, $X_{CO} = 80\%$.

With the composition of the liquid phase in the fluid channel, the composition within the catalyst can then also be calculated. For better clarity, just the average carbon numbers are used, as these are also the numbers that are most interesting for validating the assumption of the reactor model that the products can be represented by a single paraffin with a carbon number of 28. For the two layers, the 2D-distribution of the average carbon number is depicted in figure 6.15. The plots are oriented in a way that the gas flow will occur from left to right, with the fluid-catalyst-boundary at the bottom and the diffusion and pore convection is occurring vertically with the wall-boundary at the top.

As for the average carbon number in the liquid phase, in the fluid channel, there is almost no difference observable between the two types of layers. Surprisingly the effect of diffusion limitations, as expected from the main reaction and the diffusive transport of the reactants, is apparently very minimal even for a layer with a thickness of 200 µm. Only just next to the fluid-catalyst boundary into the catalyst a slight curvature is visible in the plot, indicating a minor and insignificant drop in the carbon number at these points. Thus, overall the average carbon number within the catalyst is very similar to the carbon number of the liquid phase in the fluid channel.

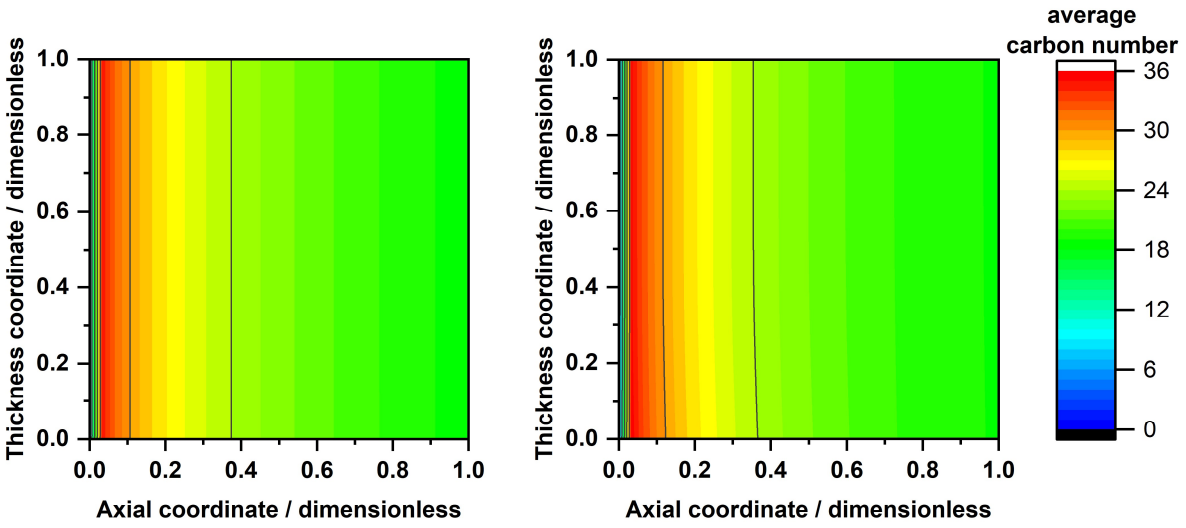

Figure 6.15: 2D plots of the average carbon number within the catalyst layers with thicknesses of 10 µm (left) and 200 µm (right); $T = 220\,°C$, $p = 21$ bar, $H_2/CO = 2$, $CO/Ar = 9$, $X_{CO} = 80\%$.

Finally, this allows evaluating whether the assumption of a constant carbon number of 28 for a representative paraffin is a valid choice or not. Assigning a constant value for the carbon number of a hydrocarbon, upon which all physical properties are based on, is clearly not the best possible choice as the average carbon number will undergo changes just as the catalyst and its performance will. For the investigated reference case, the carbon number does change between 35 and 19 depending on the axial position. So ideally, this change along the axial position would be included in the model. However, for the reference case, a conversion of 80% was used, which is significantly higher than the conversions that were typically achieved with the experiments. Most of the experimental results did not even obtain a conversion of 60% for which the lowest average carbon number would be close to 21. Therefore, for a drop from 35 to 21, a constant value of 28 seems like a reasonable, well-chosen guess exactly in the middle between the two extremes. Of course, the temperature can also be a strong driver for the average carbon number as the vaporisation pressures are greatly affected by temperature. But then again, if a constant value needs to be used a value from the middle of the temperature range ought to be a reasonable guess. And since the full inclusion of the VLE model into the reactor model is numerically too demanding the approach with a constant value was used as the next best option.

The fact that the carbon number of 28 seems well-chosen also further strengthens the plausibility of the tortuosities obtained from the parameter estimation, which is a key result of this work. With this additional certainty about the validity of these results, the last section of this work focuses on a sensitivity analysis of the model.

6.3 Model sensitivity analysis

With merging knowledge from simulation and experimental efforts, the results can be used to predict further how the system would behave under ideal conditions. This opens a route to answer a remaining question of this work and to find out if there is a way that would have shown the beneficial effects of transport pores more clearly. Moreover, the model allows predicting the behaviour of the system under varying operating conditions to see if substantial changes would occur.

6.3.1 Transport pore effect

The catalyst layers used in the experiments exhibited a fixed porosity of transport pores with either none or about 30% porosity. Comparison of these layers showed only very limited benefit in the selectivity, but between a thickness of about 100 µm to 250 µm the selectivity improved when transport pores were used. For the conversion no advantage was obtainable. Especially this absence of any improvement in conversion is indicative for too poorly performing transport pores being used so that only the reduction of active mass had come into play but not the benefit for the improved catalyst efficiency. Only when fewer transport pores are used, there might be a range where also the catalyst efficiency could improve. For a thorough screening, catalyst layers with thicknesses between 10 and 300 µm and incrementally increasing transport pore porosity have been simulated for typical reaction conditions, e.g. a temperature of 220 °C a H_2/CO ratio of 2, a CO/Ar ratio of 9 and a pressure of 21 bar. To include the effect of integral operation the simulation was conducted for a CO conversion of 1% and 80%. The results of this are depicted in figure 6.16. For a conversion of 1%, the efficiency presents the typical profile with a distinct maximum, well above 100% for the layers without transport pores, but as transport pores are introduced they reduce the total active mass more than they improve the mass transport, therefore only a dropping efficiency can be seen. Though, the position of the maximum in efficiency is shifted from its initial position just below 100 µm to higher values. This is at least a mild indication of improvement for the mass transport.

At 80% CO conversion the maximum is much less pronounced and also not exceeding values of 100% anymore. This is because the rate that is used as a reference for the efficiency is the surface rate at inlet conditions. Hence, a loss in efficiency is already purely caused by the dilution of reactants at high conversion even for thin layers without internal mass transport limitations. And the diffusion effect comes on top of that for

thicker layers. However, when using the averaged molar flux of the catalyst layers a slight difference between 80% and 1% conversion can be seen, aside from the obvious difference in absolute height.

At differential operation, the total amount of converted CO increases proportionally to a rise in layer thickness and between 70 to 90 µm the line begins to deviate from a linear correlation positively – as a variable efficiency in excess of 100% would suggest. After the maximum in efficiency is reached only a flat line for the total flux of CO is prevalent. This clearly shows that beyond a certain thickness, any additional catalyst cannot be utilised due to diffusion limitations. With the use of transport pores, this point can be moved to thicker layers, but the total value is only reduced.

However, this translates not entirely to the 80% conversion layers, as for these a slight increase in the total molar flux of CO can still be observed after the initial linear rise, but with a magnitudes lower gradient. For the layers with added transport pores this secondary gradient is also visible, but adding more of the pores also just reduces the obtained total flux of CO. On the other hand transport pores can show quite some benefit for the selectivities. Without transport pores a jump in the selectivity to methane and C_{5+} occurs around 80 µm and with higher values for the transport pore fraction this jump is pushed to higher thicknesses of 300 µm and more for the highest porosities. At 1% conversion the jump involves a change of nearly 20% but for the high conversion the jump only leads to a change of about 10%, always with a rise for methane and a drop for C_{5+} as the thickness increases.

The ATY as the indicator for the performance of a catalyst layer can be written as the multiplication of C_{5+} selectivity and total molar flux of CO. So, when the sudden change in selectivity outweighs the permanent drop in total flux for a certain layer, a positive effect can be observed, but only in a limited thickness range. The improvement is visible for the 1% conversion between 75 µm and 160 µm for which the corresponding transport pore fraction increases from 0 to 40%. At 80% conversion, this thickness range is limited to values from 75 µm to 110 µm and the transport pore fraction only increases up to values of ca. 35%. However, transport pores are merely beneficial when the improvement is based against the same layer thickness, because the highest ATY is still observed for a layer without transport pores, negating a global improvement via utilisation of transport pores. Also, the range where at least a local positive contribution occurs is greatly curtailed. This is in stark contrast to the positive effect that was drawn in previous chapters, but it is a strict consequence of the already comparatively high porosity of the catalyst combined with a very similar tortuosity for both types of pores. This means the effective diffusion within the catalyst is already similarly fast as the

transport within the transport pores. Hence transport pores can only marginally improve diffusive transport but will inevitably reduce the active mass. This is precisely what is shown in figure 6.16.

Additional effects due to integral operation also appear. The improvement potential at high conversion is even further reduced, as a high conversion itself leads to a lower average H_2 to CO ratio within the reactor that improve selectivity at the cost of reaction rate, too. This is a result of the less obvious interplay of selectivity and the associated consumption ratio and feed ratio of H_2 to CO. Within the catalyst the selectivity is getting worse but along the axial direction, the selectivity gets better, as diffusion and convection either promote an increase or a decrease of the local H_2 to CO ratio, respectively. This causes thick layers to benefit more profoundly from a high conversion, as a catalyst that at inlet conditions performs worse than a thin layer, due to diffusion

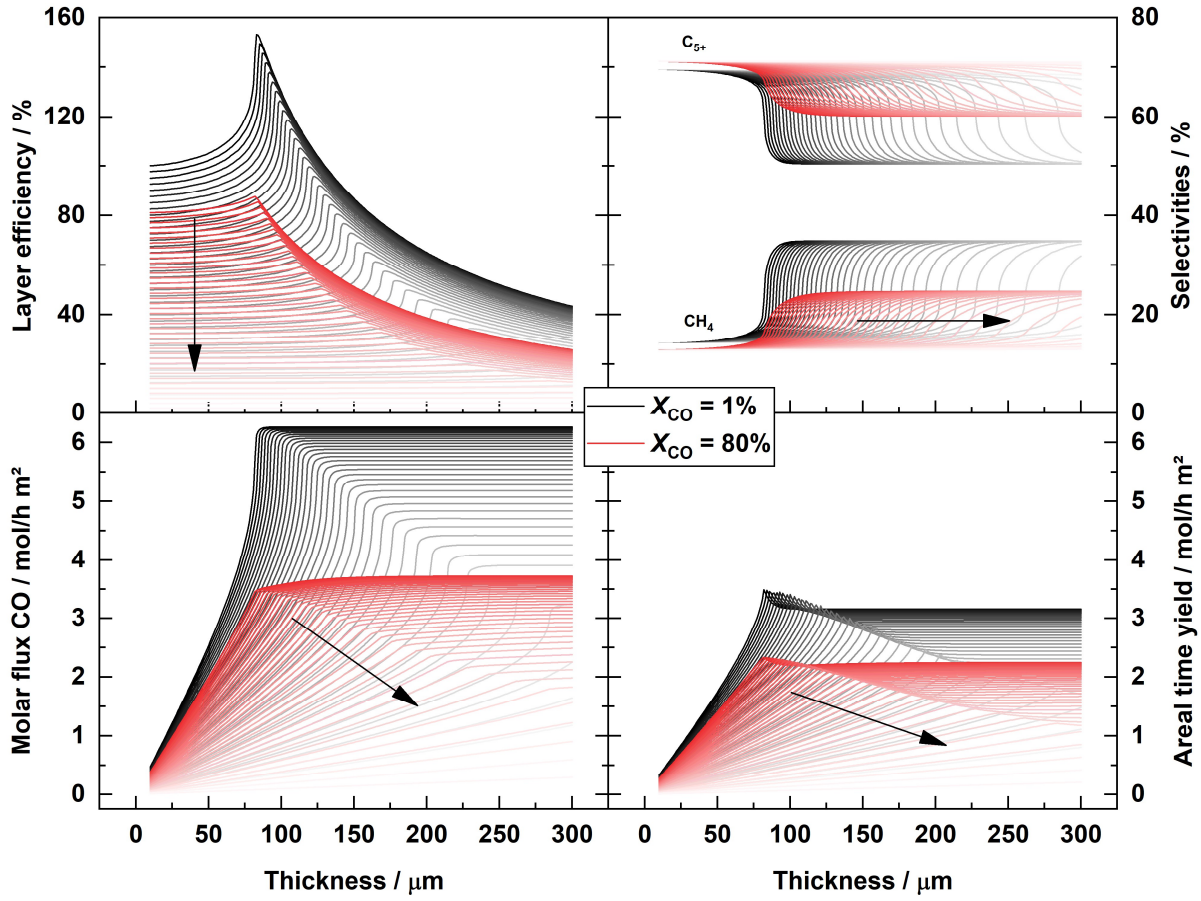

Figure 6.16: Averaged values of catalyst layer efficiency (top left), methane and C_{5+} selectivity (top right), molar flux of CO (bottom left) and areal time yield (bottom right) as function of layer thickness for catalyst layers with transport pore porosities between 0% and 97.5% (increments of 2.5%). $T = 220\,°C$, $p = 21$ bar, $H_2/CO = 2$, $CO/Ar = 9$.

limitations, overly reduces the H_2 to CO ratio for the downstream parts of the reactor. This, in turn, yields higher selectivities for C_{5+} and a lower one for methane, improving the total selectivity of a reactor more when the diffusion limitations are higher. For literature kinetics, this is already shown in more detail in chapter 5 and this positive effect is now confirmed with the kinetic parameter set after fitting of the model. Nevertheless, different from the reference case, the integral ATY does not show an advantage of operating at high conversion at any given thickness.

6.3.2 Effect of temperature

Experimental results with a stepwise variation of temperature were severely affected by deactivation over time and the increasingly detrimental ramifications of mass transport limitations, when the temperature rises, might not be as meaningful as they otherwise could have been. The simulation, therefore, provides an alternative route to explore the effects of operating a pristine catalyst at different temperatures. Transport pores are not considered, however, as they do not sufficiently improve mass transport. Results analogously displayed to the previous section, yet for just 1% conversion, are shown in figure 6.17 for catalyst layers operating at temperatures from 200 °C to 240 °C with increments of 5 °C. For the lower temperatures, up to 220 °C, nothing unusual happens. Only the total reaction rate drops allowing for a flatter profile and a less pronounced maximum in the efficiency, but at the same time also lowering the total flux for CO, though this is partially compensated for by a shift to higher layer for the maximum exploitable layer thicknesses. The selectivity at low temperatures also shows similar behaviour to the default temperature of 220 °C, merely the transition from low thickness with low C_{5+} and high methane selectivity to greater thicknesses with higher C_{5+} and lower methane selectivity is stretched out over a longer thickness range. Also, the difference in selectivity during this transition becomes smaller, as, with lower temperatures, the catalyst gets less sensitive to concentration changes. However, for temperatures exceeding 220 °C, all plots are no longer surjective. This means that for certain layer thicknesses, multiple solutions exist. The now very substantial maximum in efficiency, exceeding 200% at 240 °C, occurs around 52 µm before dropping down with further increasing layer thickness. Layers with lower thicknesses exhibit a monotone increase in efficiency as the thickness increases up to about 56 µm before the curve turns back to reach the maximum. For the molar flux of CO, the multiplicity is also well observable at about the end of the thickness range, where, with increasing thickness, also the flux increases, thereby marking the transition from layers with little diffusion

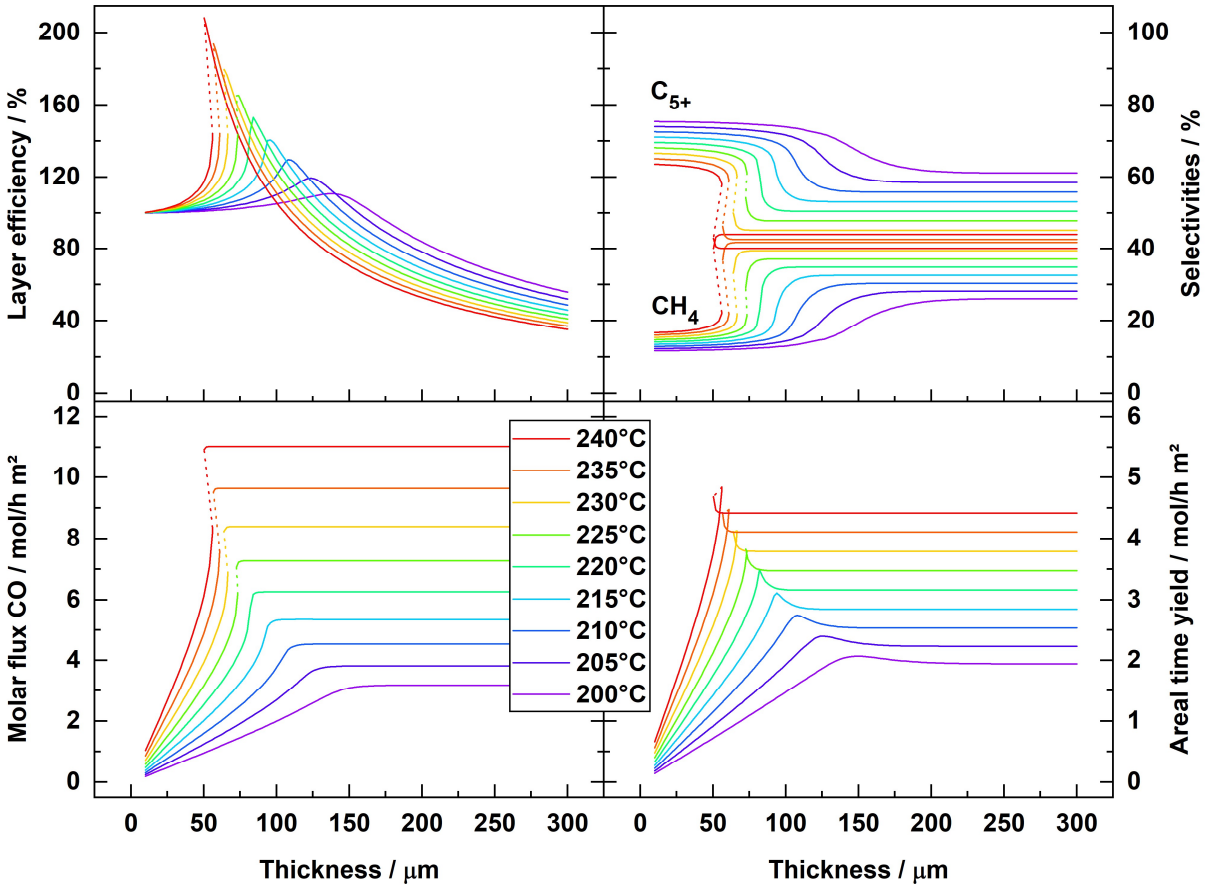

Figure 6.17: Averaged values of catalyst layer efficiency (top left), methane and C_{5+} selectivity (top right), the molar flux of CO (bottom left) and areal time yield (bottom right) as a function of layer thickness for catalyst layers operated at different temperatures. $p = 21$ bar, $H_2/CO = 2$, $CO/Ar = 9$, $X_{CO} = 1\%$.

influence towards a severe impact of diffusion. The selectivity also shows multiple solutions in this transition range and for the highest temperature a jump, with a maximum difference for methane and C_{5+} selectivity of more than 20% and 30%, respectively, entails. Combining selectivity and molar flux yields a fairly peculiar behaviour for the ATY with loops around the maxima for each curve. Otherwise, the ATY plots are as expected, with the two distinct sections for thick and thin layers. At low thicknesses, the ATY exhibits a linear increase with layer thickness, as diffusion limitations are marginal, and for thick layers with severe diffusion limitations, only a constant value for ATY is obtained. These very unusual results, exhibiting multiplicity, are well known when non-isothermal reactors are considered and efficiencies exceeding 100% in combination with catalysts are also common knowledge. However, multiple solutions for reaction-diffusion problems including Langmuir-Hinshelwood kinetics are much less expected, though in literature several works already indicate up to three

solutions for a certain Thiele-modulus, that translates here to layer thickness [32], also for Fisher-Tropsch catalysts [33,34]. A prerequisite for this to happen is a sufficiently high CO concentration and a high sorption coefficient. Since a positive activation energy for the sorption coefficient was estimated, high temperatures favour the existence of multiple solutions, which goes in line with the observed loss of surjectivity only at temperatures in excess of 220 °C. High conversions of CO, on the other hand, should hinder multiplicity. This is indeed depicted in figure 6.18, where no multiple solutions exist. The profiles for efficiency exhibit only very modest maxima, if any at all, and the jumps of the selectivities during the transition are also more restricted compared to operation at 1% conversion. This leads to conventional ATY plots without any odd features, only at an overall low level.

Yet, problematic are numerical solution issues preventing an overlap in the thickness as indicated by the dotted lines. Therefore, multiple solutions for the integral values may have occurred at 80% conversion as well. Checking for multiplicity is done by conducting simulations that start at either side of the thickness range and incrementally increasing or decreasing the thickness. When multiplicity occurs the simulation is regularly, prematurely forced to stop. This is caused by switching from on to the other solution type leading to a non-continuous axial profile for the local catalyst efficiency. This non-continuity in the axial profile is challenging for numerical solution, especially when non-dynamic models are considered and use of well working initial guesses is paramount for stable operation of the numerical solvers. This numerical sensitivity may also have had an influence on the result of the parameter estimation. Especially when considering a comparably large deviation between simulation and experimental results for the CO conversion at the highest temperature of 240 °C (see figure 6.9), improvements on the stability of the simulation may also contribute to more accurate parameter estimation results. Nonetheless, a lack in obtaining all possible solutions may not be too detrimental, as whether all the points mathematically feasible are also feasible via experiments remains open.

All in all the sensitivity analysis clearly shows that despite a good understanding of the observed behaviour, in detail certain reaction conditions still lead to surprising results that can trigger new investigations to improve the kinetic description involved in the models. The use of transport pores that are not specifically designed but just a result of randomly ordered spherical catalyst particles shows an only limited capacity to improve the reactor performance in total, though with respect to selectivity an improvement can be seen. However, further work might need to focus on the geometry and size of the transport pores as well as the catalyst to allow for larger gains in reactor performance.

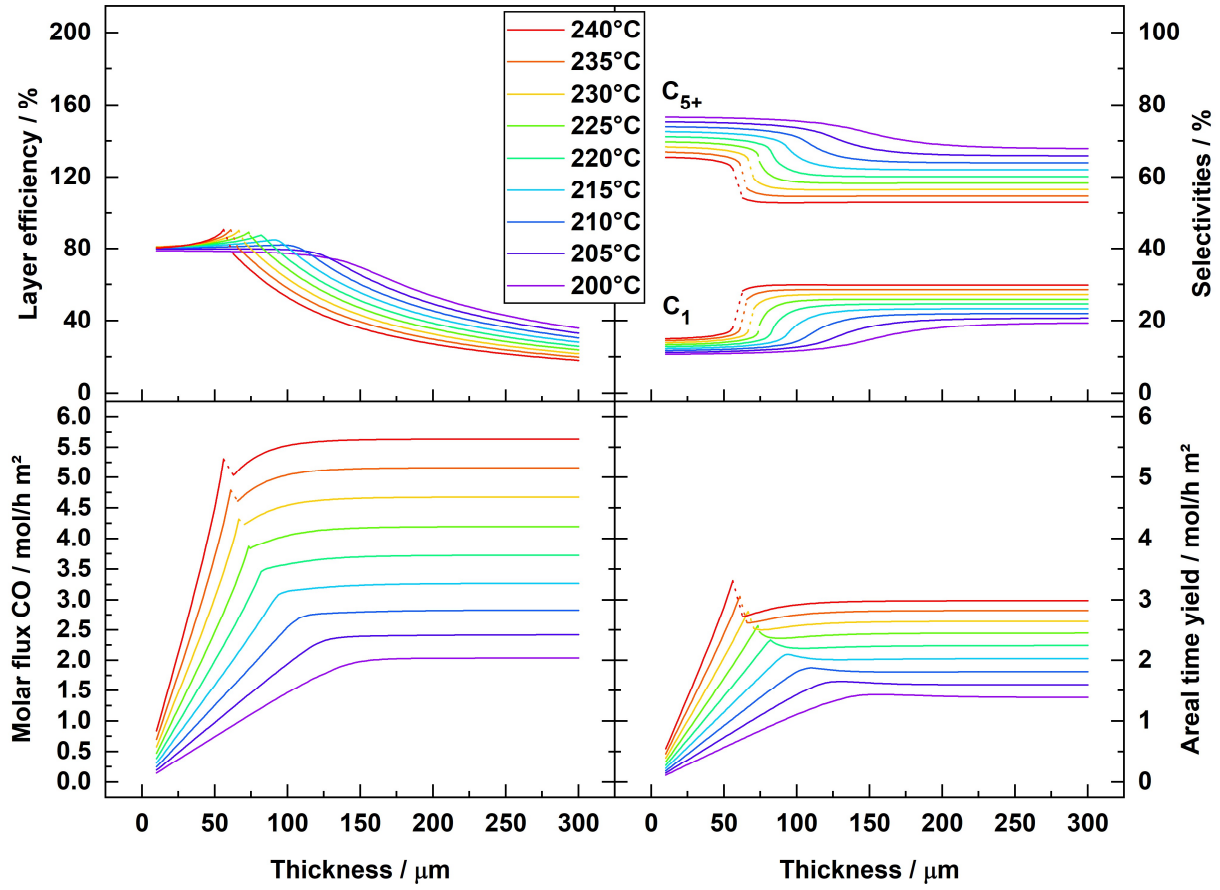

Figure 6.18: Averaged values of catalyst layer efficiency (top left), methane and C_{5+} selectivity (top right), the molar flux of CO (bottom left) and areal time yield (bottom right) as a function of layer thickness for catalyst layers operated at different temperatures. $p = 21$ bar, $H_2/CO = 2$, $CO/Ar = 9$, $X_{CO} = 80\%$.

6.4 Notation

Latin

c_{CO}	concentrations in the gas phase, mol m^{-3}
c_{gas}	concentrations in the gas phase, mol m^{-3}
c_{H_2}	concentrations in the gas phase, mol m^{-3}
D_i	diffusion coefficient of species i (H_2 or CO), m^2 s^{-1}
F	activity factor, dimensionless
F_0	initial activity Factor
H_i	Henry coefficient of species i, bar
J_{cl}	molar flux from catalyst to liquid (fluid) phase, mol s^{-1} m^{-2}
K_i	vapour-liquid equilibrium constant of species i, dimensionless

k_m reaction rate constant for additional methane termination, s^{-1}

k_p reaction rate constant for chain propagation, s^{-1}

k_t reaction rate constant for chain termination, s^{-1}

k_α selectivity coefficient for chain growth probability, dimensionless

k_γ selectivity coefficient for methane, dimensionless

$n_{c,I}$ carbon number of hydrocarbon species i, dimensionless

$\dot{n}_{CO,in}$ molar feed flow of CO, $mol\,s^{-1}$

$\dot{n}_i$ molar flow of species i, $mol\,s^{-1}$

$\dot{n}_{I,0}$ initial molar flow (or feed flow) of species i, $mol\,s^{-1}$

p pressure, bar

$p_{vap,i}$ vaporisation pressure of species i, bar

r reaction rate, $mol\,s^{-1}\,m^{-2}$

R_{CO} extensive reaction rate, $mol\,s^{-1}$

T temperature, K

t_{gas} thickness of the gas channel, m

$t_{n,end}$ time at the end of the n-th operating interval, h

$T_{ref,}$ reference temperature, 493.15 K

$t_{ref,0}$ time for first reference point n, h

$t_{ref,n}$ time for the n-th reference point, h

u_{dif} theoretical velocity of the liquid products within the catalyst layer due to diffusion, $m\,s^{-1}$

u_l velocity of the liquid products within the catalyst layer, $m\,s^{-1}$

$v_{C_{28}H_{58}}$ molar volume of the liquid octacosane, $mol\,m^{-3}$

X conversion of CO, dimensionless

X_0 initial conversion of CO, dimensionless

$x_{g,i}$ molar fraction of species i in the gas phase, dimensionless

$x_{l,i}$ molar fraction of species i in the gas phase, dimensionless

y dimension coordinate inside the catalyst layer, m

z axial dimension coordinate, m

Z total molar fraction of vaporisation, dimensionless

Greek

a chain growth probability, dimensionless

β selectivity model exponent for chain growth probability, dimensionless

γ enhanced methane termination probability, dimensionless

δ	selectivity model exponent for methane, dimensionless
$\Delta E_{A,\gamma}$	activation energy for the methane selectivity model, kJ mol^{-1}
ε_{cat}	porosity of the catalyst, dimensionless
ε_{TP}	volume fraction of transport pores, dimensionless
ν_i	stoichiometric coefficient of species i (CO, H_2, H_2O, C_nH_{2n+2}), dimensionless
τ_{cat}	tortuosity inside the catalyst phase, dimensionless
τ_{TP}	tortuosity inside the transport pores, dimensionless

7 Conclusion & Outlook

The intricate Fischer-Tropsch process was successfully modelled to predict the influence that diffusion limitations can have on the process. For micro-channel reactors with catalysts coated to the channel walls, the effect of transport pores was thoroughly investigated to test for potential benefits in reactor performance and possible prerequisites for the catalyst and the transport pores.

A general necessity for a trade-off by introducing transport pores was found. Improved mass-transport by additional pores always competes with a consequential lower amount of catalyst and thus active surface area. For conventional fixed-bed reactors, the volume fraction of catalyst is fairly constant, as the void fraction between particles is largely unaffected by particles size, causing additional transport pores inside the catalyst to only reduce the total amount of catalyst for a given reactor volume, therefore the particle size is a better variable to adjust the impact of diffusion limitations. Thus, benefits through the use of transport pores can only be evaluated on an economic basis, taking pressure drop as well as productivity into account. On the other hand, for micro-channel reactors with wall coated catalyst layers, the catalyst hold-up is directly linked to the catalyst layer thickness. Hence, transport pores provide an opportunity to improve mass transport allowing for thicker catalyst layers and thereby to increase the catalyst hold-up of the reactor, albeit the catalyst layer itself exhibits a lower volume fraction of the catalyst. Catalyst layers in micro-channel reactors are therefore an ideal system for testing of transport pores. For the Fischer-Tropsch reaction, some additional specific phenomena come into effect. They result mainly from two reactants, H_2 and CO, being involved in the reaction. The effective kinetics in combination with differences in diffusivity allow for catalyst efficiencies exceeding 100% for certain layer thicknesses, leading to the formation of an efficiency maximum. Additionally, the product selectivity is also strongly affected by the ratio of H_2 to CO with more desired products being formed when the ratio is low. In combination, the two effects lead to a maximum in productivity of C_{5+} hydrocarbons when layer thickness and transport porosity are adjusted. This can be used to optimise the performance of reactors but for that purpose, the diffusion in the transport pores needs to be superior to the diffusion in the catalyst. Moreover, the transport pores are required to be sufficiently small in order to obtain an equal concentration in transport pores and catalyst pores and to avoid yet another transport limitation. The latter criterion was fulfilled by the experimentally tested catalyst layers which were created by spraying, drying and calcination of powder catalyst

onto metallic sheets. By choosing to compact or not to compact the layers transport pores were either removed or kept as obtained during preparation. The experimental results, however, only indicated some advantage for the selectivity when transport pores are used, whereas the conversion and the total productivity could not benefit from transport pores.

Evaluation of the integral operation of micro-channel reactors further suggests some complication due to differences of the transport of the reactants in the fluid phase, where convection occurs, and the liquid phase inside the catalyst, where diffusion is predominant for the reactants. Layers with major diffusion limitations improve more in terms of selectivity when operating at high conversion than thin layers with minimal diffusion limitations. This is caused by the initial overly high consumption-ratio of H_2 to CO when strong diffusion limitations occur and therefore, the downstream ratio of H_2 to CO is lower, contributing to an improved selectivity. For the integral simulations, a novel model of estimating the impact of external mass transport was also introduced, calculating the local film thickness that forms on the surface of the catalyst. Nevertheless, even for very active catalysts and long channels, which ought to be the worst cases, the reduction in productivity due to external transport limitations was found to be negligible. For the parameter estimation, the deactivation of the catalyst was taken into account by a simple data-based estimation of bulk activity factors. The accuracy of the simulation predictions, especially for conversion, was greatly improved by this measure and reasonable parameter estimates have been obtained. The tortuosities for transport pores and catalyst pores were revealed to be only marginally different at values between 2.6 and 2.7. Hence any benefit in improving diffusive transport of the reactants is outweighed by the decrease in activity making compacted layers, without transport pores, clearly superior to non-compacted layers. However, when compacted layers are used as a baseline for further modification of catalyst layers to introduce well defined more linear transport pores, the corresponding lower tortuosity should allow for a less elusive benefit for the new layers. Another possibility to improve layers upon introduction of transport pores is by increasing the metal loading of the catalyst close to the theoretical upper limit, given by the pore volume of the support. When the catalyst support is impregnated, possibly several times, to the extent that almost all mesopores of the support are filled with cobalt, a catalyst with high activity, yet little porosity, can be obtained. In that case, diffusion in the catalyst is greatly hampered, while the activity is high. The low porosity of the catalyst would additionally cause a high tortuosity which would make optimisation of the catalyst layer even by non-ideal transport pores considerably less difficult. A catalyst of that sort, however, would probably require more sophisticated

preparation techniques as sintering and agglomeration of the active cobalt could become problematic.

Finally, the validity of the assumptions for the product composition was tested with an enhanced model that simulates the gas and liquid phase equilibrium as well as the diffusion and convection within the liquid-filled pores. For the gas phase composition, differences between the enhanced and the conventional model were found to be negligible. But only with the enhanced model the product composition in the liquid phase can be predicted, which plays an important role in the estimation of the actual values for the tortuosities, as physical properties, e.g. diffusion coefficients, require a representative paraffin of a certain chain length to be calculated. The average carbon number of the hydrocarbons in the catalyst varies with the axial position, but lateral gradients into the layer are largely irrelevant. The carbon number is therefore mostly defined by the gas-liquid equilibrium of the fluid phases and future models may be set up with a simplified, yet improved description, avoiding high computational efforts and still improving on the accuracy of the diffusion coefficients. Nonetheless, the conventional model with an assigned product carbon number of 28 utilises a reasonable guess that equals about the average carbon number of the enhanced model.

Ultimately, the reactor model also predicts some peculiar but not entirely uncommon multiple solutions for the reaction-diffusion equation that results from the used effective kinetic expression. Therefore, future works may also attempt to improve the kinetic expression by exploring a larger range of operating conditions, especially with varying syngas compositions. This variation, of course, demands a more stable catalyst as deactivation will otherwise render results from inherently longer experiments useless. Hence, catalyst regeneration cycles may be an interesting alternative for time-consuming optimisation of the stability of the catalyst activity. Alternatively, only one operating condition can be used allowing for more variation in catalyst type, layer thickness and transport pore fraction to experimentally prove the viability of the optimisation of catalyst layers by inserting transport pores, as suggested in this work.

References

[1] D. H. Meadows, D. L. Meadows, J. Randers, W. W. Behrens III, *THE LIMITS TO GROWTH*, Universe Books, New York **1972**.

[2] P. van Rüth, G. Schönwiese, K. Schönthaler, S. von Andrian-Werburg, M. Buth, H. Küchenhoff, J. Hagenberg, S. Kevork, F. Imbery, K. Friedrich, et al., *Monitoringbericht 2019*, Dessau-Roßlau **2019**.

[3] A. Jess, P. Kaiser, C. Kern, R. B. Unde, C. von Olshausen, *Chemie Ing. Tech.* **2011**, *83* (11), 1777–1791. DOI: 10.1002/cite.201100066.

[4] E. van Steen, M. Claeys, *Chem. Eng. Technol.* **2008**, *31* (5), 655–666. DOI: 10.1002/ceat.200800067.

[5] R. Guettel, U. Kunz, T. Turek, *Chem. Eng. Technol.* **2008**, *31* (5), 746–754. DOI: 10.1002/ceat.200800023.

[6] S. Leviness, S. R. Deshmukh, L. A. Richard, H. J. Robota, **2014**, 518–525. DOI: 10.1007/s11244-013-0208-x.

[7] M. E. Dry, *Catal. Today.* **2002**, *71* (3–4), 227–241. DOI: 10.1016/S0920-5861(01)00453-9.

[8] H. Schulz, *Appl. Catal. A Gen.* **1999**, *186* (1–2), 3–12. DOI: 10.1016/S0926-860X(99)00160-X.

[9] J. P. den Breejen, P. B. Radstake, G. L. Bezemer, J. H. Bitter, V. Frøseth, A. Holmen, K. P. de Jong, *J. Am. Chem. Soc.* **2009**, *131* (20), 7197–7203. DOI: 10.1021/ja901006x.

[10] S. Storsæter, B. Tøtdal, J. C. Walmsley, B. S. Tanem, A. Holmen, *J. Catal.* **2005**, *236* (1), 139–152. DOI: 10.1016/j.jcat.2005.09.021.

[11] T. M. Eggenhuisen, J. P. den Breejen, D. Verdoes, P. E. de Jongh, K. P. de Jong, *J. Am. Chem. Soc.* **2010**, *132* (51), 18318–18325. DOI: 10.1021/ja1080508.

[12] Ø. Borg, S. Eri, E. A. Blekkan, S. Storsæter, H. Wigum, E. Rytter, A. Holmen, *J. Catal.* **2007**, *248* (1), 89–100. DOI: 10.1016/j.jcat.2007.03.008.

[13] E. Rytter, S. Eri, T. H. Skagseth, D. Schanke, E. Bergene, R. Myrstad, O. A. Lindvåg, *Ind. Eng. Chem. Res.* **2007**, *46* (26), 9032–9036. DOI: 10.1021/ie071136+.

[14] M. Wolters, I. C. A. Contreras Andrade, P. Munnik, J. H. Bitter, P. E. de Jongh, K. P. de Jong, in *Stud. Surf. Sci. Catal.*, Vol. Volume 175, Elsevier **2010**.

[15] H. Becker, T. Turek, R. Güttel, *Catal. Today.* **2013**, *215*, 8–12. DOI: 10.1016/j.cattod.2012.12.013.

[16] H. J. Robota, L. A. Richard, S. R. Deshmukh, S. LeViness, D. Leonarduzzi, D. Roberts, *Catal. Surv. from Asia.* **2014**, 1–6. DOI: 10.1007/s10563-014-9175-x.

[17] L. Fratalocchi, C. G. Visconti, L. Lietti, N. Fischer, M. Claeys, *Appl. Catal. A Gen.* **2018**, *556*, 92–103. DOI: 10.1016/j.apcata.2018.02.002.

[18] M. F. M. Post, A. C. Vanthoog, J. K. Minderhoud, S. T. Sie, *AIChE J.* **1989**, *35* (7), 1107–1114. DOI: 10.1002/aic.690350706.

[19] E. Iglesia, S. L. Soled, R. A. Fiato, *J. Catal.* **1992**, *137* (1), 212–224. DOI: 10.1016/0021-9517(92)90150-G.

[20] A. Jess, C. Kern, *Chem. Eng. Technol.* **2012**, *35* (2), 369–378. DOI: 10.1002/ceat.201100615.

[21] C. Knobloch, R. Güttel, T. Turek, *Chemie Ing. Tech.* **2013**, *85* (4), 455–460. DOI: 10.1002/cite.201200202.

[22] S. Mousavi, A. Zamaniyan, M. Irani, M. Rashidzadeh, *J. Nat. Gas Sci. Eng.* **2016**, *34*, 1333–1346. DOI: 10.1016/j.jngse.2016.07.068.

[23] J. Yang, Y. Qi, J. Zhu, Y.-A. Zhu, D. Chen, A. Holmen, *J. Catal.* **2013**, *308*, 37–49. DOI: 10.1016/j.jcat.2013.05.018.

[24] G. T. K. K. Gunasooriya, A. P. van Bavel, H. P. C. E. Kuipers, M. Saeys, *ACS Catal.* **2016**, *6* (6), 3660–3664. DOI: 10.1021/acscatal.6b00634.

[25] M. Zhuo, K. F. Tan, A. Borgna, M. Saeys, *J. Phys. Chem. C.* **2009**, *113* (19), 8357–8365. DOI: 10.1021/jp900281h.

[26] J. Schweicher, A. Bundhoo, N. Kruse, *J. Am. Chem. Soc.* **2012**, *134* (39), 16135–16138. DOI: 10.1021/ja3068484.

[27] R. A. van Santen, A. J. Markvoort, *ChemCatChem.* **2013**, *5* (11), 3384–3397. DOI: 10.1002/cctc.201300173.

[28] B. Todic, W. Ma, G. Jacobs, B. H. Davis, D. B. Bukur, *Catal. Today.* **2014**, *228*, 32–39. DOI: 10.1016/j.cattod.2013.08.008.

[29] C. J. Weststrate, I. M. Ciobîcă, A. M. Saib, D. J. Moodley, J. W. Niemantsverdriet, *Catal. Today.* **2014**, *228*, 106–112. DOI: 10.1016/j.cattod.2013.11.042.

[30] J. Cheng, P. Hu, P. Ellis, S. French, G. Kelly, C. Lok, *J. Catal.* **2008**, *257* (1), 221–228. DOI: 10.1016/j.jcat.2008.05.006.

[31] J. Gaube, H.-F. Klein, *J. Mol. Catal. A Chem.* **2008**, *283* (1), 60–68. DOI: 10.1016/j.molcata.2007.11.028.

[32] J. Gaube, H.-F. Klein, *Appl. Catal. A Gen.* **2010**, *374* (1), 120–125. DOI: 10.1016/j.apcata.2009.11.039.

[33] C. G. Visconti, M. Mascellaro, *Catal. Today.* **2013**, *214*, 61–73. DOI: 10.1016/j.cattod.2012.10.016.

[34] M. Ostadi, E. Rytter, M. Hillestad, *Chem. Eng. Res. Des.* **2016**, *114*, 236–246. DOI: 10.1016/j.cherd.2016.08.026.

[35] J. Patzlaff, Y. Liu, C. Graffmann, J. Gaube, *Catal. Today.* **2002**, *71* (3), 381–394. DOI: 10.1016/S0920-5861(01)00465-5.

[36] D. Förtsch, K. Pabst, E. Groß-Hardt, *Chem. Eng. Sci.* **2015**, *138*, 333–346. DOI: 10.1016/j.ces.2015.07.005.

[37] K. D. Kruit, D. Vervloet, F. Kapteijn, J. R. van Ommen, *Catal. Sci. Technol.* **2013**, *3* (9), 2210–2213. DOI: 10.1039/c3cy00080j.

[38] Z. A. Makrodimitri, D. J. M. Unruh, I. G. Economou, *J. Phys. Chem. B.* **2011**,

115 (6), 1429–1439. DOI: 10.1021/jp1063269.

[39] Z. A. Makrodimitri, D. J. M. Unruh, I. G. Economou, *Phys. Chem. Chem. Phys.* **2012**, *14* (12), 4133–4141. DOI: 10.1039/C2CP23471H.

[40] C. Erkey, J. B. Rodden, A. Akgerman, *Energy & Fuels.* **1990**, *4* (3), 275–276. DOI: 10.1021/ef00021a010.

[41] C. Erkey, J. B. Rodden, A. Akgerman, *Can. J. Chem. Eng.* **1990**, *68* (4), 661–665. DOI: 10.1002/cjce.5450680418.

[42] Lord Rayleigh, *London, Edinburgh, Dublin Philos. Mag. J. Sci.* **1892**, *34* (211), 481–502. DOI: 10.1080/14786449208620364.

[43] G. H. Neale, W. K. Nader, *AIChE J.* **1973**, *19* (1), 112–119. DOI: 10.1002/aic.690190116.

[44] H. L. Weissberg, *J. Appl. Phys.* **1963**, *34* (9), 2636–2639. DOI: 10.1063/1.1729783.

[45] J. D. Ferry, *J. Gen. Physiol.* **1936**, *20* (1), 95–104. DOI: 10.1085/jgp.20.1.95.

[46] E. M. Renkin, *J. Gen. Physiol.* **1954**, *38* (2), 225–243.

[47] M. Ternan, *Can. J. Chem. Eng.* **1987**, *65* (2), 244–249. DOI: 10.1002/cjce.5450650208.

[48] S. Y. Lee, J. D. Seader, C. H. Tsai, F. E. Massoth, *Ind. Eng. Chem. Res.* **1991**, *30* (1), 29–38. DOI: 10.1021/ie00049a005.

[49] M. D. Argyle, C. H. Bartholomew, *Catalysts.* **2015**, *5* (1), 145–269. DOI: 10.3390/catal5010145.

[50] N. E. Tsakoumis, M. Rønning, Ø. Borg, E. Rytter, A. Holmen, *Catal. Today.* **2010**, *154* (3–4), 162–182. DOI: 10.1016/j.cattod.2010.02.077.

[51] M. Sadeqzadeh, S. Chambrey, S. Piché, P. Fongarland, F. Luck, D. Curulla-Ferré, D. Schweich, J. Bousquet, A. Y. Khodakov, *Catal. Today.* **2013**, *215*, 52–59. DOI: 10.1016/j.cattod.2013.03.022.

[52] M. Sadeqzadeh, S. Chambrey, J. Hong, P. Fongarland, F. Luck, D. Curulla-Ferre, D. Schweich, J. Bousquet, A. Y. Khodakov, *Ind. Eng. Chem. Res.* **2014**, *53* (17), 6913–6922. DOI: 10.1021/ie4040303.

[53] K. Fei Tan, J. Xu, J. Chang, A. Borgna, M. Saeys, *J. Catal.* **2010**, *274* (2), 121–129. DOI: 10.1016/j.jcat.2010.06.008.

[54] G. Jacobs, P. M. Patterson, Y. Zhang, T. Das, J. Li, B. H. Davis, *Appl. Catal. A Gen.* **2002**, *233* (1–2), 215–226. DOI: 10.1016/S0926-860X(02)00147-3.

[55] K. Keyvanloo, M. J. Fisher, W. C. Hecker, R. J. Lancee, G. Jacobs, C. H. Bartholomew, *J. Catal.* **2015**, *327*, 33–47. DOI: 10.1016/j.jcat.2015.01.022.

[56] G. L. Bezemer, T. J. Remans, A. P. Van Bavel, A. I. Dugulan, *J. Am. Chem. Soc.* **2010**, *132* (25), 8540–8541. DOI: 10.1021/ja103002k.

[57] M. Claeys, M. E. Dry, E. van Steen, E. du Plessis, P. J. van Berge, A. M. Saib, D. J. Moodley, *J. Catal.* **2014**, *318*, 193–202. DOI: 10.1016/j.jcat.2014.08.002.

[58] D. Vervloet, F. Kapteijn, J. Nijenhuis, J. R. van Ommen, *Catal. Sci. Technol.* **2012**, *2* (6), 1221–1233. DOI: 10.1039/c2cy20060k.

[59] I. C. Yates, C. N. Satterfield, *Energy & Fuels.* **1991**, *5* (1), 168–173. DOI:

10.1021/ef00025a029.

[60] K. A. Akanni, J. W. Evans, I. S. Abramson, *Chem. Eng. Sci.* **1987**, *42* (8), 1945–1954. DOI: 10.1016/0009-2509(87)80141-0.

[61] J. M. Zalc, S. C. Reyes, E. Iglesia, *Chem. Eng. Sci.* **2003**, *58* (20), 4605–4617. DOI: 10.1016/j.ces.2003.07.008.

[62] S. Khirevich, A. Höltzel, A. Daneyko, A. Seidel-Morgenstern, U. Tallarek, *J. Chromatogr. A*. **2011**, *1218* (37), 6489–6497. DOI: 10.1016/j.chroma.2011.07.066.

[63] H. Rusinque, G. Brenner, *Microporous Mesoporous Mater.* **2019**, *280* (November 2018), 157–165. DOI: 10.1016/j.micromeso.2019.01.037.

[64] J. W. Beeckman, *Chem. Eng. Sci.* **1990**, *45* (8), 2603–2610. DOI: 10.1016/0009-2509(90)80148-8.

[65] A. Bufe, M. Klee, G. Wehinger, T. Turek, G. Brenner, *Chemie-Ingenieur-Technik*. **2017**, *89* (10), 1385–1390. DOI: 10.1002/cite.201700066.

[66] J. R. Pappenheimer, E. M. Renkin, L. M. Borrero, *Am. J. Physiol. Content*. **1951**, *167* (1), 13–46. DOI: 10.1152/ajplegacy.1951.167.1.13.

[67] H. H. Rachford, J. D. Rice, *J. Pet. Technol.* **1952**, *4* (10), 19–3. DOI: 10.2118/952327-G.

[68] J. J. Marano, G. D. Holder, *Ind. Eng. Chem. Res.* **1997**, *36* (6), 2409–2420. DOI: 10.1021/ie9605140.

[69] C. Tsonopoulos, *Fluid Phase Equilib.* **2001**, *186* (1–2), 185–206. DOI: 10.1016/S0378-3812(01)00520-9.

[70] C. Giraudet, K. D. Papavasileiou, M. H. Rausch, J. Chen, A. Kalantar, G. P. Van Der Laan, I. G. Economou, A. P. Fröba, *J. Phys. Chem. B.* **2017**, *121* (47), 10665–10673. DOI: 10.1021/acs.jpcb.7b07580.

[71] G. S. Witmer, V. Balakotaiah, D. Luss, *Chem. Eng. Sci.* **1986**, *41* (1), 179–186. DOI: 10.1016/0009-2509(86)85212-5.

[72] D. B. Bukur, M. Mandić, B. Todić, N. Nikačević, *Catal. Today.* **2018**. DOI: 10.1016/j.cattod.2018.10.069.

[73] R. S. Dixit, L. L. Tavlarides, *Chem. Eng. Sci.* **1982**, *37* (4), 539–544. DOI: 10.1016/0009-2509(82)80116-4.

Appendix

A. Supporting information to chapter 3

Evaluation of the productivity of microchannel reactors requires a careful choice of the reference volume as the overall absolute production rate, R_{C5+}, is not independent of reactor size and overall catalyst inventory, which is influenced by transport pore fraction and layer thickness (figure A1, left)

$$R_{C5+} = (1 - \varepsilon_{TP}) \cdot A \cdot \int_0^t r_{CO}(x) \cdot S_{C5+}(x) dx$$

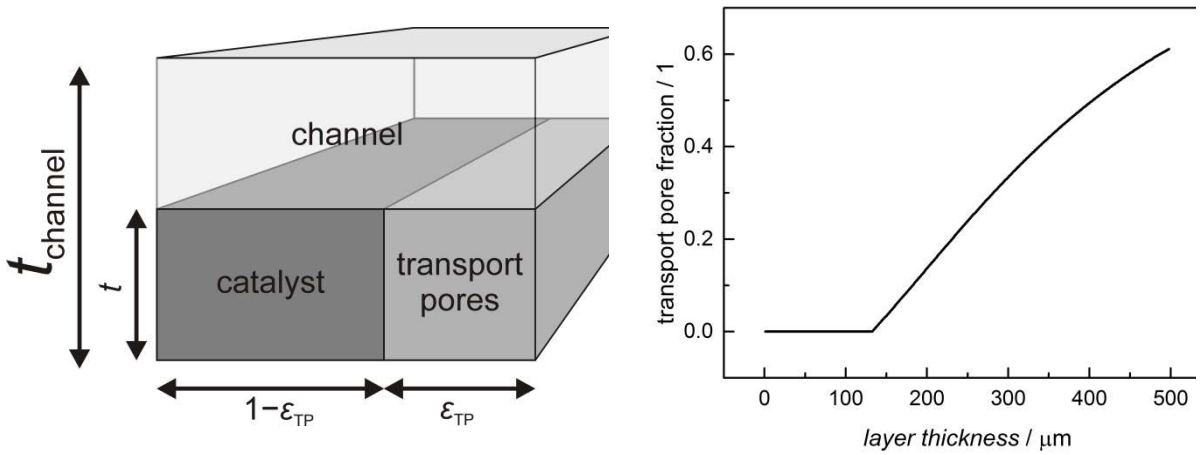

Figure A1: Schematic of a wall coated micro-reactor with catalyst, transport pore and microchannel volumes (left); transport pore fraction as a function of layer thickness; $T = 220$ °C, $p = 21$ bar, $H_2/CO = 2$, $\varepsilon_{Cat} = 0.4$, $\tau_{cat} = 3$, $\tau_{TP} = 1$ (right).

Optimization of productivity for a certain layer thickness requires an ideal transport pore fraction that maximizes C_{5+} production rate. Repeating this for several layer thicknesses lead to the ideal transport pore fraction as a function of layer thickness (figure A1, right). These conditions are also used for subsequent evaluation of productivity measures.

Catalyst volume

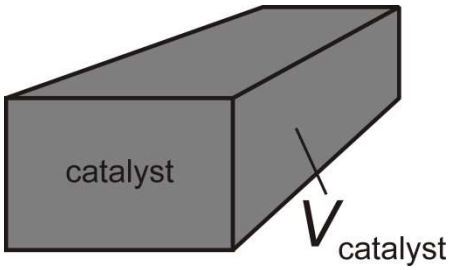

$$STY_{catalyst} = \frac{R_{C5+}}{V_{catalyst}}$$

$$= \frac{1}{t} \cdot \int_0^t r_{CO}(x) \cdot S_{C5+}(x) dx$$

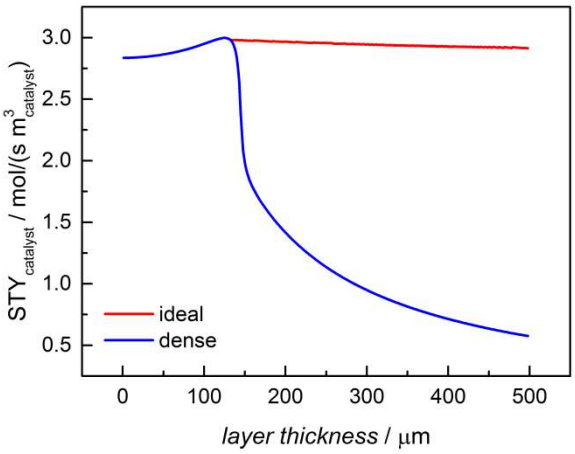

The typically used space time yield with the catalyst volume as a basis, STY_{catalyst}, does neither take into account that the amount of catalyst is reduced by transport pores nor the ambiguous effect of layer thickness, the increase of which leads to higher diffusion limitations, but also to higher catalyst inventory. Thus, results highly overestimate the improvement for a certain layer but do not show a positive effect of transport pores.

Layer volume

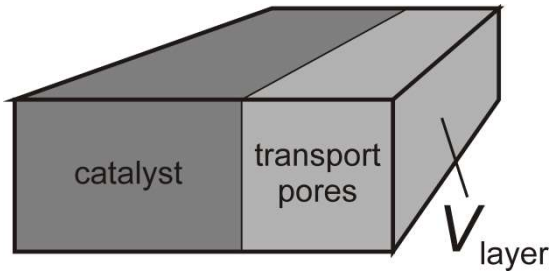

$$STY_{laye} = \frac{R_{C5+}}{V_{layer}}$$

$$= \frac{(1 - \varepsilon_{TP})}{t} \cdot \int_0^t r_{CO}(x) \cdot S_{C5+}(x) dx$$

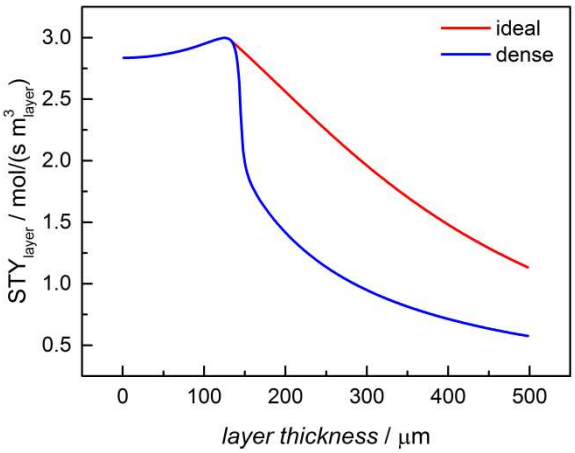

If one uses the layer volume as a basis, the resulting STY_{layer} properly accounts for the effect of transport pores, but the impact of layer thickness is still neglected. Therefore, this property is not useful for comparison of layers with different thickness.

Channel volume

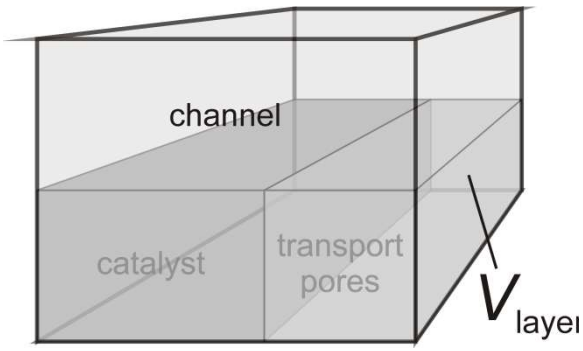

$$STY_{cha} = \frac{R_{C5+}}{V_{channel}} = \frac{(1-\varepsilon_{TP})}{t_{channel}} \cdot \int_0^t r_{CO}(x) \cdot S_{C5+}(x)dx$$

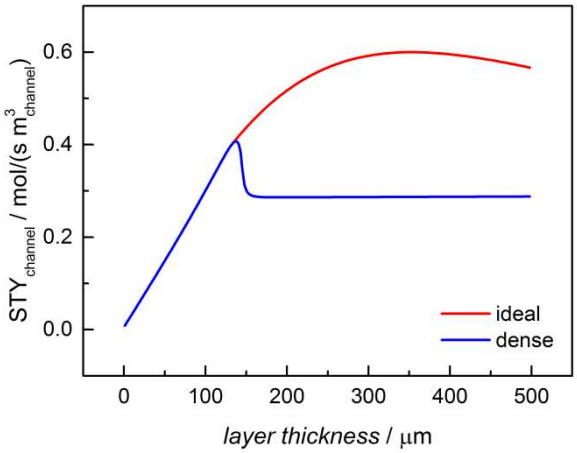

The use of the complete channel volume, including the catalyst layer, would be the best reference volume for evaluation of reactor productivity. But channel thickness can only be realistically evaluated by using an integral reactor model, considering gas and liquid flow and pressure drop. Since this was not the objective of this work, an arbitrarily fixed value of 1 mm was used.

Layer surface area

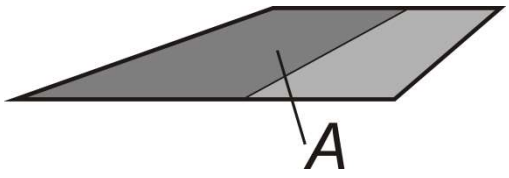

$$ATY = \frac{R_{C5+}}{A} = (1-\varepsilon_{TP}) \int_0^t r_{CO}(x) \cdot S_{C5+}(x)dx$$

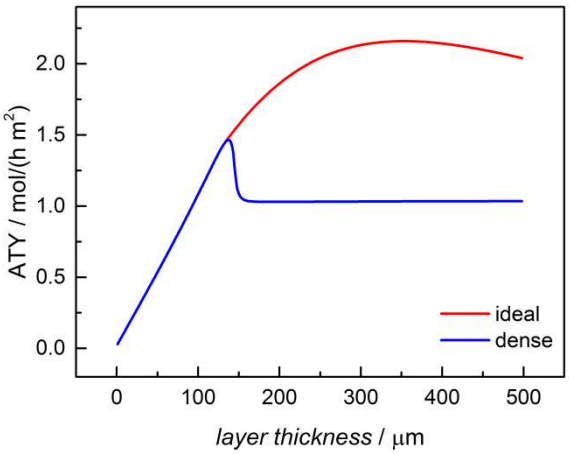

The area-specific yield, ATY, considers effects of thickness and transport pore fraction properly but avoids problems related to the channel thickness. Hence the ATY is the ideal measure for the assessment of productivity.

B. Supporting information to chapter 5

Film formation

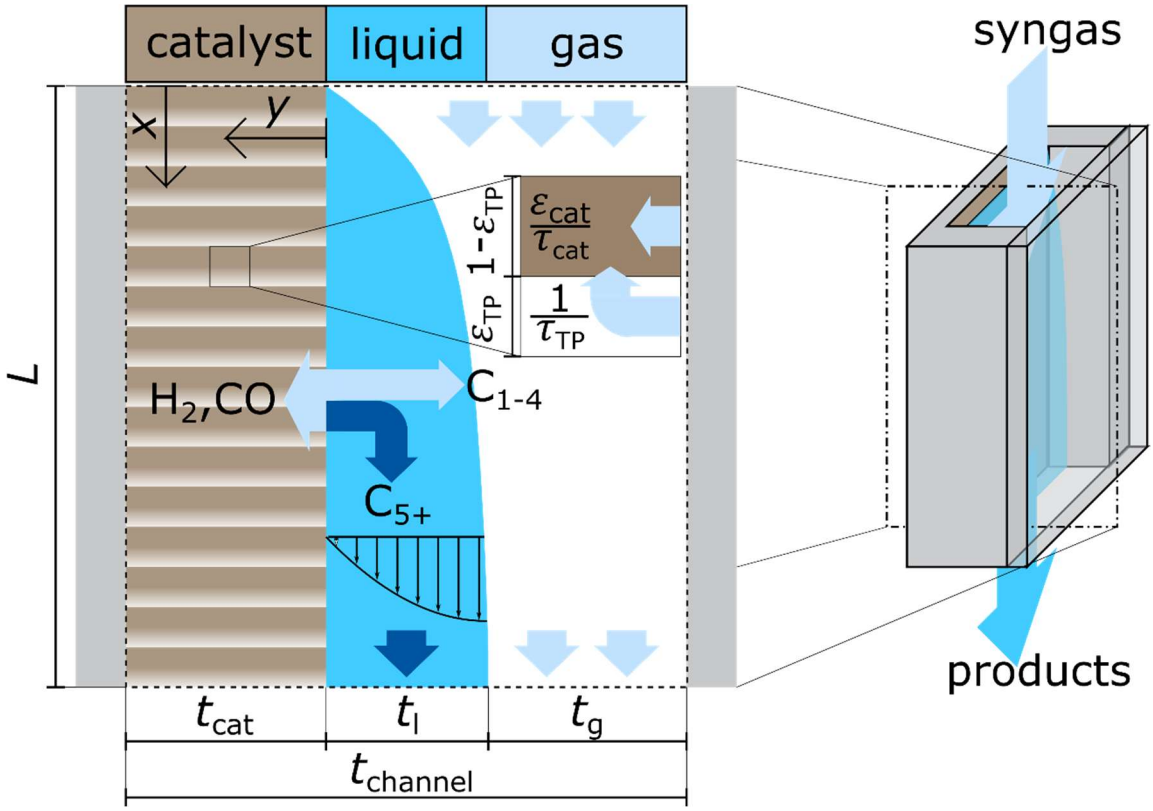

Figure B1: Schematic of a wall coated micro-reactor with catalyst layer, forming liquid film and open gas channel.

The derivation of the liquid film formation is based on the works of Nusselt and adapted for a microchannel reactor with a catalyst layer coated to one wall as depicted in figure B1. The basis for modelling is a stationary balance of shear stress with gravitational forces, equation (B1).

$$0 = \frac{\partial}{\partial y}(\tau) + (\rho_l - \rho_g)\, g \tag{B1}$$

Assuming the liquid behaves Newtonian and omitting the buoyancy effect of the gas, equation (B2) and (B3) combine to yield equation (B3), which is an ordinary differential equation needing to be solved.

$$\tau = \eta_l \frac{\partial}{\partial y}(u_l) \tag{B2}$$

$$0 = \eta_l \frac{\partial^2}{\partial y^2}(u_l) + \rho_l\, g \tag{B3}$$

At the liquid-catalyst interface, a no-slip condition forces the liquid to a standstill, equation (B4), and at the gas-liquid interface, any momentum transfer is neglected, equation (B5).

$$v(y = 0) = 0 \tag{B4}$$

$$\tau(y = t_l) = \frac{\partial}{\partial y}(u_l) = 0 \tag{B5}$$

With the assumptions of the boundary conditions, the solution for equation (B3) is easily found by integration. The obtained equation (B6) provides the velocity profile of the liquid film.

$$u_l = \frac{\rho_l\, g}{\eta_l}\left(t_l\, y - \frac{1}{2}y^2\right) \tag{B6}$$

Because the reactor model operates only with a simplified bulk flow velocity of the liquid film averaging by integration is done as in equation (B7). Equation (B8) is the desired relation of the liquid film thickness with the liquid average velocity.

$$\overline{u_l} = \frac{1}{t_l}\int_0^{t_l} \frac{\rho_l\, g}{\eta_l}\left(t_l\, y - \frac{1}{2}y^2\right) dy \tag{B7}$$

$$v_l = \overline{u_l} = \frac{\rho_l\, g\, t_l^2}{3\,\eta_l} \tag{B8}$$

Modified ASF selectivity model

The selectivity model used in this work is based on a variable alpha model, that was further modified according to Förtsch et al.[1] with an additional parameter describing the enhanced formation of methane. A second parameter for the typically low C_2 selectivity was also introduced by Förtsch et al. but not used in this work, as it did not improve the description of the results. Because no general values for the parameters were given in the literature, actual values needed to be assigned to the parameters, which are γ, describing the enhanced termination probability for methane, and β, a readsorbtion probability for C_2 species. For evaluation of useful parameter values, various data from literature[2–19] for methane, $C_{2\text{-}4}$ and C_{5+} selectivity were used. Global parameters for β and γ were tested and a variable a was adjusted for each individual data point to yield best results. When both new parameters are set to zero a conventional ASF distribution is obtained. figure 2 shows the parity plots for this case in the left column. With a conventional model, only high C_{5+} selectivities are sufficiently described, for lower values for C_{5+} the deviation increases, $C_{2\text{-}4}$ is overestimated and methane selectivity is vastly underestimated. The next column in figure 2 illustrates the results for a given γ value of 0.5 and still no change to the β value. The C_{5+} selectivities are described almost perfectly and the $C_{2\text{-}4}$ selectivity is also relatively well-matched, disregarding a certain scatter.

The methane selectivity is now also much better predicted, values up to 10% are mostly in line, only for higher values a certain offset still leads to a mild underestimation of the actual value with the model. When both parameters, β and γ, are freely adjusted to produce the best fitting to the experimental data the accuracy for the C_{5+} and the $C_{2\text{-}4}$ selectivity barely changes (see. figure. 2, right column). Only for methane, the offset at higher values is further reduced. The parameters allowing for this description are with 0.5756 for γ and 0.0 for β only slightly different from the previous case. Interestingly the probability for the readsorption of C_2 species is zero, rendering it unused and justifies the negligence in the main reactor model used for this publication. Additionally, the small difference in the results to the initially guessed value of 0.5 makes the model more conservative. For a full reactor model, an increased methane formation rate will also occur when diffusion is taken into consideration. However, this matching of useful parameters cannot and shall not be seen as full validation of a kinetic parameter set. It only acts as a justification for a reasonably working set of parameters that allow for a more realistic description of actual FT catalyst performance.

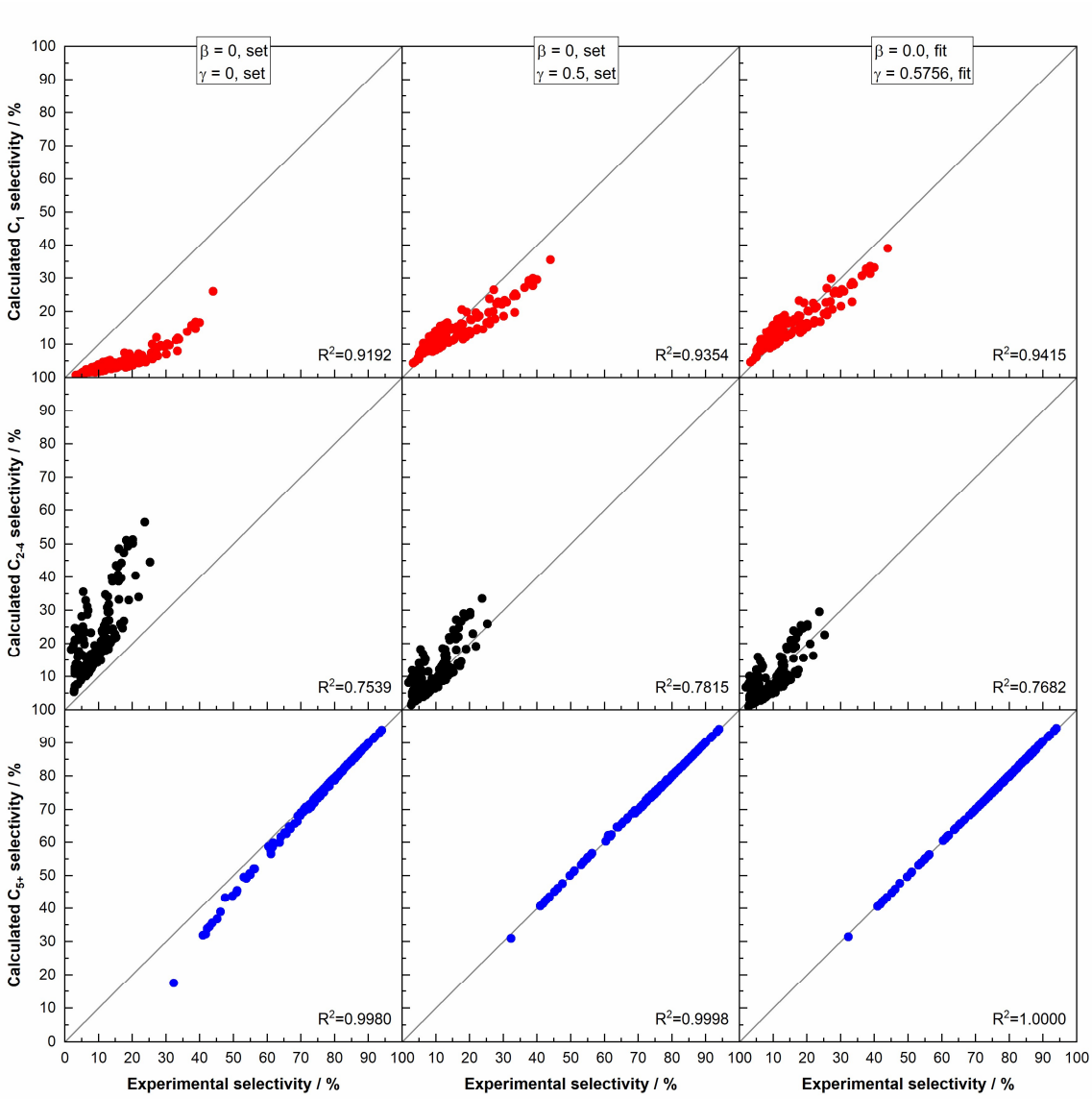

Figure B2: Parity plots for methane, $C_{2\text{-}4}$ and C_{5+} selectivities for three different parameter sets of ASF distribution modifiers; calculation based on formulas by Förtsch et al.[1] and tested against experimental data[2–19] with variable α values for each datum.

Reactor performance parameters

For evaluation of reactor performance, different parameters are required to describe the impact of diffusion resistances and integral operation on the observed reaction rate (catalyst efficiency, η) product distribution (selectivities, S_{C1} and S_{C5+}) and productivity (areal time yield, ATY). To distinguish further between the effects of diffusion on a local level and the total integral operation of the reactor, a differentiation between "local" and "total" quantities is made. "Local" measures are just a result of an integral over the

lateral domain; thus, they represent the effective performance of a slice of the catalyst layer at a given axial position. "Total" quantities, on the other hand, describe the effective performance of the entire layer in the reactor by being the result of integration over both domains, axial and lateral. For differential reactors, there are no differences between both types, as there are no axial gradients in that case.

The formulas for the local catalyst efficiency, η, the local methane selectivity, S_{C1}, the local C_{5+} selectivity, S_{C5+}, and the local productivity, ATY, are shown in equation (B9) to (B12).

$$\eta(x) = \frac{\left|j_{\mathrm{gl,CO}}(x)\right|}{t_{\mathrm{cat}} \cdot r(x, \mathrm{y}=0) \cdot (1-\varepsilon_{\mathrm{TP}})} = \frac{\left|(1-\varepsilon_{\mathrm{TP}}) \int_0^{t_{\mathrm{cat}}} r(x,y) \cdot \nu_{\mathrm{CO}}(\mathrm{x},\mathrm{y})\, dy\right|}{t_{\mathrm{cat}} \cdot r(x, \mathrm{y}=0)) \cdot (1-\varepsilon_{\mathrm{TP}})} \tag{B9}$$

$$S_{\mathrm{C1}} = \frac{j_{\mathrm{gl,C1}}(x)}{\left|j_{\mathrm{gl,CO}}(x)\right|} = \frac{\int_0^{t_{\mathrm{cat}}} r(x,y) \cdot \nu_{\mathrm{C1}}(x,y)\, dy}{\int_0^{t_{\mathrm{cat}}} r(x,y) \cdot \nu_{\mathrm{CO}}(\mathrm{x},\mathrm{y})\, dy} \tag{B10}$$

$$\begin{aligned} S_{\mathrm{C5+}}(x) &= 1 - S_{\mathrm{C1\text{-}4}}(x) = 1 - \frac{j_{\mathrm{gl,C1}}(x) + j_{\mathrm{gl,C2}}(x) \cdot 2 + j_{\mathrm{gl,C3}}(x) \cdot 3 + j_{\mathrm{gl,C4}}(x) \cdot 4}{\left|j_{\mathrm{gl,CO}}(x)\right|} \\ &= 1 - \frac{\int_0^{t_{\mathrm{cat}}} r(x,y) \cdot [\nu_{\mathrm{C1}}(x,y) + \nu_{\mathrm{C2}}(x,y) \cdot 2 + \nu_{\mathrm{C3}}(x,y) \cdot 3 + \nu_{\mathrm{C4}}(x,y) \cdot 4]\, dy}{\int_0^{t_{\mathrm{cat}}} r(x,y) \cdot \nu_{\mathrm{CO}}(\mathrm{x},\mathrm{y})\, dy} \end{aligned} \tag{B11}$$

$$\begin{aligned} ATY(x) &= \left|j_{\mathrm{gl,CO}}(x)\right| - j_{\mathrm{gl,C1}}(x) - j_{\mathrm{gl,C2}}(x) \cdot 2 - j_{\mathrm{gl,C3}}(x) \cdot 3 - j_{\mathrm{gl,C4}}(x) \cdot 4 \\ &= \int_0^{t_{\mathrm{cat}}} r(x,y) \cdot [|\nu_{\mathrm{CO}}(\mathrm{x},\mathrm{y})| - \nu_{\mathrm{C1}}(x,y) - \nu_{\mathrm{C2}}(x,y) \cdot 2 + \nu_{\mathrm{C3}}(x,y) \cdot 3 + \nu_{\mathrm{C4}}(x,y) \cdot 4]\, dy \end{aligned} \tag{B12}$$

The catalyst efficiency, as defined by equation (B9), is the true efficiency of the catalyst without being affected by the diluting effect of the transport pore phase. This efficiency is only used as a local variable because any use for the integral reactor in total could lead to ambiguity. The ambiguity stems from the fact that the efficiency requires a reference for the reaction rate in the denominator of equation (B9). As reference either the reaction at the layer surface ($\mathrm{y}=0$) at the reactor inlet ($\mathrm{x}=0$) can be used or the rate at the catalyst surface ($\mathrm{y}=0$) along the axial domain for each individual point of the integration can be used. Neither case was deemed useful for evaluation and thus omitted. For the C_{5+} selectivity and for the ATY no neat equation was found to produce the value as a function of α and γ. Instead, the values were calculated as the difference of the production of C_1 to C_4 and the consumption of CO.

The remaining parameters for the total performance of the reactor, S_{C1}, S_{C5+} and ATY, are shown in equation (B13) to (B15). They are merely the result of averaging the local parameters over the axial domain via integration.

$$S_{\mathrm{C1}} = \frac{\int_0^{\mathrm{L}} j_{\mathrm{gl,C1}}(x)dx}{\int_0^{\mathrm{L}} \left|j_{\mathrm{gl,CO}}(x)\right|dx} \tag{B13}$$

$$S_{C5+} = 1 - \frac{\int_0^L \left(j_{gl,C1}(x) + j_{gl,C2}(x) \cdot 2 + j_{gl,C3}(x) \cdot 3 + j_{gl,C4}(x) \cdot 4\right) dx}{\int_0^L \left|j_{gl,CO}(x)\right| dx} \quad \text{(B14)}$$

$$ATY = \frac{\int_0^L \left|j_{gl,CO}(x)\right| dx}{L} - \frac{\int_0^L \left(j_{gl,C1}(x) + j_{gl,C2}(x) \cdot 2 + j_{gl,C3}(x) \cdot 3 + j_{gl,C4}(x) \cdot 4\right) dx}{L} \quad \text{(B15)}$$

Convective transport in liquid versus gas phase

The used model neglects the axial transport in the liquid phase. To have an impact, that justifies inclusion in the model, the amount of reactants transported in the liquid phase, as described by equation (16), needs to be of similar magnitude than the amount transported in the gas phase, equation (17). Hence a high velocity and film thickness of the liquid and a high concentration of the reactants in the liquid phase, which is limited by their solubility, would increase the amount of reactants being transported in the liquid phase.

$$j_{liq}(x) \cdot t_{liq}(x) = u_{liq}(x) \cdot t_{liq}(x) \cdot c_{liq}(x) \quad \text{(B16)}$$

$$j_{gas}(x) \cdot t_{gas}(x) = u_{gas}(x) \cdot t_{gas}(x) \cdot c_{gas}(x) \quad \text{(B17)}$$

For all tested scenarios the reactor with the highest activity factor of 10, the longest channel length of 1 m, and ideal transport pore fraction and optimal catalyst layer thickness (42.3%, 114.7 µm) led to the highest liquid film thickness. Additionally, a high CO conversion of 80% results in a low gas velocity. All this pronounces the role of the convective transport in the liquid film over the convective transport in the gas phase. Yet, the axial profiles of thickness, velocity and concentration indicate a vastly more effective transport in the gas phase, that is more than three magnitudes larger than in the liquid phase, figure 3. This result warrants to neglect the convective transport in the liquid phase as done for the main reactor model.

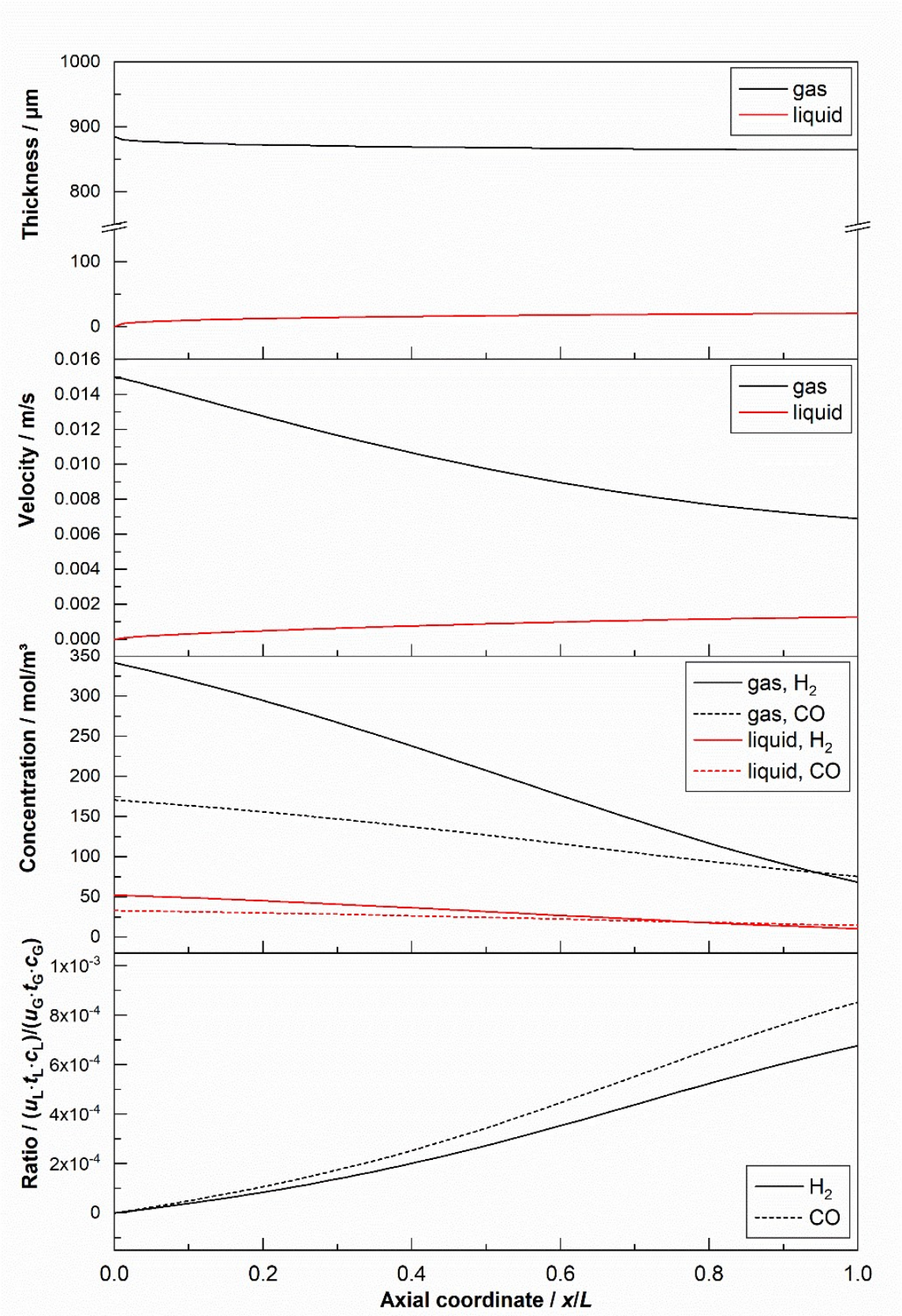

Figure B3: Axial profiles of thickness, velocity and concentration of reactants for the gas phase and the liquid phase. 80% CO conversion, $t_{cat} = 114.7\,\mu m$, $\varepsilon_{TP} = 0.423$, $F = 10$.

Effects of conversion on selectivity

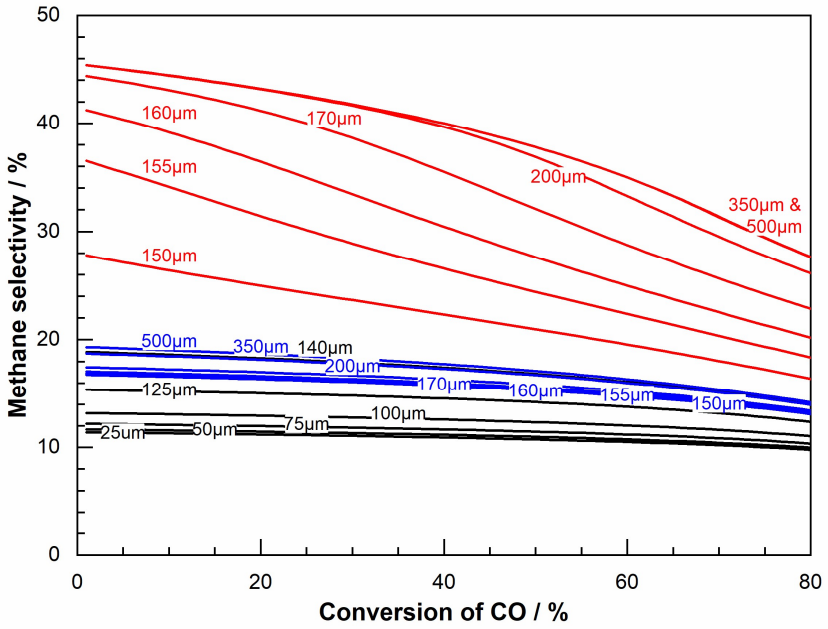

Figure B4: Effect of CO conversion on total methane selectivity of layers of different thickness and kind; thin layers with minor diffusion effects (black); thick layers with significant mass transport restrictions (blue); thick layers with added, ideal fraction of transport pores (red).

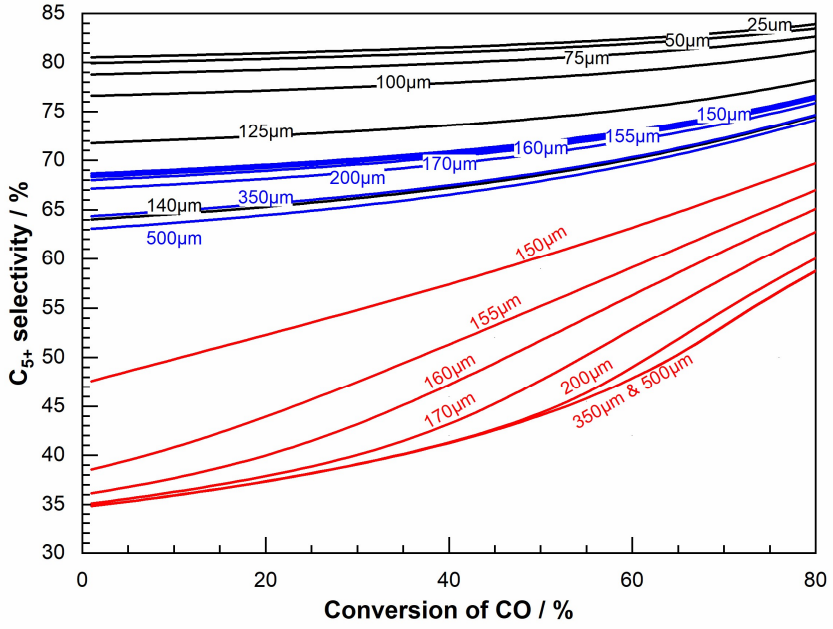

Figure B5: Effect of conversion on total C_{5+} selectivity of layers of different thickness and kind; thin layers with minor diffusion effects (black); thick layers with significant mass transport restrictions (blue); thick layers with added, ideal fraction of transport pores (red).

Additional values for the effect of conversion

Table B1: Effect of conversion on the required optimal thickness and resulting total ATY.

	"dense", ε_{TP} =0		"ideal", ε_{TP}= 0.42	
CO Conversion	thickness	ATY	thickness	ATY
%	µm	mol/(m² h)	µm	mol/(m² h)
1	140.2	1.249	357.1	1.837
5	140.5	1.247	358.2	1.834
10	140.7	1.244	358.6	1.830
15	140.8	1.241	359.0	1.825
20	141.0	1.237	359.6	1.820
25	141.3	1.234	360.1	1.814
30	141.5	1.229	360.8	1.808
35	141.8	1.225	361.5	1.801
40	142.1	1.219	362.3	1.793
45	142.5	1.213	363.2	1.784
50	142.8	1.206	364.2	1.773
55	143.2	1.196	365.1	1.759
60	143.5	1.196	365.9	1.742
65	143.7	1.168	366.4	1.718
70	143.7	1.145	366.4	1.684
75	143.3	1.111	365.4	1.634
80	142.2	1.059	362.6	1.558

References

1 D. Förtsch, K. Pabst and E. Groß-Hardt, *Chem. Eng. Sci.*, 2015, **138**, 333–346.

2 H. Becker, R. Güttel and T. Turek, *Catal. Today*, 2016, **275**, 155–163.

3 L. C. Almeida, F. J. Echave, O. Sanz, M. A. Centeno, G. Arzamendi, L. M. Gandía, E. F. Sousa-Aguiar, J. A. Odriozola and M. Montes, *Chem. Eng. J.*, 2011, **167**, 536–544.

4 D. Merino, I. Pérez-Miqueo, O. Sanz and M. Montes, *Top. Catal.*, 2016, **59**, 207–218.

5 M. Lualdi, S. Lögdberg, M. Boutonnet and S. Järås, *Catal. Today*, 2013, **214**, 25–29.

6 L. Fratalocchi, C. G. Visconti, L. Lietti, E. Tronconi, U. Cornaro and S. Rossini, *Catal. Today*, 2015, **246**, 125–132.

7 R. Zennaro, M. Tagliabue and C. H. Bartholomew, *Catal. Today*, 2000, **58**, 309–319.

8 S. Storsæter, B. Tøtdal, J. C. Walmsley, B. S. Tanem and A. Holmen, *J. Catal.*, 2005, **236**, 139–152.

9 S. Lögdberg, M. Boutonnet, J. C. Walmsley, S. Järås, A. Holmen and E. A. Blekkan, *Appl. Catal. A Gen.*, 2011, **393**, 109–121.

10 H. J. Robota, L. A. Richard, S. Deshmukh, S. LeViness, D. Leonarduzzi and D. Roberts, *Catal. Surv. from Asia*, 2014, 1–6.

11 D. Merino, O. Sanz and M. Montes, *Chem. Eng. J.*, 2017, **327**, 1033–1042.

12 L. Fratalocchi, C. G. Visconti, L. Lietti, N. Fischer and M. Claeys, *Appl. Catal. A Gen.*, 2018, **556**, 92–103.

13 G. Prieto, A. Martínez, R. Murciano and M. A. Arribas, *Appl. Catal. A Gen.*, 2009, **367**, 146–156.

14 A. Martínez, G. Prieto and J. Rollán, *J. Catal.*, 2009, **263**, 292–305.

15 D. Yin, W. Li, W. Yang, H. Xiang, Y. Sun, B. Zhong and S. Peng, *Microporous Mesoporous Mater.*, 2001, **47**, 15–24.

16 J. Yang, S. Boullosa Eiras, R. Myrstad, H. J. Venvik, P. Pfeifer and A. Holmen, in *Catalysts and Catalysis: Advances and Applications*, eds. B. H. Davis and M. L. Occelli, CRC Press, 2016, pp. 259–266.

17 L. C. Almeida, O. Sanz, J. D'olhaberriague, S. Yunes and M. Montes, *Fuel*, 2013, **110**, 171–177.

18 M. H. Rafiq, H. A. Jakobsen, R. Schmid and J. E. Hustad, *Fuel Process. Technol.*, 2011, **92**, 893–907.

19 A. M. Saib, M. Claeys and E. van Steen, *Catal. Today*, 2002, **71**, 395–402.

C. Supporting information for the model validation

Table C1: Results of parameter estimation on experimental data for different model scenarios.

	$\gamma = 0$, $F = 1$	$\gamma = 0$, $F = \mathrm{f}(t)$	$\gamma = \mathrm{const}$, $F = 1$	$\gamma = \mathrm{const}$, $F = \mathrm{f}(t)$	$\gamma = \mathrm{f}(T,c)$, $F=1$	$\gamma = \mathrm{f}(T,c)$, $F = \mathrm{f}(t)$
inetic parameters:						
Kinetic coeff. activ. energy, kJ/mol	239.4	136.6	229.7	260.6	224.2	256.9
Activ. energy for sorption, kJ/mol	96.02	36.92	87.86	95.87	84.29	91.16
Kinetic coeffficient, $\mathrm{mol \cdot kg^{-1} \cdot s^{-1} \cdot bar^{-2}}$	$1.229 \cdot 10^{-2}$	$2.389 \cdot 10^{-2}$	$3.275 \cdot 10^{-2}$	$6.824 \cdot 10^{-2}$	$3.327 \cdot 10^{-2}$	$4.979 \cdot 10^{-2}$
Sorption coefficient, $\mathrm{bar^{-1}}$	1.136	1.618	2.402	3.101	2.426	2.581
Parameters for a:						
Activation energy, kJ/mol	0.00	39.08	18.76	18.49	10.40	17.71
Selectivity coefficient, -	$7.83 \cdot 10^{-2}$	$1.38 \cdot 10^{-1}$	$8.70 \cdot 10^{-2}$	$9.12 \cdot 10^{-2}$	$1.49 \cdot 10^{-1}$	$1.99 \cdot 10^{-2}$
Exponent, -	2.000	1.504	0.859	0.783	0.382	0.142
Parameters for γ:						
Activation energy, kJ/mol	-	-	0.00	0.00	-11.27	-8.26
Selectivity coefficient, -	-	-	0.755	0.750	1.41	1.53
Exponent, dimensionless	-	-	0	0	0.543	0.589
Parameters for effective diffusion:						
Tortuosity of catalyst, -	7.466	3.207	2.769	2.748	2.780	2.772
Tortuosity of transport pores, -	3.347	4.616	2.677	2.592	2.639	2.739

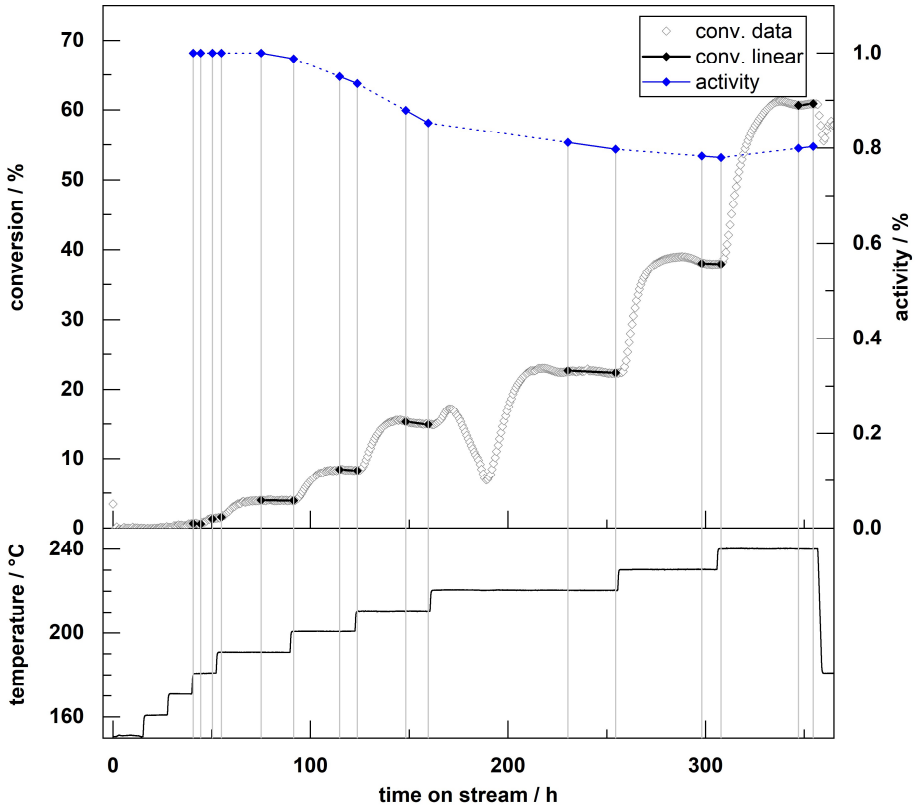

Figure C1: Results of a catalyst layer with transport pores and a thickness of 65 µm; temporal loss in conversion due to an untimely resolved shortage in hydrogen.

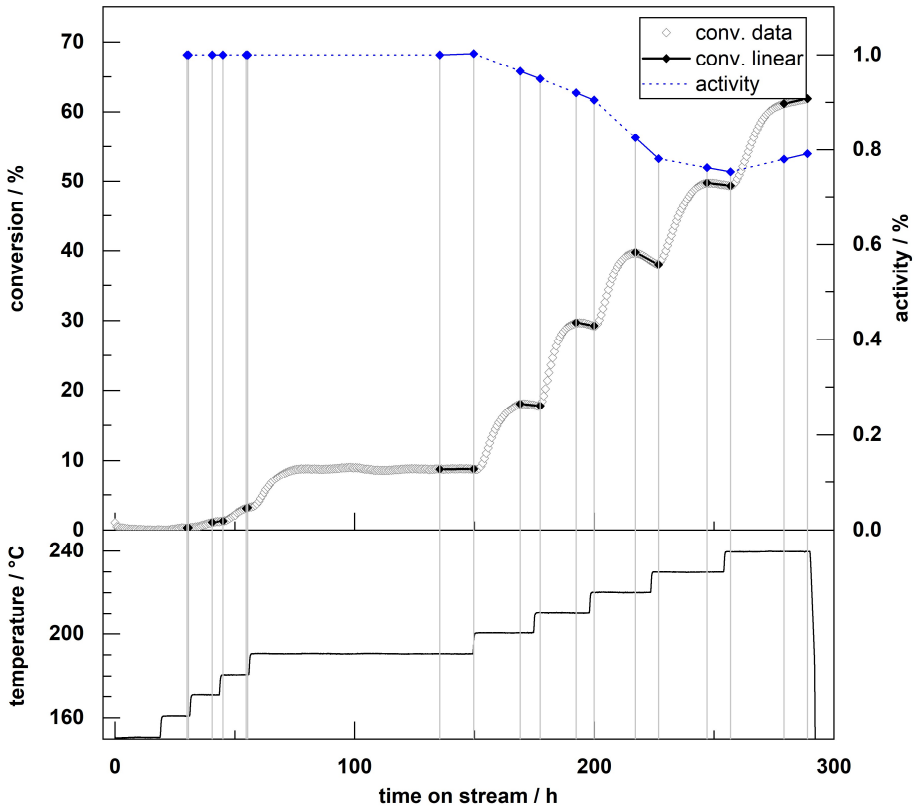

Figure C2: Results of a catalyst layer with transport pores and a thickness of 141 µm.

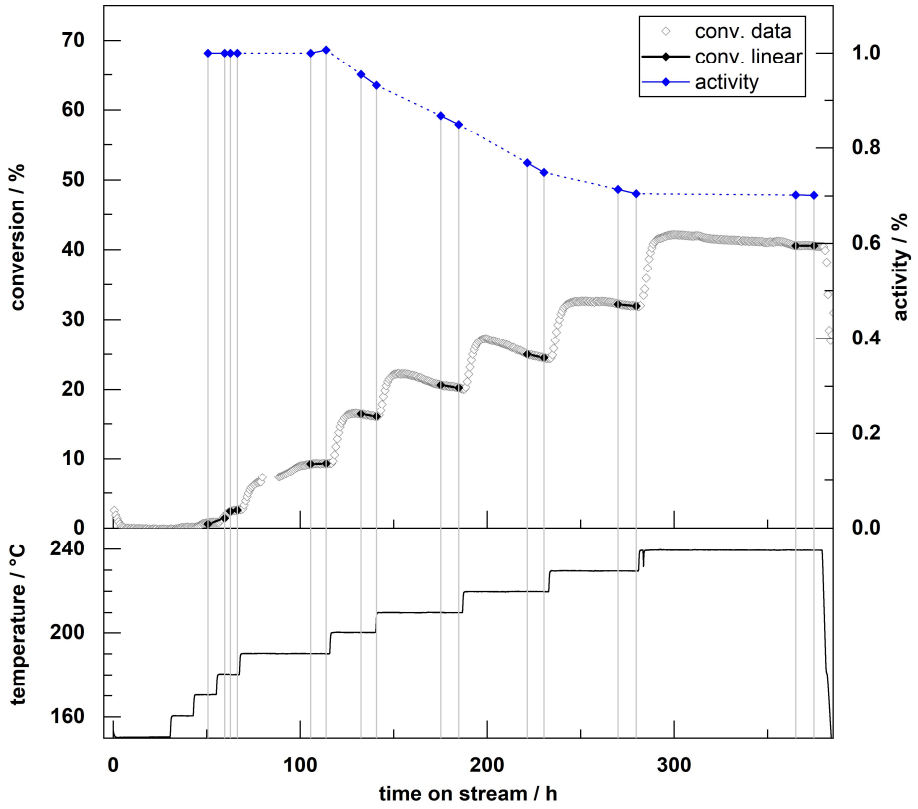

Figure C3: Results of a catalyst layer with transport pores and a thickness of 285 µm.

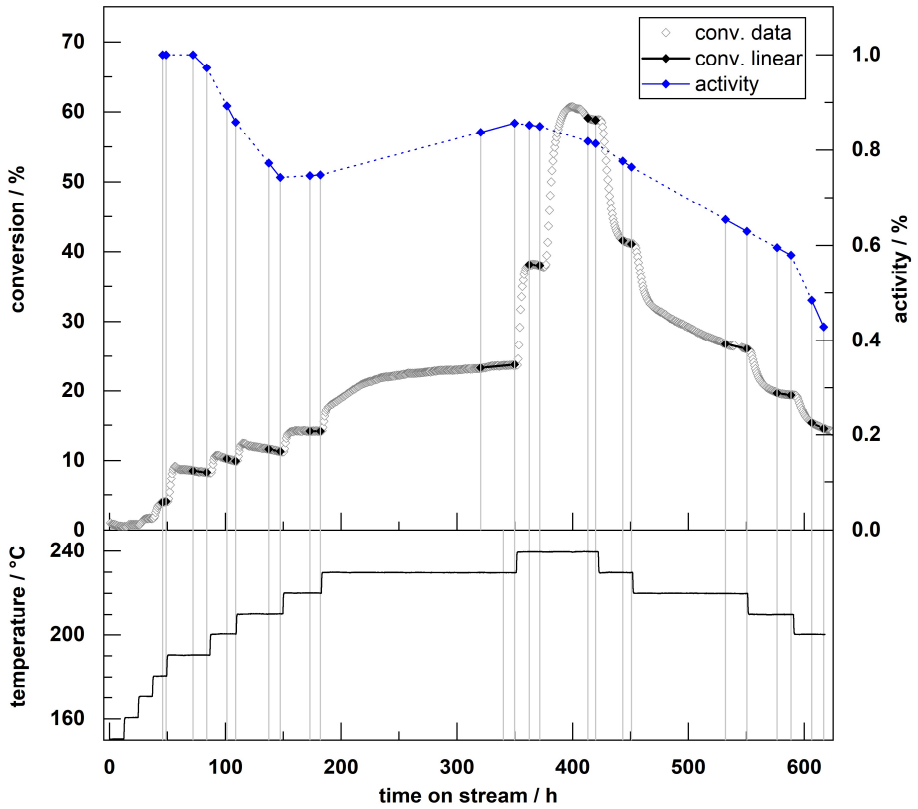

Figure C4: Results of a catalyst layer with transport pores and a thickness of 485 µm; GHSV changes from 5000 h^{-1} to 2500 h^{-1} at 410 h.

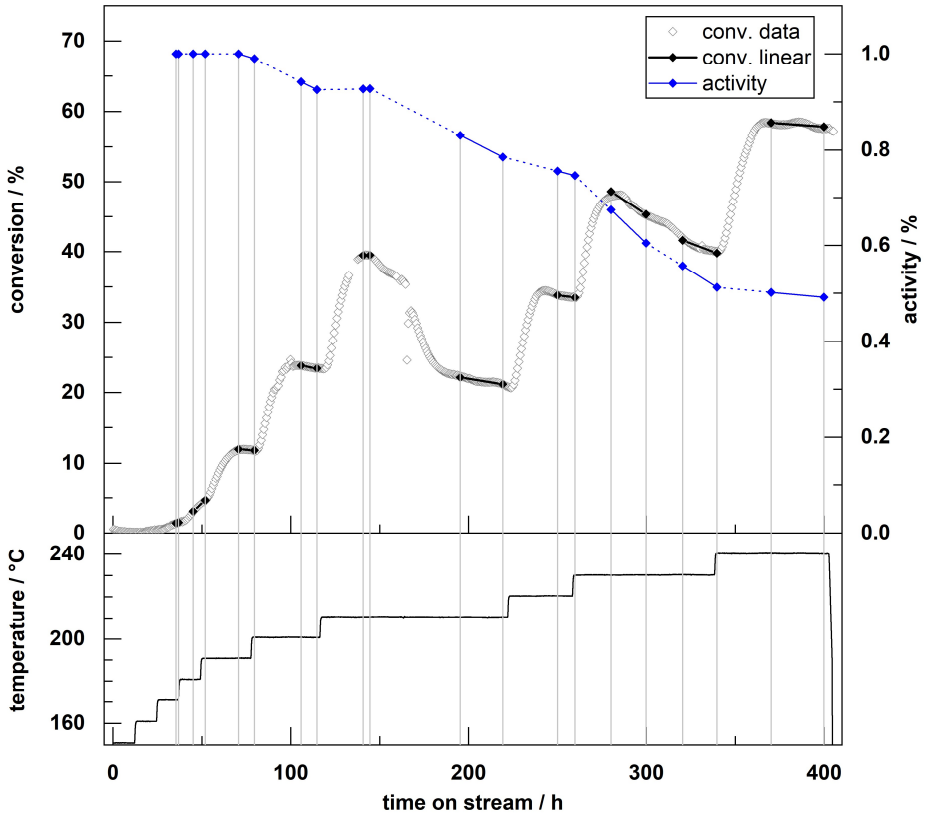

Figure C5: Results of a catalyst layer without transport pores and a thickness of 65 µm.

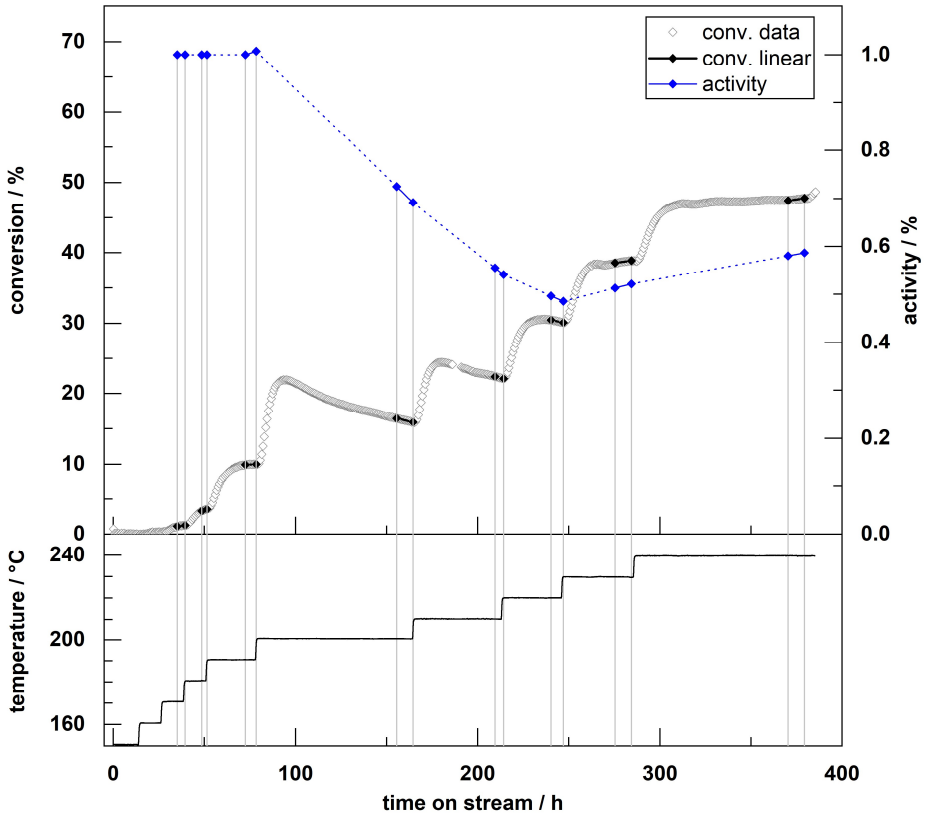

Figure C6: Results of a catalyst layer without transport pores and a thickness of 191 µm.

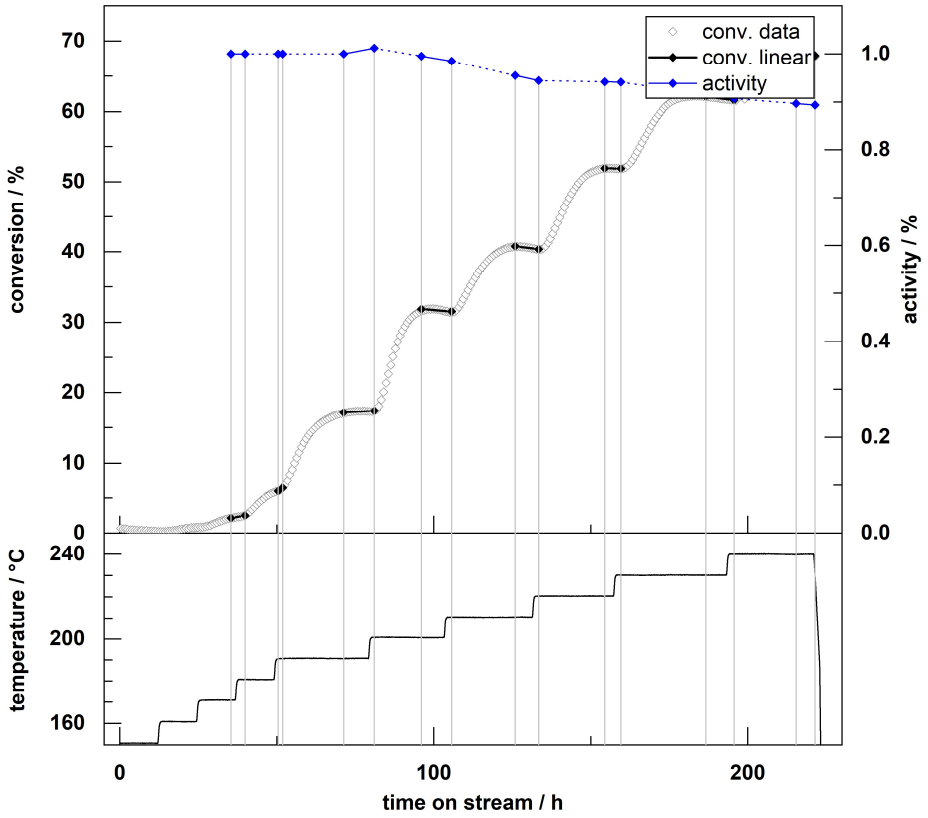

Figure C7: Results of a catalyst layer without transport pores and a thickness of 145 µm.

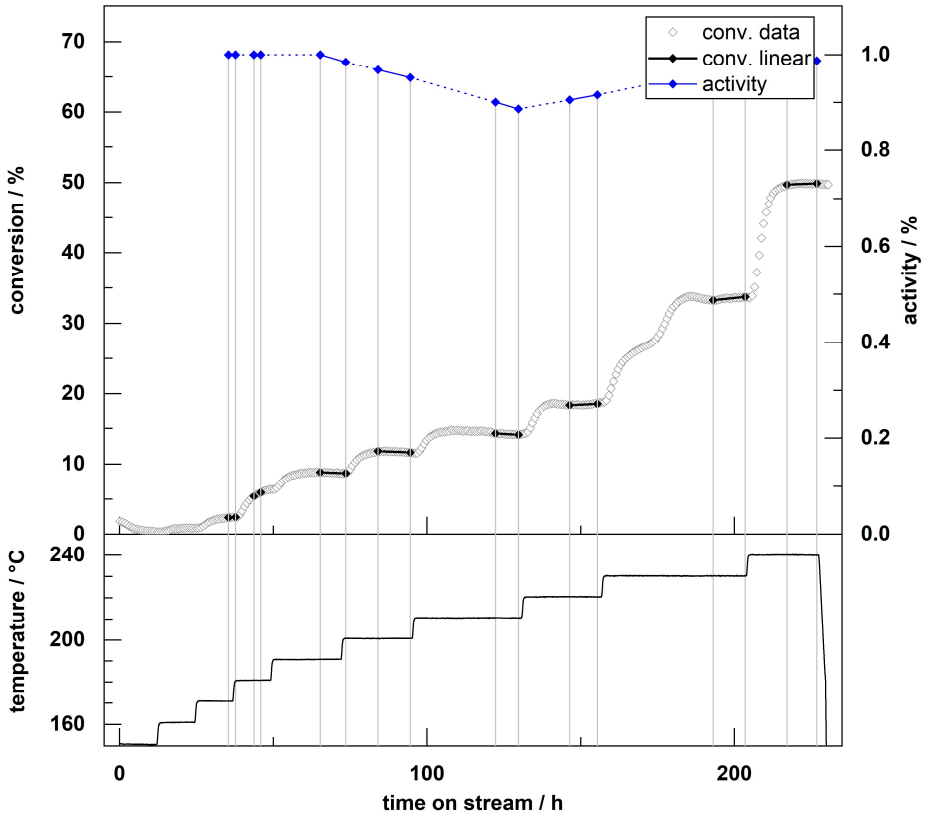

Figure C8: Results of a catalyst layer without transport pores and a thickness of 443 µm.